

Geophysical Methods for Stratigraphic Identification

September 2020

Judy Robinson
Rob D Mackley
Mark Rockhold
Tim Johnson
Jonathan Thomle
Christian Johnson
Piyoosh Jaysaval

DISCLAIMER

This report was prepared as an account of work sponsored by an agency of the United States Government. Neither the United States Government nor any agency thereof, nor Battelle Memorial Institute, nor any of their employees, makes **any warranty, express or implied, or assumes any legal liability or responsibility for the accuracy, completeness, or usefulness of any information, apparatus, product, or process disclosed, or represents that its use would not infringe privately owned rights.** Reference herein to any specific commercial product, process, or service by trade name, trademark, manufacturer, or otherwise does not necessarily constitute or imply its endorsement, recommendation, or favoring by the United States Government or any agency thereof, or Battelle Memorial Institute. The views and opinions of authors expressed herein do not necessarily state or reflect those of the United States Government or any agency thereof.

PACIFIC NORTHWEST NATIONAL LABORATORY
operated by
BATTELLE
for the
UNITED STATES DEPARTMENT OF ENERGY
under Contract DE-AC05-76RL01830

Printed in the United States of America

Available to DOE and DOE contractors from the
Office of Scientific and Technical Information,
P.O. Box 62, Oak Ridge, TN 37831-0062;
ph: (865) 576-8401
fax: (865) 576-5728
email: reports@adonis.osti.gov

Available to the public from the National Technical Information Service
5301 Shawnee Rd., Alexandria, VA 22312
ph: (800) 553-NTIS (6847)
email: orders@ntis.gov <<https://www.ntis.gov/about>>
Online ordering: <http://www.ntis.gov>

Geophysical Methods for Stratigraphic Identification

September 2020

Judy Robinson
Rob D Mackley
Mark Rockhold
Tim Johnson
Jonathan Thomle
Christian Johnson
Piyoosh Jaysaval

Prepared for
the U.S. Department of Energy
under Contract DE-AC05-76RL01830

Pacific Northwest National Laboratory
Richland, Washington 99354

Summary

The goal of this work is to identify geophysical methods that can be used to delineate (in 3D) a large-scale paleochannel that has been inferred to exist between the 200 West and 200 East Areas of the Hanford Site's Central Plateau. This paleochannel is of particular importance because it will significantly impact flow and contaminant transport from 200 West to 200 East. Its high permeability can both accelerate contaminant transport and lower contaminant concentrations through spreading. Information about the spatial extent and structure of such features is needed to inform subsurface flow and contaminant transport models that support remedy decisions at Hanford.

The viability of several geophysical methods for stratigraphic characterization was assessed, including electrical resistivity tomography (ERT), electromagnetic, ground penetrating radar, and seismic. In addition, geophysical surveys previously executed at the Hanford Site were reviewed with respect to informing stratigraphy. Field investigations using seismic, electromagnetic, and ERT methods have ranged from kilometer-scale mapping of supra-basalt sediments to meter-scale studies used to identify borehole and well locations within a plume footprint. Since some of these datasets have not yet been fully interpreted in 3D, the existing datasets can be further assessed for potential contributions to the geologic framework model.

Of all the reviewed geophysical methods, ERT was identified as a robust approach for identifying major structural features in the deep subsurface. Coupled groundwater-ERT simulations were also used to assess the ability of using ERT to delineate the paleochannel. The groundwater model provided data on physical properties and tracer concentrations converted to electrical conductivity, and the ERT simulation code E4D was used to evaluate the efficacy of replicating these conductivity distributions from synthetic ERT data.

Multiple conceptual models were used to assess the impact of varying hydrological parameters on the imaging results, including tracer volume, tracer concentrations, and petrophysical parameters. The horizontal structure of the paleochannel could only be imaged with limited vertical resolution unless a conductive tracer was injected into the subsurface to provide a contrast in electrical conductivity. Results of a conductive tracer simulation indicated that time-lapse ERT monitoring could be used to delineate the large-scale paleochannel but depended on the uncertainty associated with the geoframework model and parameters used in the conceptualization. Simulation results also indicated that a multi-year monitoring period would be required for the injected tracer to laterally migrate the hundreds of meters needed to fully characterize the paleochannel.

A 2D field ERT campaign was also conducted between the 200 West and East Areas to obtain site-specific data to confirm feasibility of mapping paleochannels with ERT and reduce uncertainty from synthetic modeling. Using data quality, bulk conductivity structure, and estimated depth of investigation considerations, field results interpreted channel-like features as vertical contacts of high hydraulic conductivity zones horizontally separated by a lower permeability zone. These results support the use of additional static ERT imaging to delineate the paleochannel location, rather than using a tracer injection monitored with time-lapse ERT. A field campaign with additional 2D ERT lines is recommended so that a pseudo-3D analysis can be used to delineate the extent of the paleochannel feature(s) and guide locations for future characterization boreholes. The recommended static ERT imaging provides a cost-effective way of mapping the large-scale paleochannel while guiding borehole placement to confirm paleochannel extents identified with ERT.

Acknowledgments

This document was prepared by the Deep Vadose Zone - Applied Field Research Initiative at Pacific Northwest National Laboratory. Funding for this work was provided by the U.S. Department of Energy (DOE) Richland Operations Office. The Pacific Northwest National Laboratory is operated by Battelle Memorial Institute for the DOE under Contract DE-AC05-76RL0183.

Acronyms and Abbreviations

CCU	Cold Creek Unit
CRIM	Complex Refractive Index Model
EM	electromagnetics, active source
ERT	electrical resistivity tomography
FEM, FDEM	frequency-domain EM
GFM	geologic framework model
GPR	ground penetrating radar
HEIS	Hanford Environmental Information System
IP	induced polarization
LERF	Liquid Effluent Retention Facility
LIDAR	Light Detection and Ranging
MASW	multichannel analysis surface wave
NMR	nuclear magnetic resonance
NQAP	Nuclear Quality Assurance Program
OU	operable unit
P2R	Plateau-to-River
PNNL	Pacific Northwest National Laboratory
RLM	Ringold lower mud
TEM, TDEM	time-domain electromagnetics
SASW	spectral analysis surface wave

Contents

Summary	ii
Acknowledgments.....	iii
Acronyms and Abbreviations	iv
Contents	v
1.0 Introduction.....	1.1
1.1 Geophysical Surveys at Hanford	1.1
1.2 Report Organization.....	1.2
2.0 Hanford Site Geologic Description.....	2.1
3.0 Overview of Geophysical Methods	3.1
3.1 Electrical Resistivity Tomography	3.2
3.1.1 Induced Polarization.....	3.2
3.2 Active Source Electromagnetics	3.3
3.3 Seismic.....	3.5
3.4 Ground Penetrating Radar.....	3.8
3.5 Magnetism.....	3.9
4.0 Previous Geophysical Surveys Done to Identify Preferential Flow Pathways at Hanford	4.1
4.1 Electromagnetics and Integration Investigations	4.1
4.2 Seismic and Integrative Investigations	4.4
4.3 Electrical Resistivity Tomography	4.7
4.4 Ground Penetrating Radar.....	4.9
4.5 Conclusions / Recommendations of Previous Work.....	4.12
5.0 Pre-field Feasibility Evaluation of Electrical Resistivity Tomography	5.1
5.1 Site Description.....	5.2
5.2 Simulation Description	5.4
5.2.1 Flow and Transport.....	5.5
5.2.2 Petrophysical Transform.....	5.8
5.2.3 Electrical Resistivity Tomography	5.9
5.2.4 Other Modeling Considerations.....	5.10
5.3 Simulation Results	5.12
5.3.1 Flow and Transport.....	5.12
5.3.2 Electrical Resistivity Tomography	5.13
5.4 Simulation Results Exploring Uncertainty	5.16
5.4.1 Flow and Transport.....	5.16
5.4.2 Background/Characterization Electrical Resistivity Tomography	5.18
5.4.3 Time-lapse Electrical Resistivity Tomography	5.20
5.5 ERT Feasibility Evaluation Conclusions	5.26
6.0 ERT Field Evaluation	6.1

6.1	ERT Array Design	6.2
6.1.1	Field Setup.....	6.2
6.1.2	Data Collection	6.3
6.2	ERT Modeling Considerations	6.5
6.3	ERT Survey Results.....	6.5
7.0	Summary and Recommendations	7.1
7.1	Geophysical Surveys at Hanford	7.1
7.2	Paleochannel Evaluation.....	7.1
8.0	Quality Assurance.....	8.1
9.0	References.....	9.1
	Appendix A – Tracer Injection Considerations	A.1

Figures

Figure 2.1.	Hanford Site stratigraphy with geologic time scales from Lanigan et al. 2010 (Fig 6.4).....	2.1
Figure 2.2.	Cold Creek Unit facies and main paleochannels within the Central Pasco Basin (Martin 2010, Figure 3-6).....	2.2
Figure 2.3.	Multiple buried paleochannels in the Gable Gap area from Bjornstad et al. (2010), Fig 6.3.....	2.3
Figure 2.4.	Generalized stratigraphic relationship among post-Ringold units for Central Pasco Basin (Figure A.4, DOE 2002).....	2.4
Figure 3.1.	A typical electrical resistivity tomography (ERT) measurement where a current I is injected across current electrodes C+/C- and the resulting potential field ΔV is measured across two potential electrodes P+/P-. Photo credit: A. Binley, Lancaster Univ., UK.....	3.2
Figure 3.2.	A) Schematic airborne EM system and induced vs. measured fields; B) frequency-domain EM primary and secondary fields at receiver; C) time-domain EM transmitter and receiver waveforms (Legault 2015, Figure 1).....	3.4
Figure 3.3.	Principles of seismic methods (from Schuck and Lange 2007, Fig 4.6-1).....	3.7
Figure 3.4.	Ground penetrating radar ray paths (from Neal 2004, Figure 4).....	3.8
Figure 3.5.	Schematic diagram showing the declination (D) and inclination (I) of the total field vector F. Declination is the angle between true north and magnetic north (11.5 degrees). F is caused by the superimposed presence of magnetic minerals and rocks at that location (from Figure 6.12, Haldar 2018).....	3.9
Figure 4.1.	Comparison of 50-m resistivity depth slice of the RESOLVE FEM survey in a) and the HeliGEOTEM in b) (from Figure 10, Fugro Airborne Surveys 2010).....	4.3
Figure 4.2.	Ground-based EM-34 model (top) and 2D resistivity model (bottom) (Figure 4-1, CHPRC 2010b). The dashed yellow-blue line in both images depicts the water table boundary.....	4.4
Figure 4.3.	Pre-stack depth-migrated seismic results from a landstreamer survey northwest of 200 East Area interpreting the basalt boundary and potential locations of faults (orange) (Figure 8 from Hyde et al. 2011).....	4.5

Figure 4.4. Profile Line 2 was collected along a west-to-east profile north of the LERF basins. The interpreted basalt boundary is shown as dashed dark pink (top) and black (middle, bottom) lines. The Hanford formation is separated into two horizons, an upper (dashed green line) and lower (dashed pink line) (Figure 5, CHPRC 2012).	4.6
Figure 4.5. a) Hanford formation thickness estimated from waterborne electrical imaging. Low stage temperature measurements collected on b) 3/31/2009 and c) 8/2/2009. Red contours represent uranium concentrations (Slater et al. 2010, Figure 8).	4.8
Figure 4.6. Plan view ERT image of high stage river water intrusion within the saturated zone. The colored isosurfaces contour the negative changes in EC with respect to baseline conditions, indicating the presence of river water. River water intrusion flows preferentially through two features interpreted as high permeability paleochannels (Johnson et al. 2015, Figure 11b).	4.9
Figure 5.1. The Hanford South geologic framework model (CHPRC 2016) between 200 East and West on the Central Plateau. The Hanford formation has been removed to demonstrate the general shape of a paleochannel between 200 East and West as inferred by areas of lower elevation.	5.1
Figure 5.2. Hanford South geologic framework model (CHPRC 2016) at an elevation of 120 m in the saturated zone. The time-lapse ERT simulations focus on depths at or below this elevation.	5.2
Figure 5.3. Central Plateau Geoframework (CHPRC 2019, 2018a,b) at an elevation of 120 m in the saturated zone. This figure represents an updated geologic framework model from the image shown in Figure 5.2.	5.3
Figure 5.4. a) Proposed electrode placement and injection well locations used in the geophysical simulations; and b) magnified site view with groundwater flow directions with yellow arrows.	5.4
Figure 5.5. The relationship between potassium bromide (KBr) concentration and fluid conductivity (from Isono 1984).	5.9
Figure 5.6. A comparison of HEIS nitrate concentrations and fluid specific conductance from boreholes within and surrounding the area between 200 East and West Areas between 12/12/1983 and 11/2/2018.	5.11
Figure 5.7. Results of flow and transport simulations of a tracer injection into wells 699-49-69 and MW-10A at elevation 120 m. Shown are plan views of the model domain aqueous concentrations after the tracer injection ceased in 2020 a) 2020.25; b) 2020.5; c) 2021; d) 2025; e) 2027; f) 2034.	5.13
Figure 5.8. Flow and transport σ in plan view a) and elevation view b). Background ERT σ images are shown in plan view c) and elevation view with a 5:1 vertical exaggeration d). Color scales are one order of magnitude lower for the ERT σ relative to the flow and transport model σ to highlight the variability in conductivity structure of the ERT σ , which would otherwise not be visible.	5.14
Figure 5.9. Time-lapse ERT σ results alongside flow and transport σ conceptual site models. Both models are represented as isosurfaces of logarithmic change from background (year 2020) values. Simulations results are shown after the tracer injection has ceased at a) 2020.25; b) 2020.5; c) 2021; d) 2025; e) 2027; and f) 2034.	5.15
Figure 5.10. Tracer injection models at elevation 120 m from flow and transport simulations for Models 1, 2, and 3 with a tracer volume of 757 m ³ and a tracer concentration of 60 g/L.	5.17

Figure 5.11. Bulk EC Models 1 and 3 shown for the comprehensive survey where $m=1.3$. Flow and transport σ are shown for A) Model 1 and B) Model 3. Corresponding ERT modeling results are shown in C) and D)..... 5.18

Figure 5.12. Bulk EC Model 2 shown for the comprehensive survey. Flow and transport σ are shown for A) $m=1.3$ and B) $m=1.8$. Corresponding ERT modeling results are shown in C) and D)..... 5.19

Figure 5.13. ERT Bulk EC for Model 2 comparing imaging results when using A) comprehensive survey and B) focused survey. 5.19

Figure 5.14. Average changes in $\Delta \log \sigma_{app}$ for Models 1, 2, and 3 with the focused ERT survey. A tracer concentration of 60 g/L and a tracer volume of 757 m³ (200,000 gallons) at two injection locations were used. 5.21

Figure 5.15. Average changes in $\Delta \log \sigma_{app}$ from 2020 using Model 2 and the focused ERT survey. tracer concentration of 60 g/L and a tracer volume of 757 m³ (200,000 gallons) at two injection locations were used. 5.21

Figure 5.16. Average changes in $\Delta \log \sigma_{app}$ from 2020 using Model 2 and the focused ERT survey for different volumes of injected tracer. A tracer concentration of 60 g/L at two injection locations was used..... 5.22

Figure 5.17. Average changes in $\Delta \log \sigma_{app}$ from 2020 using Model 2 and the focused ERT survey for different concentrations of injected tracer. A tracer volume of 757 m³ (200,000 gallons) at two injection locations was used..... 5.22

Figure 5.18. Average changes in $\Delta \log \sigma_{app}$ from 2020 using Model 2 resulting from different measurement configurations. A tracer concentration of 60 g/L and a tracer volume of 757 m³ (200,000 gallons) at two injection locations were used. 5.23

Figure 5.19. Synthetic Models 1, 2, and 3 at elevation 120 m for a 60 g/L tracer injection for years 2020.5, 2022, and 2028. Archie parameters used in the synthetic modeling were $m=1.3$ and $n=2$ 5.24

Figure 5.20. Synthetic Model 2 at elevation 120 m using a 60 g/L tracer injection for years 2020.5, 2022, and 2028 for injection volumes 378 m³, 757 m³, and 1135 m³. Archie parameters used in the synthetic modeling were $m=1.3$ and $n=2$ 5.25

Figure 5.21. Synthetic Model 2 at elevation 120 m with an injection volume of 757 m³, with 40, 60, and 80 g/L tracer concentration for years 2020.5, 2022, and 2028. Archie parameters used in the synthetic modeling were $m=1.3$ and $n=2$ 5.26

Figure 6.1. Field location of the ~1.6-km ERT line between the 200 East and West areas: A) the location in relation to 200 East and West on the Central Plateau; B) aerial image showing 64 electrodes (~25 m spacing)..... 6.2

Figure 6.2. Field site data collection images: A) representative field site image showing installation of electrodes; B) polycase[®] box containing connector cable and ERT hookups with four electrodes penetrating to the surface; C) MPT-DAS1 system for field data collection. 6.3

Figure 6.3. Electrode measurement configurations used in the ERT survey, including A) Wenner-Alpha, B) Schlumberger, C) Multiple gradient, and D) dipole-dipole. C1 and C2 are current source and sink, respectively. P1 and P2 are the potential source and sink, respectively. 6.4

Figure 6.4. Modeled resistance versus measured resistance for each of the 5,003 ERT measurements..... 6.6

Figure 6.5. A comparison of A) the geologic framework model (CHPRC 2019, 2018a,b) compared to B) the ERT inversion results. The shaded gray region in B) represents poorly resolved ERT zones. Refer to Table 5.2 for stratigraphic unit abbreviations shown in the legend for A). 6.7

Figure A.1. P2R 100-year tracer transport simulation showing the maximum extent of plume migration in the Central Plateau. A.2

Figure A.2. P2R 500-year tracer transport simulation showing the maximum extent of plume migration in the Central Plateau. A.3

Tables

Table 2.1. Stratigraphic studies^(a) that specifically mention paleochannels on the Hanford Site..... 2.4

Table 4.1. Previous geophysical methods used to investigate paleochannels at Hanford..... 4.11

Table 5.1. Input parameters for Phase 1 flow and transport model simulations. 5.5

Table 5.2. Input parameters for Phase 2 flow and transport model simulations. 5.6

Table 5.3. Phase 1 conceptualization used in ERT feasibility evaluation..... 5.10

Table 5.4. Phase 2, Models 1 and 3 Conceptualizations used in ERT feasibility evaluation 5.10

Table 5.5. Phase 2, Model 2 conceptualizations used in ERT feasibility evaluation..... 5.10

Table 6.1. Reciprocity analysis. 6.5

Table A.1. Parameters for KBr simulations..... A.2

1.0 Introduction

Stratigraphy has typically been mapped on the Central Plateau at the Hanford Site using information from borehole data. These data include borehole characterization and downhole geophysical logs, grain-size analyses from sediment samples, as-built diagrams, and/or sediment photographs (Bjornstad et al. 2010; DOE 2002). Representations of the available data include maps of the upper surface elevations or “tops” of the major hydrostratigraphic units interpolated between borehole locations. Where boreholes are sparse or subsurface heterogeneity exists at length scales smaller than the distance between the boreholes, the uncertainty in the interpolation of hydrostratigraphic surface elevations is high. Moreover, data at each borehole may not contain all these data types, which increases the uncertainty in interpreting among boreholes.

Across the Central Plateau, buried ancestral fluvial channels, or paleochannels, have been inferred from numerous borehole datasets. Paleochannels filled with coarse sediments act as preferential groundwater and contaminant pathways, and therefore can shorten travel times to downgradient receptors (e.g., the Columbia River) while also potentially diluting contaminants to below the maximum contaminant levels because of increased groundwater flow. Main paleochannels identified are north of the 200 East Area, which is where the ancestral Columbia River was located, and south of the 200 West Area, the remnant location of Cold Creek. Northwest of 200 East Area, within the Gable Gap area, at least six buried paleochannels have been identified from borehole and seismic datasets, with five carved out from Pleistocene Ice Age floods (Bjornstad et al. 2010). Paleochannels play an important role in contaminant transport across the Central Plateau, and delineation of these features is critical to effective environmental management and remediation.

Aside from physical characteristics determined from borehole data, monitoring of contaminant concentrations in groundwater provides indirect evidence of the connectivity of subsurface features in the Central Plateau. An extensive groundwater monitoring program exists on the Hanford Site (DOE 2017) that uses thousands of wells whose locations are based in part on source locations and contaminant plume concentrations. Based on the available data, paleochannels have been inferred at several other locations, including southeast of the 200 East Area and in between the 200 East and West Areas. The boreholes in these areas are relatively sparse, and therefore the interpretation of the hydrostratigraphy and the impact on contaminant transport predictions between the 200 Areas is uncertain. Improved methods are needed to provide information at a scale consistent with supporting groundwater operable units and remedy implementations.

1.1 Geophysical Surveys at Hanford

Previous studies at the Hanford Site have identified several geophysical methods that are fast and cost-effective investigative tools (e.g., Gander et al. 2011; Murray and Last 2005; Strickland et al. 2018). Geophysical methods non-invasively collect measurements in airborne and surface surveys. Depending on the spacing of sensors, resolution can be from centimeter to kilometer scale. On the Hanford Site, stratigraphy interpreted from borehole data has been integrated with surface geophysics to create hydrogeologic models (Bjornstad et al. 2010) and used to validate findings from geophysical surveys collected on or above the ground surface (CHPRC 2010a). However, many of the waste management areas at the Hanford Site contain a large amount of metallic infrastructure and many electromagnetic sources (e.g., power lines), which has limited the effectiveness of electromagnetic geophysical surveys (e.g., CHPRC 2010b). Sources of data noise can be accounted for in some cases, as in a recent re-examination of surface electrical resistivity in the B-Complex (Johnson and Wellman 2013). Interference from buried pipes, tanks, and well casings were removed in the electrical resistivity modeling performed

by Johnson and Wellman (2015) to more accurately predict subsurface distributions of electrical conductivity.

While challenges exist in using geophysical methods on the Hanford Site, these methods have the potential to provide information that complements existing borehole data, as well as guides future borehole placement. For example, although geophysical methods do not provide direct information on grain-size distributions or hydraulic conductivity, relative differences in lithologies can be inferred. Although the magnitude of contaminant concentrations cannot be measured by geophysics, the spatial extent of a plume can be visualized so that contrasting conductivity zones can be delineated. Geophysical methods are sensitive to physical and/or chemical characteristics in the subsurface. Therefore, the effectiveness of a geophysical method may depend on the characteristics of the target and the goals of the survey.

The purpose of this report is to identify and recommend geophysical methods that may be effective at delineating high permeability paleochannels in the subsurface at the Hanford Site. This was achieved by:

1. Reviewing and evaluating historical field investigations on the Hanford Site, where geophysical methods were used to identify lithologic contacts and paleochannels. The review encompassed multiple geophysical methods at varying scales of data acquisition to identify successes and lessons learned in the interpretation of data collected in geophysical surveys.
2. Executing hydrogeophysical simulations to assess the feasibility of using the geophysical method electrical resistivity tomography (ERT) for characterization imaging with an injected ionic tracer. An ionic tracer is used to enhance the contrast in electrical conductivity between the injected tracer solution and ambient groundwater. The area of interest is between 200 East and West, where a scarcity of boreholes creates uncertainty in the paleochannel spatial extent (CHPRC 2016).

The hydrogeophysical simulations were performed in two steps. Step 1 consisted of a single conceptualization by which to evaluate ERT. In step 2, multiple conceptualizations were used to evaluate uncertainty.

3. Conducting a 2D ERT field campaign between the 200 West and East Areas to assess data noise, signal strength, depth of investigation, and bulk electrical properties. The primary goal of the assessment was to determine whether the lithologic contrast in bulk physical properties could be detected using ERT, determine if these were comparable to the geologic framework model (GFM), and identify site-specific parameters for use in the modeling.

1.2 Report Organization

Section 2 of this report provides a brief overview of Hanford Site stratigraphy, focusing on identification of high permeability paleochannels. In Section 3, a review of geophysical methods used at the Hanford Site is provided, followed by a review and evaluation of Hanford geophysical field investigations in Section 4. Computer simulations used to evaluate the use of ERT for paleochannel identification are presented in Section 5. Section 6 contains the ERT field evaluation details and results. Conclusions and recommendations for additional characterization activities are provided in Section 7. Appendix A contains an overview of permitting requirements for a site tracer injection.

2.0 Hanford Site Geologic Description

The generalized stratigraphy at the Hanford Site (Figure 2.1) consists of five lithostratigraphic units, listed here in stratigraphic order from upper (shallow) to lower (deep): eolian and alluvial Holocene sediments (< 1 m thickness); glacio-fluvial deposits associated with cataclysmic ice-age flooding in the Hanford formation; alluvial, fluvial, and paleosol deposits in the Cold Creek Unit (CCU); alluvial and lacustrine deposits in the Ringold Formation; and the Columbia River Basalt Group. These units are subdivided into finer-scale features or facies that depend on the proximity to ancient river systems and floodpaths. Refer to Martin (2010) and DOE (2002) for a complete description of lithology and hydrostratigraphic units.

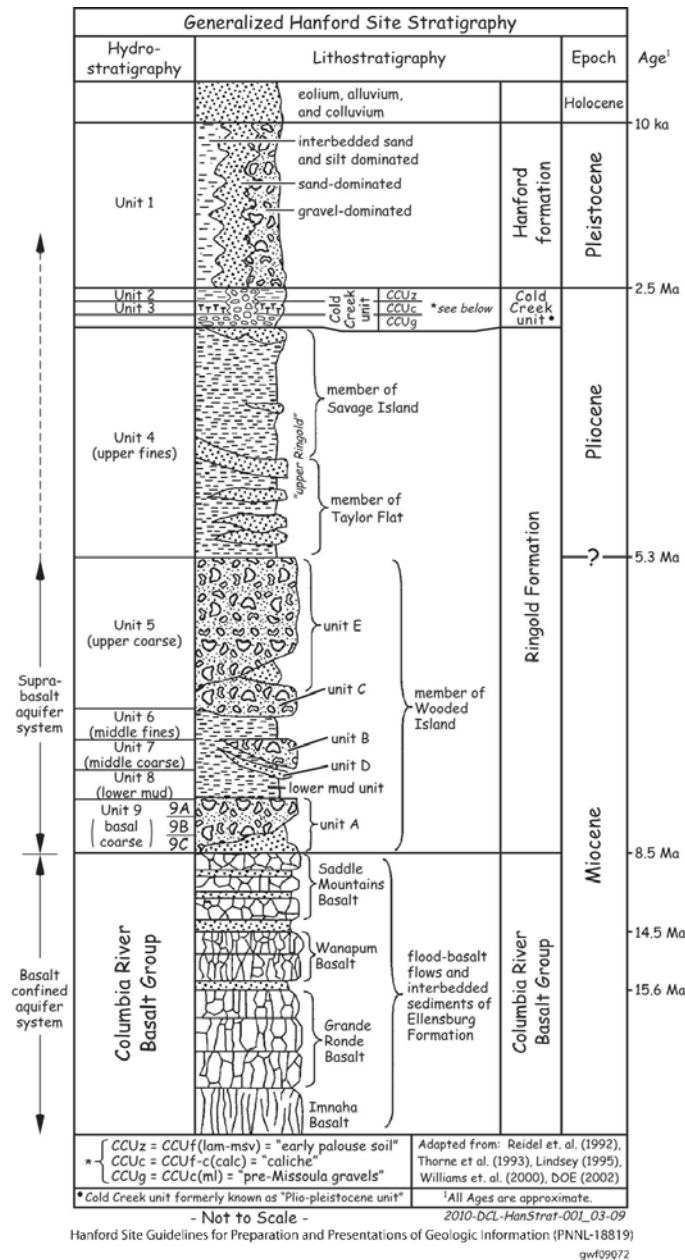


Figure 2.1. Hanford Site stratigraphy with geologic time scales from Lanigan et al. 2010 (Fig 6.4).

Field and laboratory studies have been conducted over a span of decades to characterize the lithology and stratigraphy and hence locate paleochannels at the Hanford Site (Table 2.1). Site-wide paleochannels associated with the ancestral Columbia River and cataclysmic Ice Age floods have been identified within the Ringold Formation and the CCU (Figure 2.2). The distribution of CCU units across the Hanford Site and monitored groundwater contaminants can imply where additional paleochannels may be located. For example, a detailed study of the Gable Gap area identified multiple buried paleochannels inferred from dozens of borehole and seismic-reflection data (Bjornstad et al. 2010). Five of the six paleochannels identified (A-E, Figure 2.3) had Ringold sediments removed from extreme erosion that occurred during Ice Age flooding. These paleochannels contain highly permeable Hanford formation deposits.

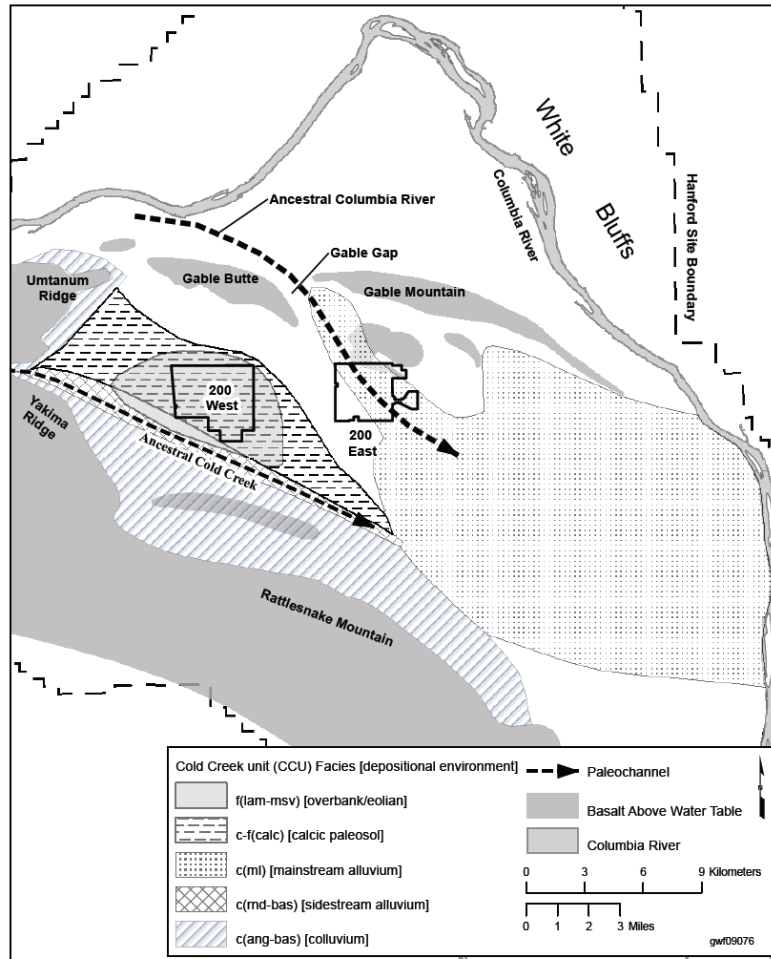


Figure 2.2. Cold Creek Unit facies and main paleochannels within the Central Pasco Basin (Martin 2010, Figure 3-6).

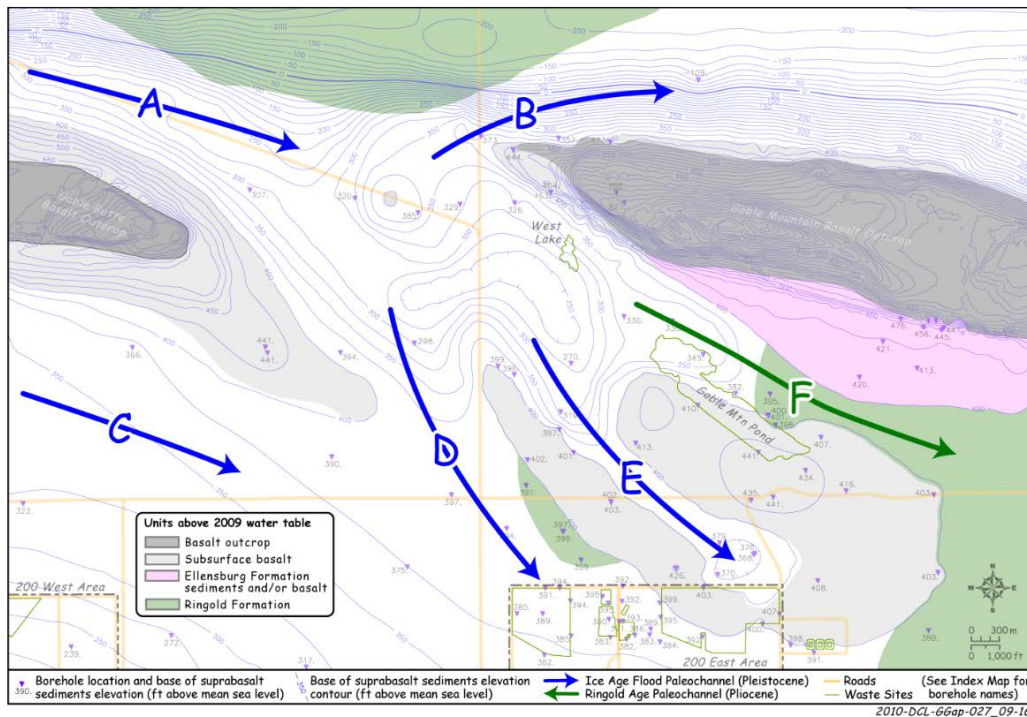


Figure 2.3. Multiple buried paleochannels in the Gable Gap area from Bjornstad et al. (2010), Fig 6.3.

Figure 2.4 shows a conceptual model of a paleochannel in the Central Pasco Basin. This figure includes sediments of the CCU, the Hanford formation, and overlying Holocene deposits. High-energy Hanford formation gravel deposits are shown to have scoured the CCU, and in some places to have direct contact with underlying Ringold Formation or Basalt Group (not shown in diagram). Laterally, a borehole cross section across the 200 West Area showed facies changes within the CCU and Hanford formation (DOE 2002, Figure A-5), suggesting a complex erosional pattern from flow paths of ancestral riverbeds and floods.

The Ringold Formation is divided into six Pliocene- to Miocene-aged facies ranging from coarse to fine-grained sediments. The Ringold lower mud (RLM) unit is a silty layer between coarser facies (refer to Figure 2.1). On the eastern boundary of the 200 West Area, the GFM (CHPRC 2016) predicts the RLM is truncated by coarser units, indicating the possibility of transmissive paleochannel within coarser Ringold sediments between the 200 East and West Areas.

Table 2.1. Stratigraphic studies^(a) that specifically mention paleochannels on the Hanford Site.

Report Reference	Year	Title
Fecht et al. 1985	1987	Paleodrainage of the Columbia River System on the Columbia Plateau of Washington State - A Summary
Williams et al. 2000	Apr 2000	Revised Hydrogeology for the Suprabasalt Aquifer System, 200-East Area and Vicinity, Hanford Site, Washington
Williams et al. 2002	May 2002	Revised Hydrogeology for the Suprabasalt Aquifer System, 200-West Area and Vicinity, Hanford Site, Washington
DOE 2002	June 2002	Standardized Stratigraphic Nomenclature for Post-Ringold-Formation Sediments Within the Central Pasco Basin
Bjornstad and Lanigan 2007	Sept 2009	Geologic Descriptions for the Solid-Waste Low Level Burial Grounds
Martin 2010	2010	Chapter 3: Overview of Hanford Hydrogeology
Bjornstad et al. 2010	Sept 2010	Hydrogeologic Model for the Gable Gap Area, Hanford Site
DOE/RL-2011-118, Rev. 0	Aug 2012	Hanford Site Groundwater Monitoring for 2011
Reidel and Tolan 2013	2013	The late Cenozoic evolution of the Columbia River system in the Columbia River flood basalt province

(a) And references therein

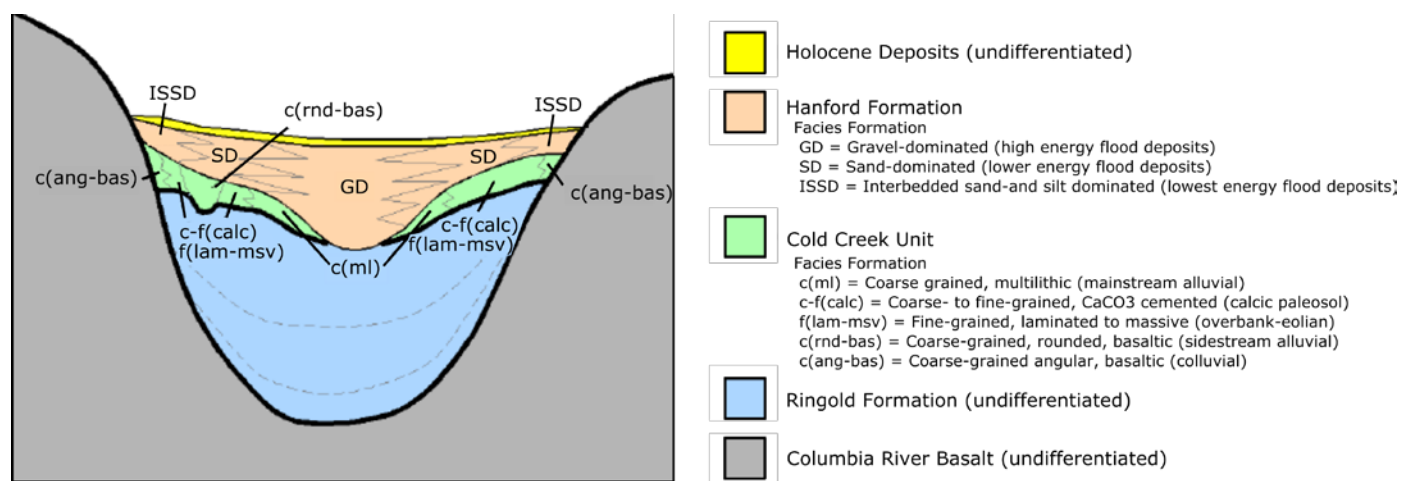


Figure 2.4. Generalized stratigraphic relationship among post-Ringold units for Central Pasco Basin (Figure A.4, DOE 2002).

3.0 Overview of Geophysical Methods

Geophysical methods measure variations in the electrical conductivity, magnetic susceptibility, seismic velocity, and gravity-induced changes in density using minimally- or non-invasive instrumentation for rapid data acquisition. The relative ease of implementation, low cost, and large interrogation volumes complement, in situ water sampling at monitoring wells. Geophysical methods can be selected and tuned to provide information at scales relevant to information needed for characterization and monitoring of groundwater operable units. Additional data (e.g., borehole stratigraphic descriptions, hydraulic properties, aqueous chemical data) can be used in conjunction with geophysical interpretation to better interpret subsurface structure and properties relevant to subsurface flow and transport processes.

To provide context for geophysical surveys performed at Hanford and described in Section 4.0, an overview of relevant geophysical methods is provided here. This review is limited to geophysical technologies that have been used on the Hanford Site and that may be relevant to paleochannel identification. This includes ERT, active source electromagnetics (EM), seismic techniques, ground penetrating radar (GPR), and magnetics. The following methods, however, are not considered in this review because they are not considered relevant to paleochannel characterization:

- **Single borehole methods (e.g., geophysical borehole logging).** Borehole geophysical data has the same limitation as more traditional borehole datasets: The spatial information is limited to the region surrounding the borehole and identification of a paleochannel is through interpolation of these datasets. While borehole datasets can be used to ground-truth other datasets, the objective here is to identify geophysical methods that can be used for paleochannel identification at a regional scale.
- **Magnetotellurics (passive source electromagnetics).** This is typically used for deep investigation (>100 m) and is not applicable to paleochannel identification on the Hanford Site, where the relevant depth is within the top 100 m.
- **Surface nuclear magnetic resonance (NMR).** This method, while excellent at detecting subsurface fluid and saturation variations, is extremely sensitive to ambient electromagnetic noise. The magnitude of the noise can often exceed the magnitude of the NMR signal (Behroozmand et al. 2014). Until there are improvements in hardware and software-based signal processing to remove this unwanted signal, the ambient noise (e.g., power lines) on the Hanford Site makes this method impracticable.
- **Gravity / Microgravity.** Gravity as a geophysical method is sensitive to density contrasts in the surface. ASTM Standard D 6429-99, *Selection of Geophysical Methods for Common Applications* (ASTM International 1999), defines voids and sinkholes, fractures and fault zones, and bedrock depths as good targets for gravity surveys. At the Hanford Site, gravity was used to identify buried bedrock features to understand the geology of the Pasco Basin (Richard et al. 1977). More recently, density within three boreholes was measured with a gravity survey at the Hanford Waste Treatment and Immobilization Plant for seismic modeling (MacQueen and Mann 2007). However, beyond borehole investigations, gravity as a geophysical technology at the Hanford Site deemed site noise a limiting factor (Murray and Last 2005). There are no recent uses of gravity that capture information at the spatial extent needed for paleochannel identification, and this is presumably due to site noise and/or lack of sensitivity to the density contrasts of paleochannels.

This method overview section is not intended to be comprehensive, but references are provided for readers interested in obtaining more detailed information on the geophysical methods.

3.1 Electrical Resistivity Tomography

ERT is sensitive to bulk electrical conductivity (the inverse of electrical resistivity) in the subsurface. Electrical conductivity is affected by physical properties, including lithology, pore water fluid conductivity, porosity, moisture content, and temperature. ERT is an active source geophysical method where an electric potential field is generated in response to a current injection I across two transmitting electrodes (Figure 3.1). The resulting change in potential ΔV is recorded across two receiving electrodes (Ward 1988). Assuming low surface conduction, electrolytic current pathways closely mimic hydraulic pathways, and distributions of electrical conductivity can be used to infer subsurface structure or migration of an ionic fluid (Falzone et al. 2018). Electrical measurements are correlated to pore fluid properties (i.e., salinity, saturation) and lithology (i.e., porosity).

The spacing between the transmitting and receiving electrodes determines the spatial resolution and volume of interrogation of each measurement. The spacing between electrodes can range from a few centimeters up to hundreds of meters. Electrodes with spacings that are farther apart sample a larger volume with lower spatial resolution. In comparison, closer spaced electrodes sample a smaller volume with higher spatial resolution. The interrogation volume is highly scalable depending on the spacing of electrodes.

ERT measurements can be collected on the surface or in boreholes. Surface electrodes are typically metal rods that penetrate the ground surface several centimeters or as shallow as necessary to have electrical contact with the subsurface. Borehole electrodes can be installed along the outer diameter of non-metallic well casing as low-profile metal clamps or within an open well using metallic electrodes along an electrical cable (Robinson et al. 2015). If the installation is below the water table, contact with the formation is maintained through the groundwater fluid. In vadose zone studies using borehole deployed ERT arrays along well casing, electrical contact with the formation is maintained via the backfill or grout in the borehole annulus.

Once electrodes are installed, they can be left in place to monitor changes from an initial state (Singha et al. 2014). Time-lapse ERT methods offer an advantage over other geophysical methods because the competing effects of lithology, porosity, etc. can be eliminated by focusing on changes in electrical conductivity over time rather than on absolute conductivity.

3.1.1 Induced Polarization

An induced polarization (IP) survey measures the stored charge or polarization response of an injected current in the subsurface and is highly dependent on mineral surface area. Given the high sensitivity to mineral surface area, field IP surveys have the potential to more clearly identify lithological variations inferred from ERT results, which provides a more robust interpretation. In all cases, IP data are collected at the same time as an ERT survey: An ERT survey measures ΔV after shutoff of an injected current and

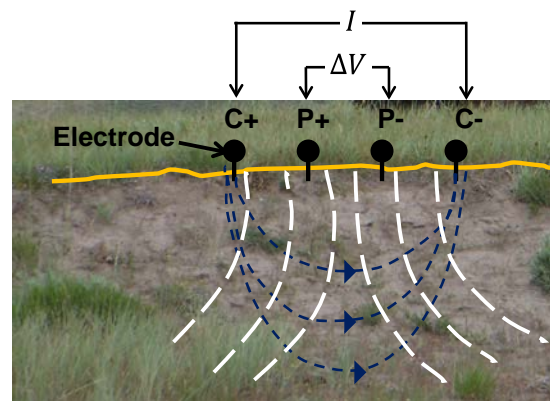


Figure 3.1. A typical electrical resistivity tomography (ERT) measurement where a current I is injected across current electrodes C+/C- and the resulting potential field ΔV is measured across two potential electrodes P+/P-. Photo credit: A. Binley, Lancaster Univ., UK.

an IP survey measures the voltage-decay (time-domain) or phase-lag (frequency-domain). Typically, the additional data collected from an IP survey results in additional data collection time, which can be prohibitive factor in some cases. When IP measurements are collected at multiple frequencies, it is referred to as spectral IP, or SIP.

Electromagnetic coupling can be a major obstacle in the interpretation of IP data (Routh and Oldenburg 2001). These effects can be observed at frequencies as low as 1 Hz but typically occur at higher frequencies (> 10 Hz). Capacitive coupling, which can arise from a leakage of displacement currents between transmitter and receiver wires or transmitter wires and the ground (Wynn 1974), can be minimized by separating the current and potential cables (Dahlin and Leroux 2012). Inductive coupling can manifest between wires or through induction within the earth and is more pronounced in conductive environments or where dipole lengths are large. While quasi-filtering (Binley 2015) and numerical solutions (Routh and Oldenburg 2001; Zhao et al. 2015; Kemna et al. 2014) have been proposed, more research is needed to characterize these effects if they are observed in a dataset.

3.2 Active Source Electromagnetics

Like ERT, EM is sensitive to bulk electrical conductivity in the subsurface. EM surveys are performed on or above the surface by passing a current through a transmitting wire coil, which then propagates a primary electromagnetic field above and below the ground. The magnetic component of the EM wave induces eddy currents in subsurface conductive material, producing a secondary EM field. Secondary EM field(s) are detected by a wire coil receiver and can be distinguished from the primary field (Figure 3.2). Secondary EM fields provide information about the geometry, size, and electrical properties of subsurface conductors.

EM systems are typically categorized by the positioning and/or layout of the transmitter and receiver. Small-loop EM systems are composed of a multiple or multiples of two small coplanar coils (i.e., a transmitter and receiver) separated by a fixed distance. These systems are moved along acquisition lines at a known position. The lengths of these systems can vary from 1 to 10 m, and can be held by an operator, mounted on a motorized vehicle, or deployed by airborne systems (e.g., mounted on a helicopter). Large-loop EM systems contain a polygon-shaped (e.g., square or hexagon) transmitter loop (5 to 200 m side length) consisting of a single conductor wire and a receiver antenna centered within the transmitter loop. These systems can be laid out on the ground or suspended from a helicopter (Figure 3.2) or small plane for an airborne survey.

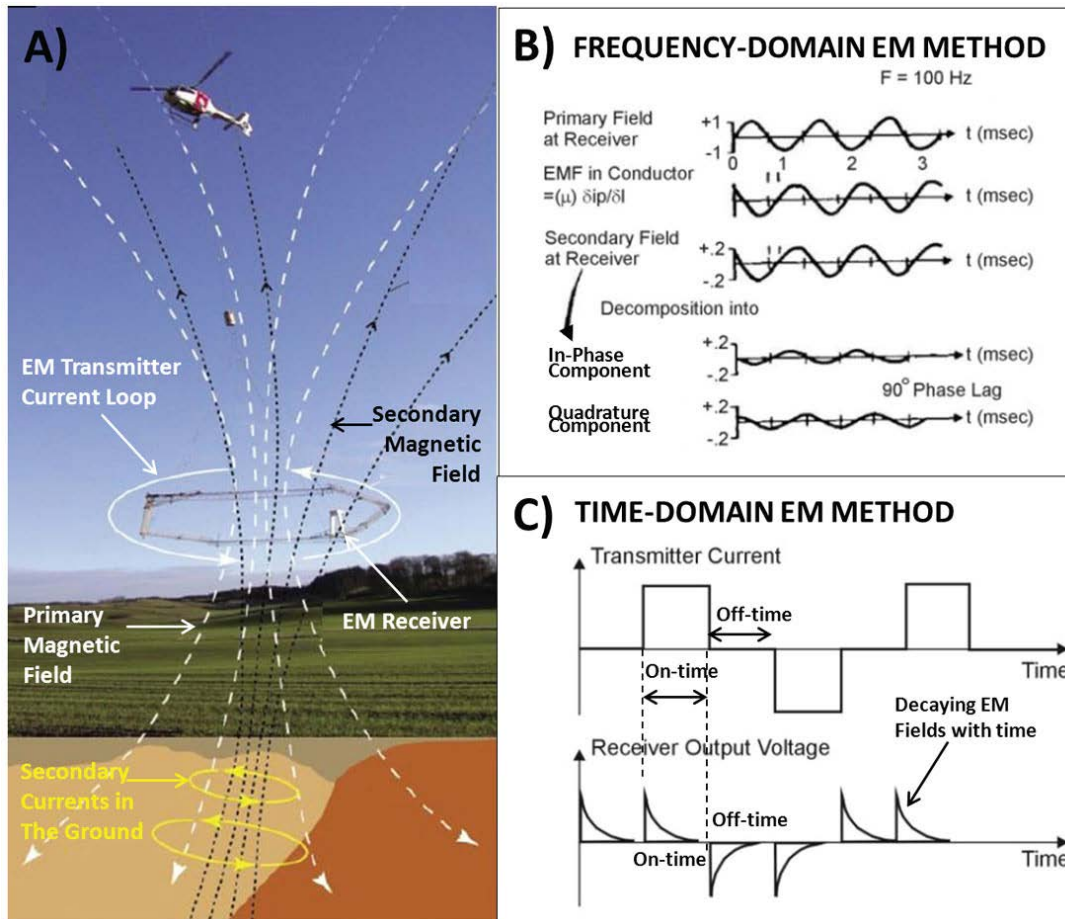


Figure 3.2. A) Schematic airborne EM system and induced vs. measured fields; B) frequency-domain EM primary and secondary fields at receiver; C) time-domain EM transmitter and receiver waveforms (Legault 2015, Figure 1)

Measurements can be collected as a function of time, for time-domain EM (TEM or TDEM), or at one or more frequencies, for frequency-domain EM (FEM or FDEM). In TEM, the transmitter emits a short duration symmetrical square wave voltage pulse and the secondary field is measured as the amplitude of the decay over time. Measurements at successively later times provide information at greater depths. The same coil can be used as the transmitter and receiver, but more often a separate receiver coil centered within the transmitter loop is used.

In FEM, the secondary field is commonly reported as the real or in-phase component and the quadrature or out-of-phase component. The in-phase component is responsive to discrete, highly conductive objects such as metal. In the absence of highly conductive objects, the magnitude of the in-phase component depends on the magnetic susceptibility. Using simplifying assumptions, the quadrature component is linearly proportional to the apparent conductivity of the subsurface.

The depth of exploration is a function of the time or frequency of the EM field and the electrical conductivity of the medium. The skin depth δ , defined herein as the depth at which the amplitude of a plane-wave electromagnetic field reduces to $1/e$ (0.378), is a common measure used to determine attenuation from the Earth's surface (Spies 1989):

$$\delta = \sqrt{\frac{2}{\sigma\mu\omega}} \quad (3.1)$$

where σ is the electrical conductivity, μ is the magnetic permeability, and ω is the angular frequency (where $\omega = 2\pi f$). Eq. (3.1) assumes σ and μ are frequency independent and that displacement currents can be ignored. Skin depth can be used as a first-order estimate of penetration depth. As shown in Eq. (3.1), as frequency and electrical conductivity increase, skin depth decreases. For airborne surveys, geometrical attenuation must also be considered in addition to frequency dependence. To this end, Beamish (2004) defined a vertical decay scale length, called a dipolar skin depth, and compared these results with plane-wave [Eq. (3.1)] skin depths. It was found that dipolar skin depths were much smaller than plane-wave skin depth except at frequencies > 50 kHz. Therefore, airborne EM survey skin depth estimates using Eq. (3.1) could potentially overestimate depth.

EM has several notable advantages over ERT, including faster data acquisition over larger areas and in land, air, and sea environments. Since EM is based on induction, the method does not require electrode contact with the ground. Disadvantages include a fixed depth of investigation based on the instrumentation frequency, the transmitter and receiver coil separation, and noise from non-geologic objects such as power lines and buried metallic objects.

3.3 Seismic

Seismic methods exploit the propagation of elastic energy in the subsurface and generally involve measuring the travel time of low-frequency acoustic energy from a source location, called a shot point, to motion sensors, called geophones, which transform seismic energy into an electrical voltage (Pelton 2012). From the surface, a seismic wave spreads out hemispherically into the subsurface, causing different particle motion orientations, which are used in the naming convention. Particle motions that are parallel and perpendicular to the direction of seismic wave propagation are compressional or ‘P’ waves and shear or ‘S’ waves, respectively. S-waves travel slightly slower than P-waves in solids and can only propagate in materials that have shear strength. P- and S- waves are also referred to as body waves since they penetrate the interior of the Earth. Surface waves travel primarily along the ground surface or at shallow depths and are characterized by elliptical motion perpendicular to the surface (Rayleigh waves) or perpendicular to the propagation direction (Love wave).

Acoustic energy sources are typically explosives, a weight drop, vibrators, or gas/air guns, and shot locations depend on survey objectives. On the surface, seismic surveys can be performed with stationary source and receiver locations or with towed arrays using gimbaled geophones. Within a borehole, seismic data can be obtained within a single borehole using a surface source location to a known depth (check-shots) or along an entire vertical profile. These data are often used with borehole geologic information and correlated to surface seismic data. Additionally, cross-well seismic tomography can be performed where a source is lowered in one borehole and stationary receivers in another borehole record the arrival of the seismic wave (Figure 3.3).

P- and S-body waves are refracted or reflected at interfaces with different velocities and/or densities (Figure 3.3). This signal is recorded in conventional reflection (Steeple 2005) or refraction surveys where the offset of sensors controls the investigation depth. In near-surface investigation, reflection survey depths can range from ten to hundreds of meters. For refraction surveys, the near-surface investigation depth can be less than 30 m, due in part to the long offset requirement where the length of the array must be at least five times the desired depth of interest. While refraction surveys are generally

less expensive, reflection surveys have better vertical resolution and are better for identifying deep, small targets (Rabbel 2010). The wave velocities of P-waves and S-waves can be readily obtained to solve for engineering properties such as Young's modulus (E), shear modulus (G), and either density or Poisson's ratio (ν).

Measurements of Rayleigh surface waves, also known as ground roll, can provide dispersion properties of the seismic wave as profiles of shear wave velocity. Spectral or multichannel analysis of surface wave surveys (SASW or MASW, respectively) can be used to determine 1D or 2D vertical profiles of shear wave velocity (Lin et al. 2017; Park et al. 2007) for soil profiling or depth to a basement basalt layer (Yaede et al. 2015). Typically, SASW and MASW surveys have a shallower depth of exploration than conventional reflection and refraction surveys.

Regardless of the type of seismic wave surveyed, the same methodology is used for each survey with different geometries and data processing procedures. The data are typically stacked (i.e., multiple traces are acquired and added together) to boost the signal-to-noise ratio. Raw seismic data collected from the surface cannot account for dipping reflectors or complex geology. Therefore, data migration is often performed, a process in which seismic data are geometrically re-located in either space (depth) or time. Depth migration is better at resolving lateral velocity variations; however, a velocity model is required to convert travel time to depth coordinates. Both pre- and post-stack migration can be performed. Seismic inversion is used to transform seismic data into a quantitative rock property, acoustic impedance, which is equal to the product of sonic velocity and bulk density.

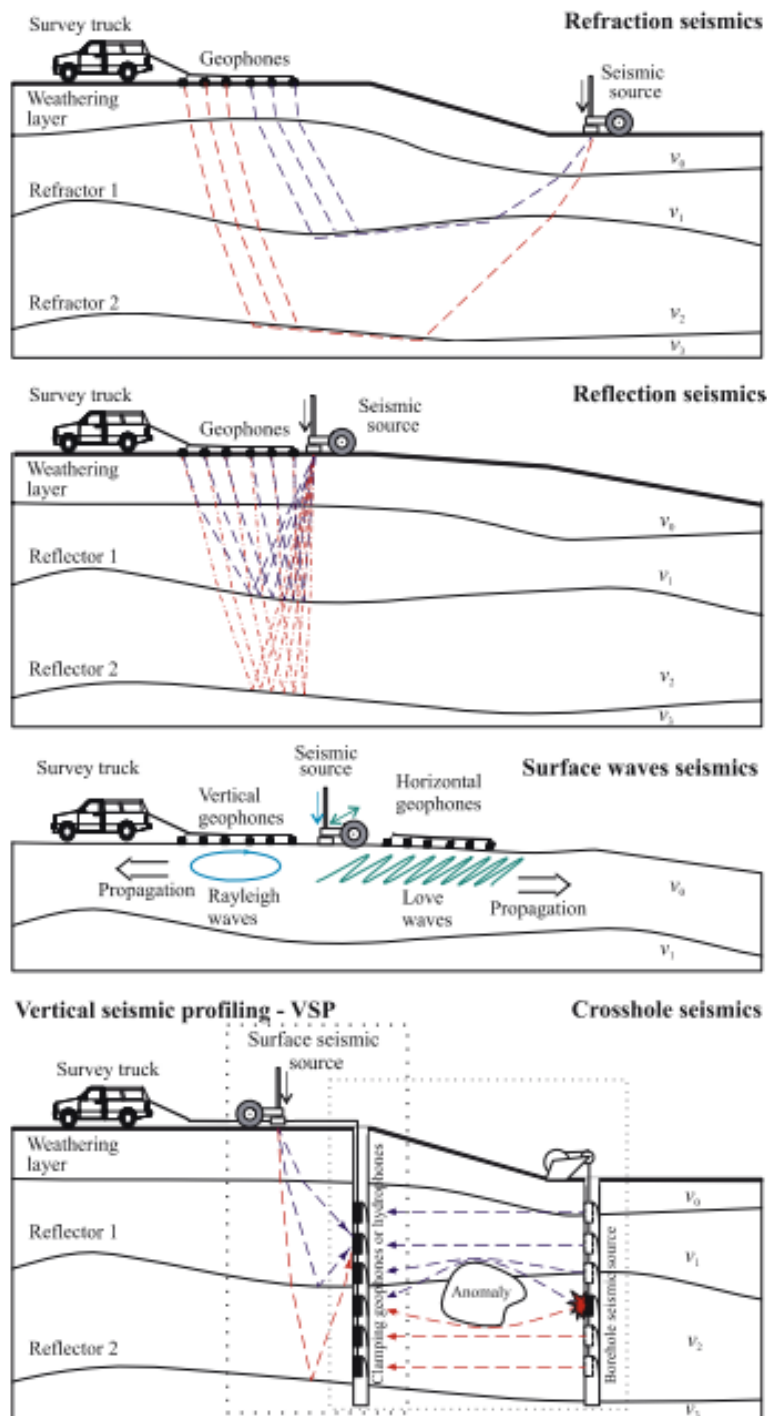


Figure 3.3. Principles of seismic methods (from Schuck and Lange 2007, Fig 4.6-1).

3.4 Ground Penetrating Radar

GPR is a shallow geophysical technique that uses the transmission and reflection of high-frequency (10 MHz to 1 GHz) EM energy (Annan 2009). Surface-based GPR data are acquired by sending an alternating pulse of EM energy into the earth from a transmitter antenna located at the earth's surface and recording energy that is reflected back to a receiver antenna located at the surface (Figure 3.4) or within a borehole. GPR images capture information about the large-scale architecture of the subsurface, and smaller-scale spatial variation. The most common survey technique is a common offset profile (COP), where data are collected at a fixed transmitter-receiver spacing. A COP radar image is essentially a pseudo cross-section of the subsurface displayed as arrival time and amplitude of energy arriving at the receiver. Reflected energy from subsurface interfaces occur due to changes in dielectric properties, so the GPR image is a representation of the variation in the dielectric properties of the subsurface.

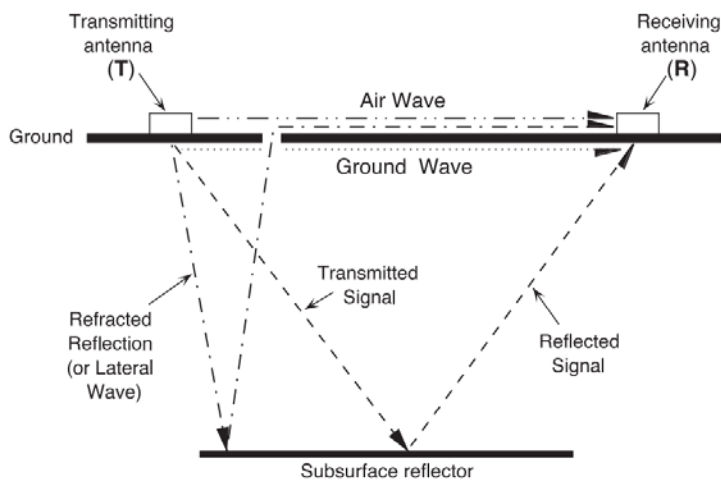


Figure 3.4. Ground penetrating radar ray paths (from Neal 2004, Figure 4).

Dielectric permittivity is measured in units of electrical capacitance (farads) per meter and represents the ability of a material to store electrical charge (Neal 2004). High frequency (1GHz) GPR data provides high spatial resolution but cannot penetrate very far into the subsurface. Conversely, lower frequencies (100 MHz) offer reduced spatial resolution with better depth of penetration (e.g., Smith and Jol 1995). Resolution of GPR waves is typically reported at one-quarter of the signal wavelength. Propagation of an EM wave in the subsurface depends not only on the dielectric properties (which

are to some extent frequency dependent) but also the electrical conductivity and magnetic permeability. In highly conductive environments (e.g., high clay content), energy losses can significantly reduce the penetration depth, making GPR impractical in areas where electrical conductivity of soils is relatively high.

Within the megahertz to gigahertz bandwidth, the permittivity of water is approximately 80, air is equal to 1, and soil is typically between 3 and 10. This large contrast makes GPR especially well-suited for estimating water content (Vereecken et al. 2008). Two commonly used relationships to estimate soil water content from dielectric permeability are a model proposed by Topp (1980) and the Complex Refractive Index Model (CRIM) (refer to Huisman and Hubbard 2003). Topp (1980) established an empirical relationship between measured permittivity and volumetric water content for a variety of mineral soils. CRIM is a mixing model that uses the volumetric fractions and dielectric permittivity of each soil constituent. By determining dielectric permittivity from GPR data, and applying these petrophysical relations, soil water content can be estimated from GPR data.

3.5 Magnetics

The magnetic geophysical method measures magnetic variations in the subsurface, which are primarily due to the presence of the Earth's magnetic field. The Earth's magnetic field is a dipole where magnetic field lines run from the South Pole (positive) to the North Pole (negative), inducing magnetism within rocks. Ferromagnetic minerals also create a magnetic field that may not be in alignment with the Earth's magnetic field. Known ferromagnetic materials are iron, nickel, cobalt, and alloys with titanium and aluminum (Spain and Venkatanarayanan 2014). Magnetism is measured as the sum of all magnetic fields measured in tesla (T) (Figure 3.5). Magnetic susceptibility (k) describes the ability of a rock to be magnetized and is the parameter of interest from magnetic data. The dimension of k is unitless and is the ratio of magnetization (the magnetic moment per unit volume) to the applied magnetizing field intensity.

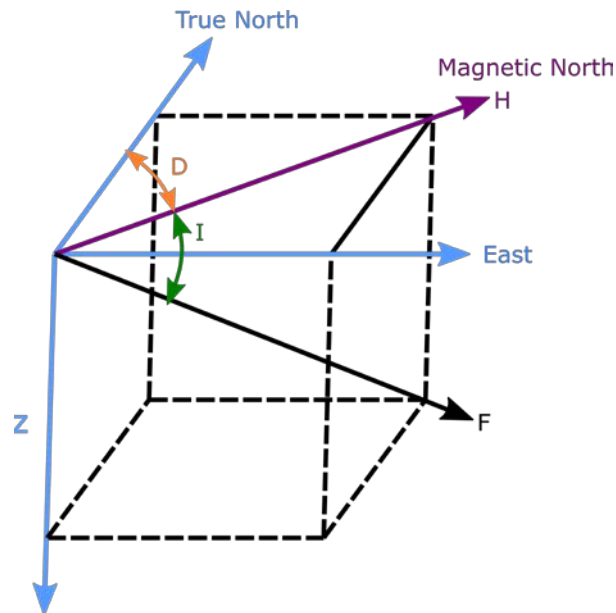


Figure 3.5. Schematic diagram showing the declination (D) and inclination (I) of the total field vector F . Declination is the angle between true north and magnetic north (11.5 degrees). F is caused by the superimposed presence of magnetic minerals and rocks at that location (from Figure 6.12, Haldrar 2018).

Measurements can be acquired from hand-held instruments in a laboratory, the ground surface, in boreholes, in airborne and ocean surveys, and in space. Magnetic fields external to the Earth have a large effect on magnetic measurements and these must be removed during post processing (Nabighian et al. 2005). These include solar winds and diurnal fluctuations from the sun. Latitude corrections are also necessary to account for the different inclinations of the magnetic field lines (Blakely 1996).

Magnetics has been extensively used for oil and gas exploration to detect faults and igneous intrusions, metallic mineral exploration (Haldrar 2018), and archeological exploration to detect buried structures (Bevan and Smekalova 2013). Magnetostratigraphy is a term used to describe how magnetic data provide chronology in strata independent of fossil content by correlating magnetic reversals of sediments with known temporal pole orientations (Reynolds 2002). Magnetostratigraphy has been used to record a complete reversal in the magnetic field of Miocene lava flows at Steens Mountain in southeastern Oregon (Mankinen et al. 1987). Pluhar et al. (2006) used Cold Creek bar sediments in the Pasco Basin (Washington State, USA) to determine three glacial maxima during the early Pleistocene, providing a more complete record on this time period.

Most sedimentary rocks contain negligible amounts of magnetic material, while igneous and metamorphic rocks can contain appreciable amounts. At the Hanford Site, basalt has a large magnetic signature and can be used to distinguish the EM response as originating from basalt or sediments and overburden. In addition, anthropogenic iron and steel drums have a high magnetic susceptibility and represent strong targets for this method.

4.0 Previous Geophysical Surveys Done to Identify Preferential Flow Pathways at Hanford

Several geophysical surveys have been executed in both the unsaturated and saturated zones at Hanford with the goals of characterizing subsurface properties or locating contaminants (e.g., Geomatrix Consultants Inc. 2005; Last and Horton 2000; Murray and Last 2005; Strickland et al. 2018). Since this work is focused on identification of stratigraphic features, and in particular paleochannels, this report is limited to geophysical investigations performed for this purpose. Large-scale field campaigns (on the order of kilometers) have used EM and seismic methods, and ERT has been used to corroborate the findings from these campaigns. Therefore, the subsections below focus on these large-scale applications using EM, seismic methods, and ERT both independently and in conjunction with other methods. A summary of the studies performed to investigate paleochannels at the Hanford site is presented in Table 4.1.

4.1 Electromagnetics and Integration Investigations

Most of the land-based field work using EM methods at Hanford has been for detection and mapping of underground pipelines, utilities, buried debris, and other structures that are primarily metallic or conductive materials (Last and Horton 2000). EM measurements have also supplemented magnetic gradiometer data to better locate shallow underground metallic objects (Rucker et al. 2007; Myers et al. 2009). Land-based TEM has also been used more recently to detect pipeline leakages. For example, Fink et al. (2010) found that high-conductivity zones from ERT were coincident with those detected from ground-based TEM to locate leakages. These investigations, while promising, were shallow in scope, imaging in the top 20 m.

In 2008 within the 200-PO-1 groundwater operable unit (OU) of the 600 Area, two airborne EM (TEM and FEM) datasets and magnetic surveys were collected to map lithological changes in the upper layers (top 50 to 150 m), detect possible paleochannels, and locate structural breaks. Magnetic surveys were conducted in parallel and were used to decipher signatures from the basement basalt bedrock and features within sediments and overburden. Power lines and cultural interference were a major concern in these datasets. Paleochannels were assumed to be more resistive, channel-like features infilled with coarser-grained deposits (CHPRC 2010b); however, EM is most sensitive to high-conductivity zones. This made identifying laterally continuous resistive zones challenging.

Apparent resistivity models were calculated for both surveys, although it is unclear if the same method was used to produce these models. The TEM reports used a simple plate in free space model (Dyck and West 1984), while the FEM survey reports used a pseudo-layer half-space model (Fraser 1978), which consists of a resistive layer overlying a conductive half-space. The apparent resistivity models output an apparent depth, which was corrected for each section to the true topographic surface elevation. For these topographically corrected models, apparent resistivity-depth (or the so-called differential resistivity-depth as described by Huang and Fraser 1996) slices were generated at 10-m intervals. Further details of the surveys performed are as follows:

1. HeliGEMTEM survey (Fluor Hanford Inc. 2008a): A total of 55 north-south lines were collected with a nominal spacing of 400 m. Line lengths varied from 7 to 21 km and the receiver was flown at 47 m above the ground at survey speed. Using a multi-coil system (x, y, and z), 20 data-time windows were collected starting at 0.067 ms and ending at 16.667 ms.

A database of 60 levels of apparent resistivities ranging from 0 to 590 m below the surface at 10-m intervals was prepared. The effective depth of penetration is reported as 250 m. Due to the broad footprint of the HeliGEOTEM, changes in resistivity every 10 m were gradual; therefore, three averaged resistivity depth slices were prepared to present shallow (40 m: averaged from 20, 40, and 60 m), middle (100 m: averaged from 80, 100, and 120 m), and deep (160 m: averaged from 140, 160, and 180 m) layers.

Generally, the lower resistivity in these profiles was correlated with the Ringold and Ringold Lower Mud units. Zones of lower resistivity are not continuous and this was interpreted as a geologic control, either the location of a fault or a paleochannel.

2. RESOLVE FEM survey (Fluor Hanford Inc. 2008b): This survey had a smaller aerial footprint, and imaged shallower than the HeliGEOTEM survey, resulting in higher resolution output. Flight lines were flown suspending the instrument at 30 m above land surface in an azimuthal direction of 2 degrees with line separations of 100 m and 200 m. A multi-coil coaxial/coplanar source energizes conductors in x, y, and z directions. The RESOLVE system contains five coplanar (horizontal) oriented coils with frequencies of 400, 1800, 3300, 8200, 40,000, and 140,000 Hz. There was also one coaxial (vertical) coil with a frequency of 3300 Hz. The system produces an in-phase and quadrature measurement from each transmitter-receiver coil pair. The effective depth of penetration is reported as 60 m.

To interpret the recorded FEM data, differential resistivity-depth slices were produced from 2 to 52 m at 10-m intervals using a pseudo-layer half-space approximation of the subsurface (Fraser 1978). However, this approximation to a 3D earth has limitations and might not produce the true resistivity distribution. Therefore, to accurately interpret the recorded EM data, a full 3D inversion of the recorded EM data is required.

A comparison of the results is shown in Figure 4.1, as resistivity depth slices at 50 m, representing a shallow image from the HeliGEOTEM and a deep image from the RESOLVE survey. The color scale is shown for comparison only (Figure 10, Fugro Airborne Surveys 2010). Although the RESOLVE survey is more detailed, the images generally show agreement in the location of resistive features interpreted as paleochannels or preferential flow pathways. However, the depths reported for the slices are not true depths; rather, they represent the location where the strongest EM signal is being generated as the signal decays within the subsurface (CHPRC 2010b). This generalizes the comparison shown in Figure 4.1 and introduces ambiguity in interpreting these (depth-located) results.

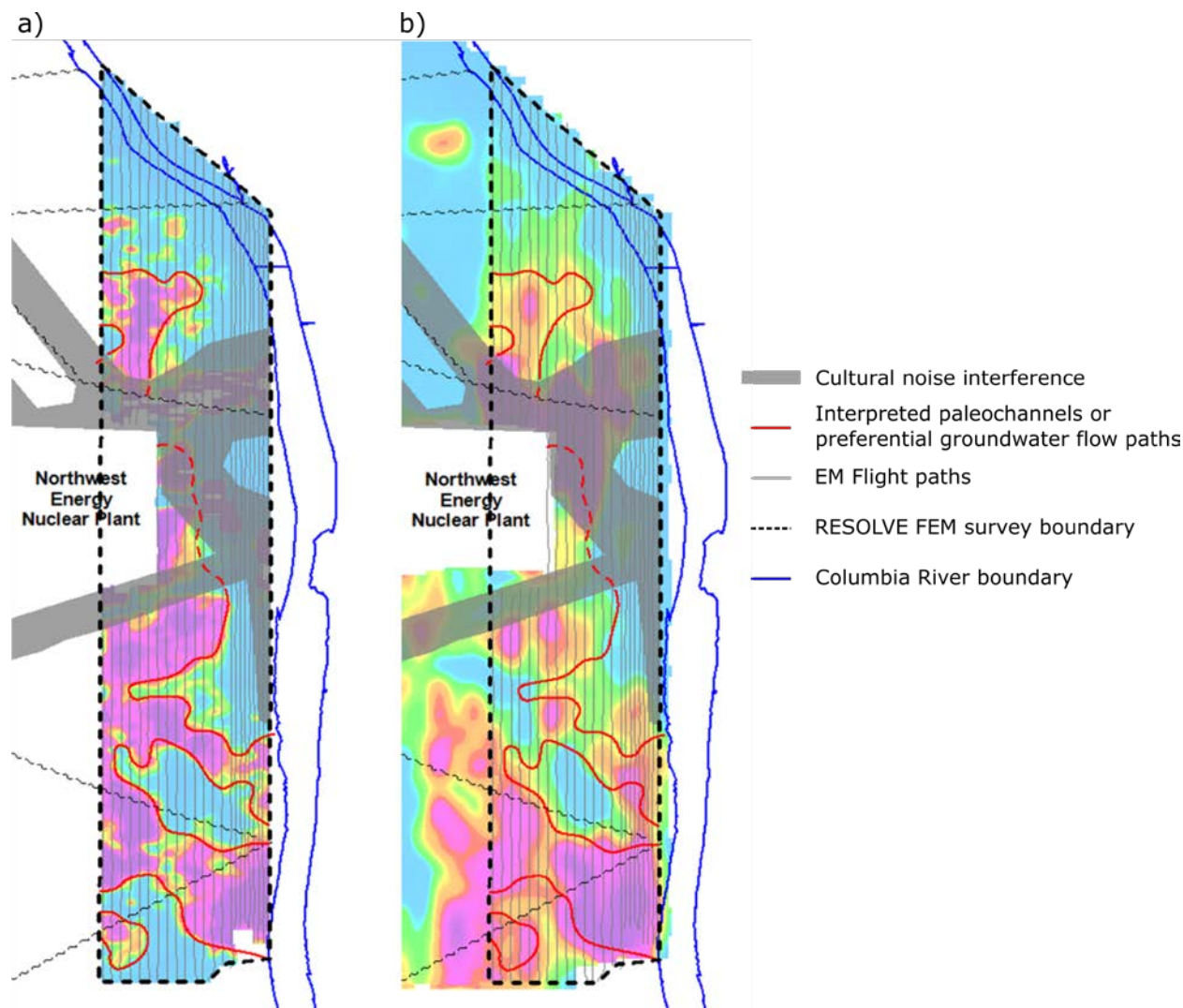


Figure 4.1. Comparison of 50-m resistivity depth slice of the RESOLVE FEM survey in a) and the HeliGEOTEM in b) (from Figure 10, Fugro Airborne Surveys 2010).

Ground-based FEM and 2D ERT techniques were used to compare and contrast to the CHPRC (2010a) analyses. An EM survey was performed using a Geonics EM-34 with three frequencies (400, 1600, and 6400 Hz) to compare with airborne EM data. The manufacturer reports horizontal dipoles have an effective depth ranging from 6.5 to 26 m; the effective depth of vertical dipoles ranges from 1.5 to 32 m. One-dimensional layered earth models using three layers were used to construct a 2D cross-section.

A roll-along 2D ERT survey was used by overlapping 84 electrodes spaced at 6 m for a total profile length of 5538 m. A 2D constrained inversion using the commercially available software RES2DInv accounted for the water table, providing a sharp contrast at this depth within the modeling. An investigation depth of 80 to 120 m was reported for the survey type used and electrode spacing.

The ground-based FEM and 2D ERT (Figure 4.2) identified changes in resistivity and likely geologic contacts (Hanford-Ringold, intra-Ringold). The Hanford-Ringold contact was found as a high-to-low change in resistivity magnitude. Both methods imaged the transition from unsaturated to saturated conditions.

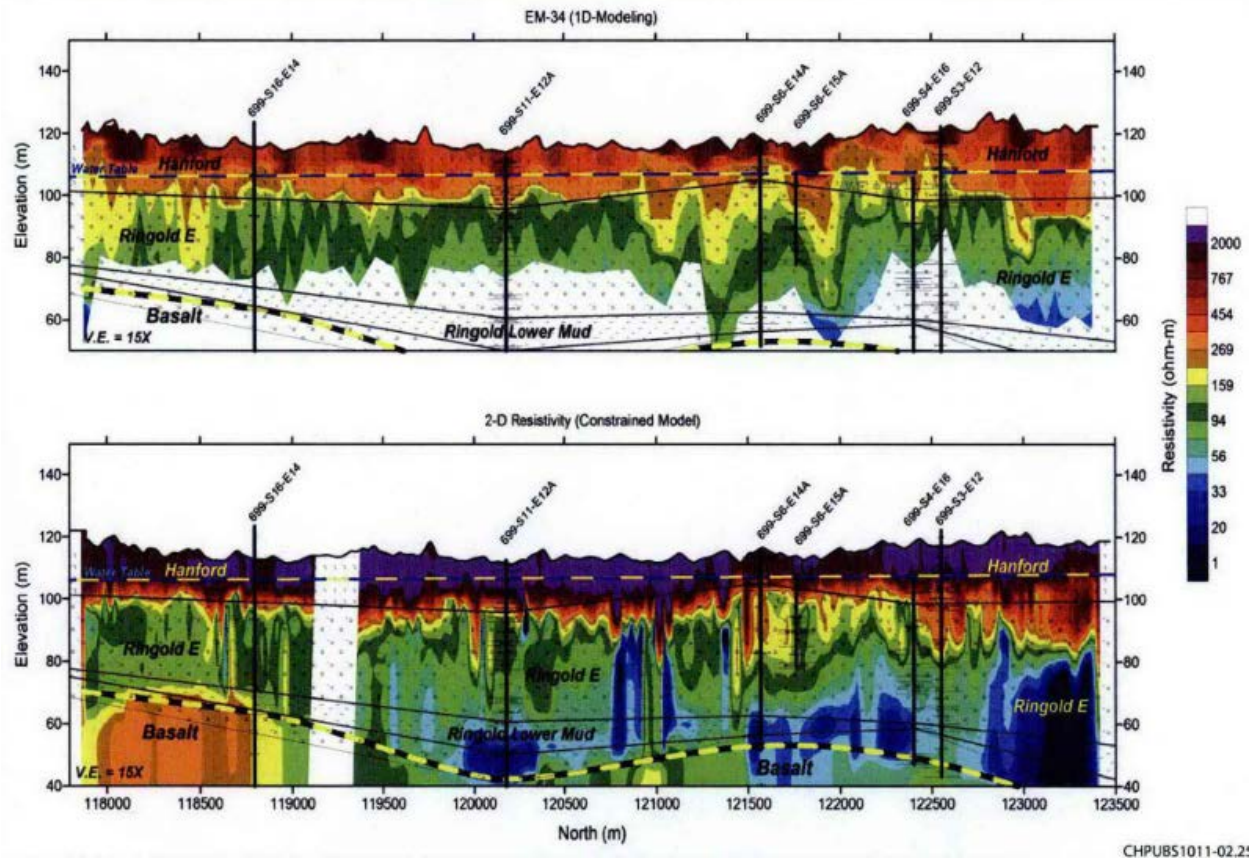


Figure 4.2. Ground-based EM-34 model (top) and 2D resistivity model (bottom) (Figure 4-1, CHPRC 2010b). The dashed yellow-blue line in both images depicts the water table boundary.

Comparing ground-based methods with the HeliGEO TEM and RESOLVE airborne surveys, the following was found (CHPRC 2010a):

- The depth of the Hanford-Ringold contact was identified as shallower for the ground-based FEM system. The 2D ERT identified the Hanford-Ringold contact as a change from higher resistivity (250 ohm-m) to lower resistivity (< 150 ohm-m).
- The ground-based FEM system mapped the near surface, highly resistive vadose-zone sediments better. The authors concluded that the near-surface vadose zone sediments were not correctly imaged in the RESOLVE FEM survey, due to the very high resistivities (>1500 ohm-m), which was below the sensitivity range of the RESOLVE instrument.
- The HeliGEO TEM has the lowest resolution and inverse modeling was recommended to compare with the underlying geology.

4.2 Seismic and Integrative Investigations

Seismic methods were employed north of the 200 East Area within Gable Gap to refine the groundwater flow model and identify when northerly flow conditions through the gap and easterly flow conditions south of the gap occurred. The objective of these surveys was to map the top of basalt layer and possible erosional channels within the suprabasalt sediments that dictate groundwater flow direction.

In 2009, a high-resolution seismic landstreamer / gimbaled survey (CHPRC 2009) was deployed, consisting of eight profiles with total length of 11 km. The data were evaluated for the depth and geometry of reflectors. Processing included pre- and post-stack time migrations, and pre-stack depth migration, constrained by borehole check-shot surveys to known geologic units. Geologic velocity functions were used to convert travel time to elevation for depth migration. The top of basalt was a recognizable seismic reflection on the raw data. Profiles revealed a highly variable depth profile of the top of the basalt. Erosional channels were inferred as depressions in 3D views (Figure 4.3). The smallest channel this survey is capable of detecting reliably is reported as 10 m thick and 20 m in width.

In 2011, a re-evaluation of previously collected high-resolution seismic datasets was performed (CHPRC 2011) to map the top of basalt and suprabasalt contacts. The datasets included the 2009 landstreamer data, data collected in FY 2008 within the 200 East Area, and data collected during FY 1979 and FY 1980 as part of the Basalt Waste Isolation Project. Check shots (i.e., seismic data obtained within a single borehole using a surface source location to a known depth) were the primary method used to correlate seismic data with the geology. These surveys demonstrated seismic methods were capable of resolving interfaces within the vadose zone sediments of supra-basalt sediments, including Hanford subunits and the Cold Creek and Ringold units.

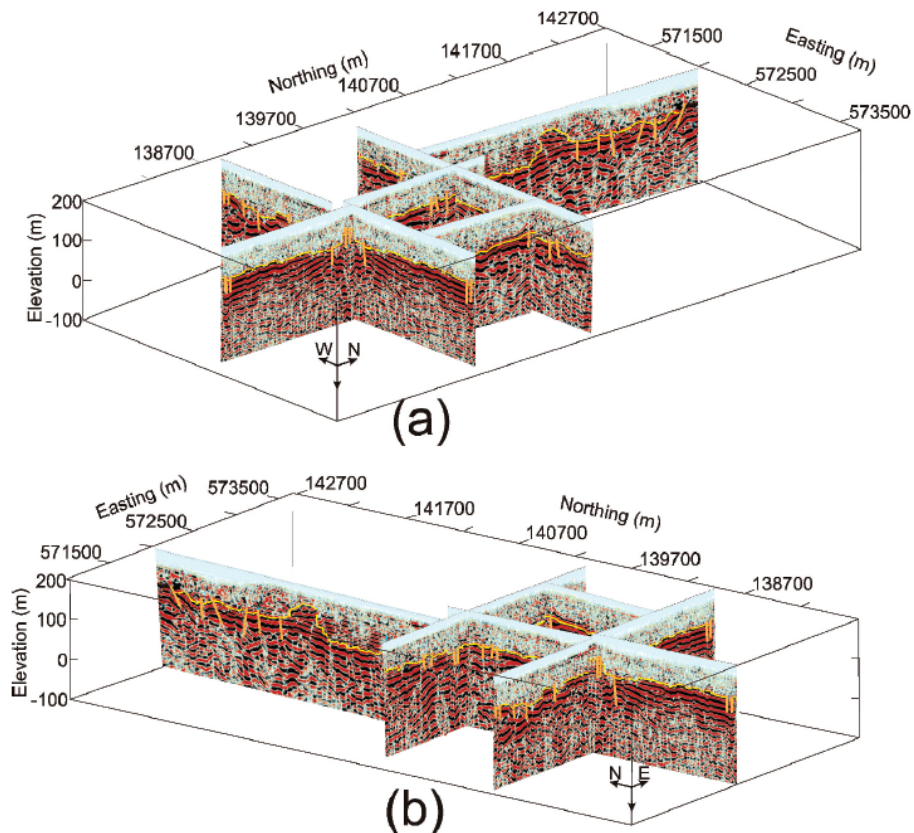


Figure 4.3. Pre-stack depth-migrated seismic results from a landstreamer survey northwest of 200 East Area interpreting the basalt boundary and potential locations of faults (orange) (Figure 8 from Hyde et al. 2011).

Another integrated approach at the Liquid Effluent Retention Facility (LERF) used seismic refraction, vertical seismic check shots, 2D ERT, and TEM 1D soundings to provide supporting information for locating a future groundwater monitoring well (CHPRC 2012). The surveys were focused on imaging the

basalt layer, water table boundary, and potential groundwater migration pathways, integrating results from field studies performed from 2008-2011. Seismic data were used primarily to identify the depth to the basalt layer and the character of the basalt (i.e., weathered, fractured). The 2D ERT and TEM 1D soundings were used to identify additional subsurface contrasts in resistivity and the location of the water table. Interpretations were made from each geophysical method and the known geology and then cross-correlated with each other for a final interpretation. Boundaries for the water table, upper and lower Hanford horizons, and the Hanford-basalt contact were identified as shown in Figure 4.4.

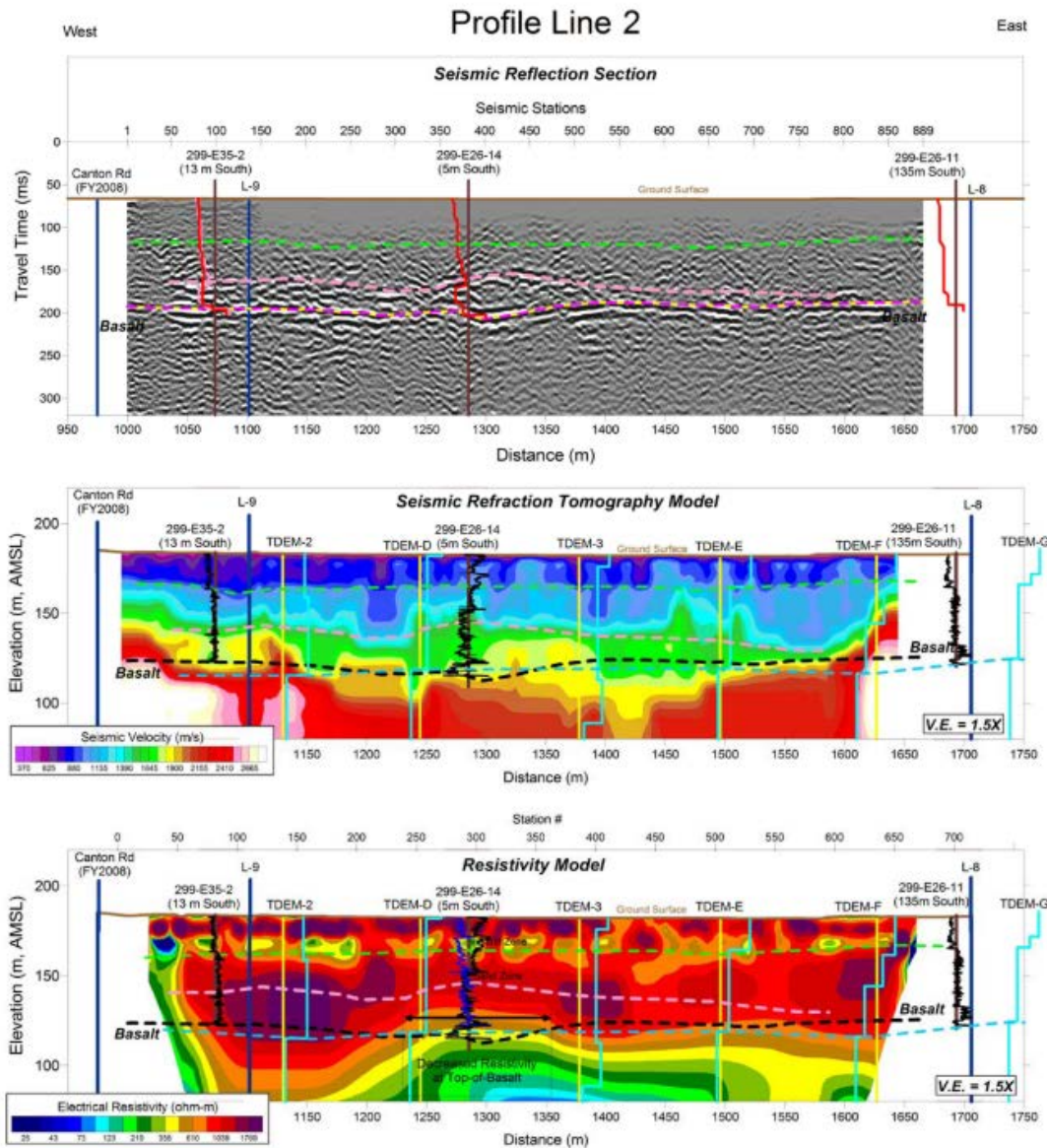


Figure 4.4. Profile Line 2 was collected along a west-to-east profile north of the LERF basins. The interpreted basalt boundary is shown as dashed dark pink (top) and black (middle, bottom) lines. The Hanford formation is separated into two horizons, an upper (dashed green line) and lower (dashed pink line) (Figure 5, CHPRC 2012).

Deep (> 500 ft) shear velocity profiling using SASW was performed in the 200 East Area (Lin 2007) and across the Hanford Site (Stokoe et al. 2014). While the purposes were to assess seismic class and

probabilistic rating in the event of an earthquake, the 1D profiles may also be used to map lithologic boundaries.

4.3 Electrical Resistivity Tomography

In the 300 Area, uranium transport (originating from the discharge of waste fluids from two infiltration ponds and a disposal trench) is dependent on river and groundwater chemistry and fluctuations in the Columbia River stage. The contact between the Hanford formation and the Ringold Formation (the H-R contact) represents a boundary that limits the vertical migration of contaminants. Hanford formation sediment incised into the Ringold Formation enhances the interaction between surface water and groundwater. Therefore, identification of the paleochannels relative to river stage is key to identifying predominant uranium transport pathways.

Slater et al. (2010) conducted continuous waterborne electrical imaging in conjunction with fiber-optic distributed temperature sensor monitoring. They found that seasonal temperature anomalies were correlated with lithology and these were areas in the electrical imaging where the Hanford sediments were thickest and the H-C contact was deepest (Figure 4.5). They determined that these focused areas of exchange play an important role in regulating surface water-groundwater exchange at the 300 Area.

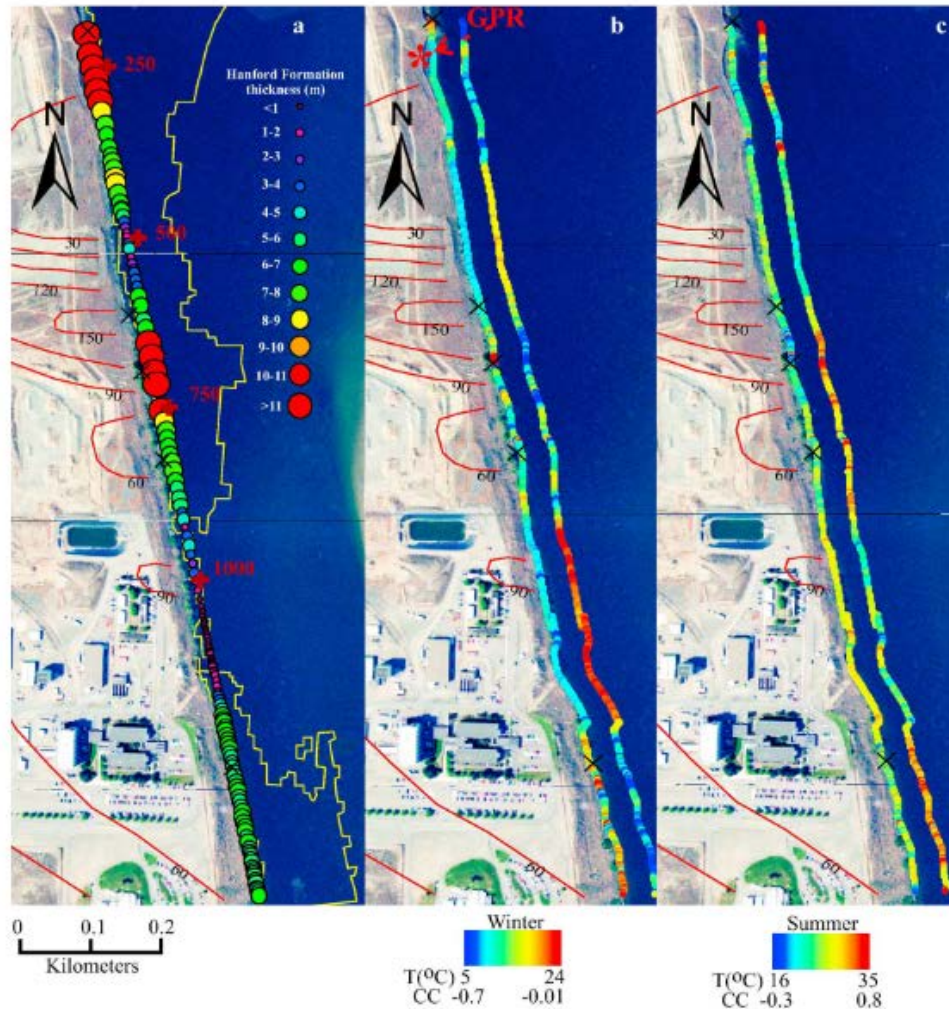


Figure 4.5. a) Hanford formation thickness estimated from waterborne electrical imaging. Low stage temperature measurements collected on b) 3/31/2009 and c) 8/2/2009. Red contours represent uranium concentrations (Slater et al. 2010, Figure 8).

Subsequent time-lapse ERT studies were performed to better define the surface water-groundwater exchange by locating paleochannels along the river corridor. The contrast in specific conductance between the Columbia River water (0.015-0.020 S/m) and the groundwater (0.040-0.045 S/m) enables ERT to detect in 4D when sediments are saturated with river or groundwater (Johnson et al. 2012). A near-shore 3D array was positioned parallel to the riverbank and consisted of four lines of 30 electrodes, spaced at 5 m along each line (total of 120 electrodes). This location straddled the region of focused exchanged identified by Slater et al. (2010). A time-series and time-frequency analysis of the 3D data (Johnson et al. 2012) focused on the dynamics of this exchange in relation to upstream daily dam operations. Segments in time-frequency space identified when surface-water groundwater interactions were most active.

Inland dynamics of the surface water-groundwater exchange in the 300 Area was studied by Wallin et al. (2013) using 2D surface ERT. The array consisted of using three-2D ERT lines, with two lines containing 60 electrodes spaced at 4 m along the line and one line containing 64 electrodes, spaced at 3 m along the line. Groundwater depths were continuously monitored. The time-lapse 2D ERT analysis consisted of

incorporating a fluctuating water table boundary in a 2D ERT inversion analysis, enabling imaging of both preferential and low permeability zones that created fast flow paths for river water to flow in and out of the aquifer.

Following the work of Wallin et al. (2013), a larger electrode array was installed in the 300 Area to capture larger scale spatiotemporal dynamics (Johnson et al. 2015) (Figure 4.6). The array consisted of 11 electrode lines spaced 25 m apart, with each line having 32 electrodes at 10 m spacing, for a total of 352 electrodes. Critical to the interpretation was the incorporation of water table fluctuations and allowing the numerical modeling to only choose models where there was a physically realistic increase in electrical conductivity. The imaging delineated a series of paleochannels that were consistent with the hydrogeological structure inferred from boreholes.

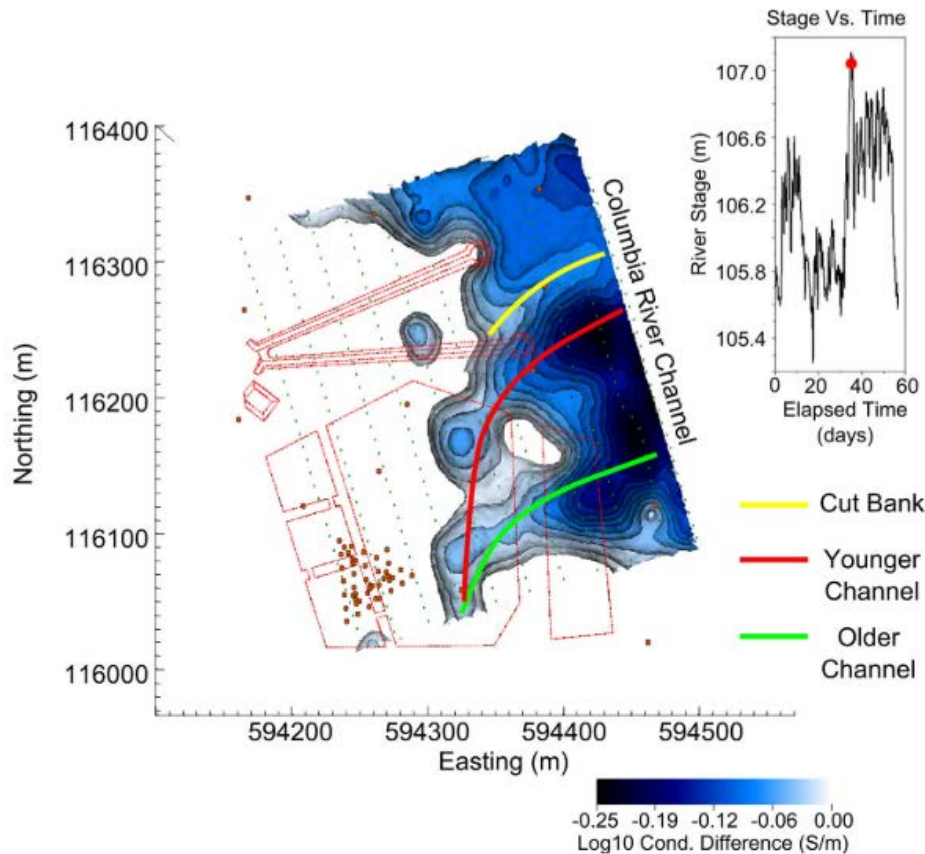


Figure 4.6. Plan view ERT image of high stage river water intrusion within the saturated zone. The colored isosurfaces contour the negative changes in EC with respect to baseline conditions, indicating the presence of river water. River water intrusion flows preferentially through two features interpreted as high permeability paleochannels (Johnson et al. 2015, Figure 11b).

4.4 Ground Penetrating Radar

GPR has not been used specifically to identify paleochannels. However, case studies at the Hanford Site report stratigraphic features could be resolved if data were collected at a resolution-appropriate frequency. The literature reviewed suggests that the lowest frequency allowed to be used on the Hanford Site was 100 MHz (Rucker et al. 2007). Interpretation depths for this frequency are approximately 10 to 12 m, which is not deep enough to resolve paleochannel features at depth.

GPR has been used to reconstruct depositional environments and determine the nature of sedimentary processes because primary reflections usually parallel primary depositional structure (Neal 2004). GPR has been used to identify stratigraphy in sand dunes (Carling et al. 2016; Harari 1996), determine sediment thickness in coves around a lake (Banks and Johnson 2011), and identify major sedimentary structures in a deltaic sedimentary environment (Jol and Smith 1991). The depths of investigation were less than 50 m; however, lower frequency antennae could potentially resolve deeper features in the subsurface. For example, Smith and Jol (1995) found that the maximum probable penetration depths in Quaternary sediments was 52 m (gravel facies) for a 25-MHz antennae and estimated to be 66 m for 12.5-MHz antennae.

At Hanford, GPR has been used to locate metal objects that could interfere with an electrical resistivity survey (Rucker et al. 2007; Myers et al. 2009). GPR is commonly used in this capacity. Other surveys have identified subsurface disturbances (Bergstrom et al. 1993), located clastic dykes, and identified the spatial variability in water content (Knight et al. 2003, 2007).

Table 4.1. Previous geophysical methods used to investigate paleochannels at Hanford.

Site/Location	Date(s) of Survey	Geophysical Technology	Survey Objectives	Reference document	Author(s)	Publication Date
200 Area						
North 200 East Area	Late May-Early June 2009	Seismic Reflection / Vertical profile (check shot)	Seismic landstreamer survey to map depth to the basalt layer and preferential flow paths associated with the basalt surface (referenced in SGW-48478)	SGW-43746	Ch2MHill	Nov-09
North 200 East Area / Gable Gap	FY2010, FY2009, FY2008, FY1979, FY1980	Seismic Reflection / Vertical profile (check shot)	Interpretation and integration of previously acquired seismic data in the Gable Gap using available geologic data to refine the conceptual site model	SGW-48478	Ch2MHill	Apr-11
North 200 East Area near the Liquid Effluent Retention Facility (LERF)	FY2008, FY2011	TEM, 2D ERT Seismic Reflection / Vertical profile (check shot)	Determine the basalt surface and the nature of the sediment-basalt interface beneath the Liquid Effluent Retention Facility to locate RCRA compliance wells	SGW-52467 SGW-52161	Ch2MHill Golder Associates	2012
East of the 200 East Area	Sept 8-12,2004	Seismic surface SASW	Deep (> 500 ft) shear velocity profiling for characterization of soil deposits and rock formations for seismic hazard rating	Lin 2007	Y.Lin	2007
300 Area						
Adjacent to Columbia River	2008	Waterborne ERT	Characterization of surface-water ground-water exchange		Slater	2010
Adjacent to Columbia River	2010	3D ERT	Characterization of surface-water ground-water exchange		Johnson	2012
Adjacent to Columbia River	2011	2D ERT	Characterization of surface-water ground-water exchange		Wallin	2013
Adjacent to Columbia River	2013	3D ERT	Characterization of surface-water ground-water exchange		Johnson	2014
600 Area						
600 Area (200-PO-1 GOU)	6/19-6/20/2008	TEM, Magnetics	Map layers to 150 m depth, detect paleochannels, locate structural breaks	08027	Fluor Handford Inc.	Sep-08
600 Area (200-PO-1 GOU)	6/29-7/1/2008	FEM, Magnetics	Map upper layers to 50 m depth, detect paleochannels, locate structural breaks	08027R	Fluor Handford Inc.	Sep-08
600 Area (200-PO-1 GOU)	6/19-6/20/2008 6/29-7/1/2008	TEM/FEM, Magnetics	Evaluation of Phase I Geophysics Technologies in the 200-PO-1 Operable Unit	SGW-38941	Cummins	Sep-08
600 Area (200-PO-1 GOU)	6/19-6/20/2008 6/29-7/1/2008	TEM/FEM, Magnetics	Interpretation of Airborne Electromagnetic and Magnetic Data in the 600 Area	SGW-47839	Ch2MHill	Sep-10
600 Area (North of 300 Area)	2010	FEM, 2D ERT	Testing Ground Based Geophysical Techniques To Refine Electromagnetic Surveys North Of The 300 Area, Hanford, Washington	SGW-47996, Hyde et al., 2009	Ch2MHill, Hyde et al., 2009	Nov-09 Dec-10
Site-wide						
100 B/C, 200 areas, 200-PO-1 GOU, Gable Gap	FY2007, FY2008, FY2009, FY2010	Seismic vertical profile (check shot)	Measurement of Seismic Velocities in 29 Wells at the Hanford Site Seismic Velocities in 29 Wells at the Hanford Site (referenced in SGW-48478)	SGW-47535	Ch2MHill	2010
Site-wide	2013	Seismic Surface SASW	Deep (> 500 ft) shear velocity profiles at each test site	DCN:GR14-1	Stokoe et al., 2014	2014

4.5 Conclusions / Recommendations of Previous Work

At the Hanford Site, large-scale EM, seismic, and ERT surveys have been designed and executed at scales relevant to delineating large-scale paleochannels. Initial surveys were further verified by performing multiple field campaigns, applying more than one geophysical method, and looking at non-geophysical datasets, such as borehole geologic information.

Discontinuities (i.e., facies changes) have been reported in several studies within the Ringold Formation. The airborne EM (HeliGEOTEM and RESOLVE) and ground-based EM-34 and 2D ERT surveys all reported a discontinuity in the low-resistivity sediments, which were assumed to be coarser-grained, Hanford sediments incised into the finer-grained sediments of the Ringold Lower Mud. This boundary is located near the water table and appears to channel groundwater flow. Therefore, geophysical data from surrounding units can also contribute to stratigraphic identification.

The ERT analyses performed in the 300 Area Hanford studies to identify surface-water groundwater interaction (Slater et al. 2010; Wallin et al. 2013; Johnson et al. 2012, 2015) clearly demonstrate time-lapse ERT as a viable option to image transient processes controlled by stratigraphy in the top 50 m. Static surface ERT has also shown promise to image stratigraphy (Figure 4.2, Figure 4.4), although the contrast in resistivity between the contacts can be small (CHPRC 2010b), underscoring the need to supplement its use with other field data (e.g., borehole sampling, other geophysical surveys). Static imaging could potentially be used to locate boreholes for further ground-truthing. A joint inversion of ERT with other field datasets better constrain the solution (Johnson et al. 2017).

Based on the review of geophysical surveys at Hanford, the following actions are recommended:

- Re-evaluate existing EM survey data where paleochannels were identified using 2D and/or 3D inverse modeling.

Previous airborne EM surveys are of high quality and were collected over multiple frequencies and time windows to have a sensitivity from the very shallow to at least 150 m depth. However, these data have not been inverted to estimate true depths. The depths reported from the EM surveys represented the location where the strongest EM signal were generated as the signal decayed within the subsurface. True depths can only be determined using 2D or 3D inverse modeling, where the data fit the response for a given model of the same dimension. A 2D and/or 3D EM inversion of the RESOLVE (Fluor Hanford Inc. 2008b) and/or HeliGEOTEM (Fluor Hanford Inc. 2008a) data can be performed to identify the depths associated with high- and low-conductivity zones.

Inversions of a shallower depth of investigation EM-34 survey (CHPRC 2010b) can be compared to the airborne inversions. This EM-34 dataset was never inverted; rather, the 1D-subjective goodness-of-fit analysis matched the observed response to a theoretical response for a given number of layers. To create 2D geoelectrical sections, each 1D layer approximation was interpolated to create 2D geoelectrical sections. Inverting these data could further verify the stratigraphic interpretation of data from the airborne surveys.

- Re-evaluate existing seismic data where basalt and suprabasalt units were identified using inverse modeling.

The previous seismic surveys performed at Hanford were evaluated for reflector locations and geologic contacts were based on borehole check-shot information. Beyond reflection information, the amplitude of the returned wave at an interface is controlled by the contrast in impedance, which is dependent on the bulk density and sonic velocity within the subsurface (Barclay et al. 2008). Seismic reflectivity inversion extracts additional information from seismic data and “facilitates the

interpretation of meaningful geological and petrophysical boundaries in the surface” (Veeken and Silva 2004). The distribution of density and velocity can further inform the conceptual model for the major stratigraphic units.

- Use low-frequency GPR to image stratigraphy in the top 100 m. Low-frequency antennae have not previously been permitted at Hanford. However, a small-scale proof-of-principle effort can be executed to determine the potential feasibility of using GPR for stratigraphic identification.
- Use modeling to determine if ERT can be used to characterize paleochannels at other locations across the Hanford Site, which can also include re-evaluating previously collected datasets. This is a cost-effective approach since the feasibility is assessed before a survey is executed in the field.

The final action recommended above has been executed and documented in this report. Results of the potential to use ERT for stratigraphic identification are presented in Section 5.0. A re-evaluation of EM data is conducted and is documented in Jaysaval et al., *draft*¹.

¹ Jaysaval P, JL Robinson, TC Johnson. 2020. “Stratigraphic Identification with Airborne Electromagnetic at the Hanford Site, Washington.” *To be submitted*.

5.0 Pre-field Feasibility Evaluation of Electrical Resistivity Tomography

The potential for an ERT survey to identify an electrically conductive paleochannel between the 200 West and 200 East Areas was evaluated by using a groundwater flow and transport model to provide information on porosity and saturation and converting this information into bulk electrical conductivities. ERT modeling was then used to simulate transfer resistance data and to image the subsurface. Results were then compared to the groundwater model (Johnson et al. 2017; Robinson et al. 2019; Vanderborght et al. 2005). The Hanford South GFM (CHPRC 2016) for the area between 200 East and West is shown in Figure 5.1. The Hanford formation has been removed from this figure to highlight incisions of lower elevation into the lower units that may be representative of zones of high transmissivity.

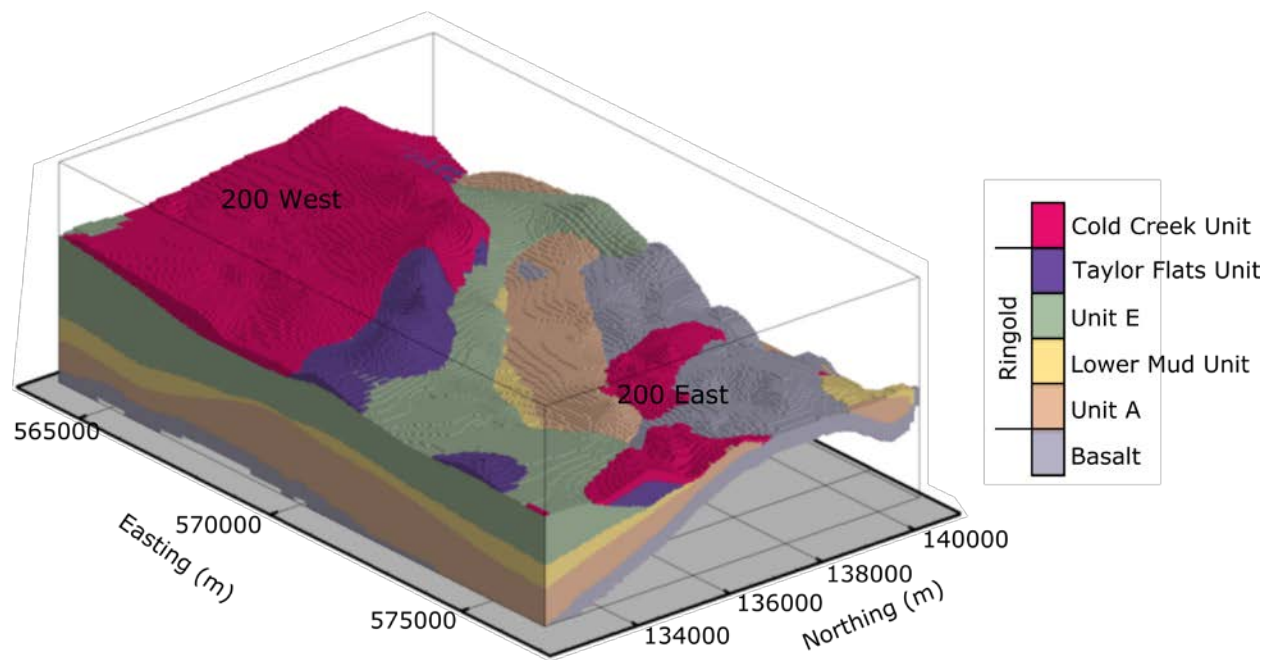


Figure 5.1. The Hanford South geologic framework model (CHPRC 2016) between 200 East and West on the Central Plateau. The Hanford formation has been removed to demonstrate the general shape of a paleochannel between 200 East and West as inferred by areas of lower elevation.

Using simulations to evaluate the likely performance of a field ERT campaign has the following benefits:

- Realistic assessment of the ability of ERT to provide useful information on subsurface structures under the given field conditions
- Optimization of ERT design such as electrode spacing and measurement sequence and configuration
- Identification of potential limitations and constraints

In this report, the initial state is referred to as the background, which represents a static, characterization ERT image. This background state is used to delineate lithologic contrasts between the paleochannel and surrounding units. The electrical conductivity contrast below the water table is enhanced by injecting a conductive tracer, and time-lapse imaging is performed of tracer transport relative to background. Subtracting the background ERT image from the time-lapse removes the static effects of lithology and

reveals only what has changed over time, namely the change in bulk conductivity caused by the migration of the tracer. This method is commonly referred to as time-lapse ERT difference imaging and enables the imaging of conductive, ionic tracers travelling through preferential flow pathways.

The pre-field test feasibility evaluation was conducted in steps to identify a potential transmissive paleochannel ~70 m below the surface in the unconfined aquifer using simulated surface ERT arrays. The first analysis focused on a single conceptualization of hydrologic and petrophysical parameters with a single tracer volume and concentration. The second phase explored uncertainty in parameter estimates and tracer scenarios. The results represent a pre-field test evaluation of the potential effectiveness of a large-scale ERT field deployment for imaging the hydrostratigraphy and tracer transport between 200 East and West.

5.1 Site Description

The simulation domain includes the inferred spatial extents of the paleochannel. Phase 1 used the Hanford South GFM (CHPRC 2016) (Figure 5.2). The stratigraphic units included in this model are shown in Figure 5.1. Phase 2 used the updated Central Plateau Vadose Zone GFM (CHPRC 2019, 2018a,b) (Figure 5.3). In this framework, the Hanford formation has two subunits, H1 and H2, that are present locally. The Cold Creek Unit has two subunits, CCuC and CCuZ.

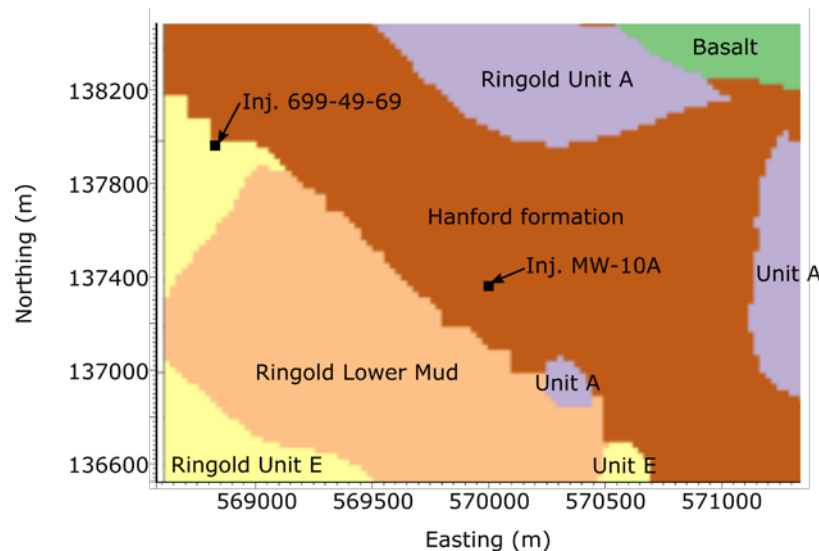


Figure 5.2. Hanford South geologic framework model (CHPRC 2016) at an elevation of 120 m in the saturated zone. The time-lapse ERT simulations focus on depths at or below this elevation.

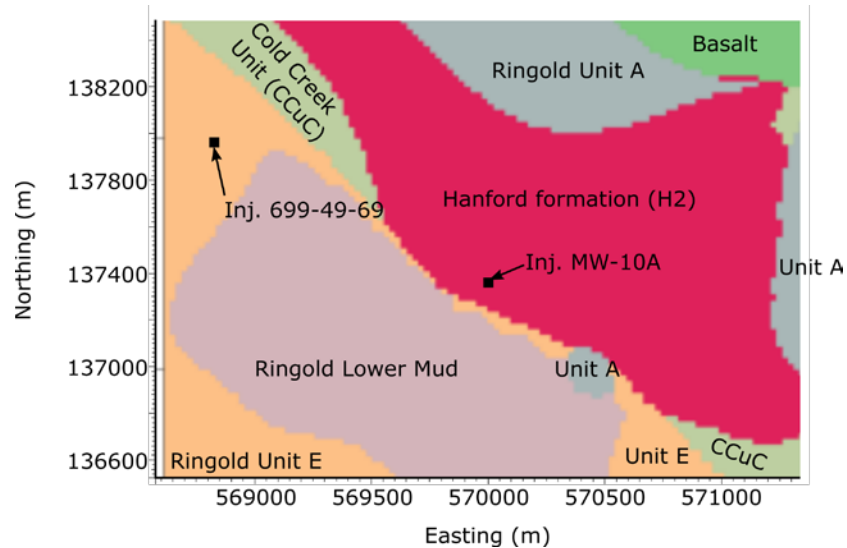


Figure 5.3. Central Plateau Geoframework (CHPRC 2019, 2018a,b) at an elevation of 120 m in the saturated zone. This figure represents an updated geologic framework model from the image shown in Figure 5.2.

There are two candidate tracer injection wells near the inferred paleochannel in the GFM (Figure 5.2 and Figure 5.3). The first candidate injection well is an existing well (699-49-69) with a screened interval at the water table. This well is currently in use as an injection well for the 200-ZP-1 OU carbon tetrachloride pump-and-treat system. The second candidate injection well has been identified as a potential monitoring well for fiscal year 2021 (designation MW-10A). The MW-10A location is presumed to be within the paleochannel between the 200 East and West Areas. The planned midpoint screened interval elevation is 106 m, which is within the Ringold Unit A (refer to Figure 5.1). While this planned screened elevation is below the paleochannel according to the GFM, the screened interval is assumed to be completed within the Hanford sediments to represent the paleochannel.

Domain extents are 1400 m in the northing direction and 2300 m in the easting direction, representing an area of 3.22 km² (Figure 5.4). Ground surface elevations range from 176.70 to 228.80 m and generally slope downward to the northeast. The water table surface generally slopes eastward from 200 West to 200 East Area, with water table elevations ranging from 129.73 to 121.95 m.

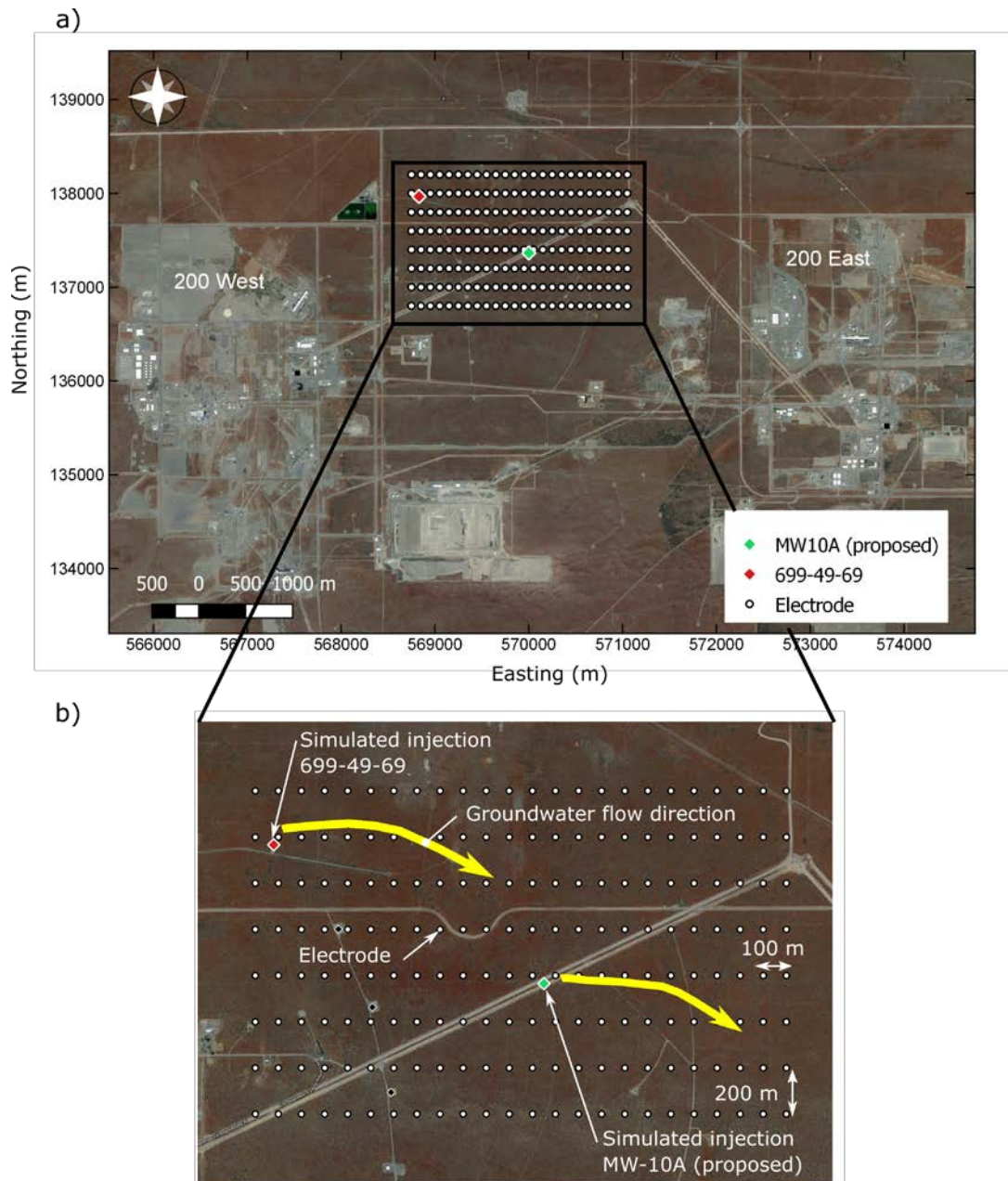


Figure 5.4. a) Proposed electrode placement and injection well locations used in the geophysical simulations; and b) magnified site view with groundwater flow directions with yellow arrows.

5.2 Simulation Description

Simulations of groundwater flow and solute transport were performed using the water operational mode of eSTOMP (Fang et al. 2015), a parallel version of STOMP (White and Oostrom 2006). ERT imaging simulations were conducted using E4D (<https://e4d-userguide.pnnl.gov/>, Johnson 2014; Johnson et al. 2010), an open source 3D modeling and inversion code designed to run on distributed memory parallel computing systems.

The eSTOMP simulator uses a 3D structured grid with orthogonal, hexahedral grid blocks, while E4D discretizes the model space with a 3D unstructured tetrahedral mesh. Therefore, eSTOMP output was interpolated to the E4D mesh. The mesh interpolation scheme of Johnson et al. (2017) was adapted so that each E4D element is divided into sub-elements and a tri-linear interpolation is used to determine the weighting from eSTOMP output. This integrated approach minimizes discretization differences.

5.2.1 Flow and Transport

The tops of major hydrostratigraphic units at the site were defined from borehole geologic and geophysical data (Hammond and Lupton 2015). Surfaces defining these tops were used to define the spatial distribution of lithological types for the eSTOMP-based 3D numerical flow and transport model. The 3D model represents a 4-km by 4-km area in between the 200 East and West Areas. The vertical extent of the model covers an elevation range from 38 to 234 m, from basalt to ground surface. The model was discretized using 2.0 million grid blocks. Since the topography over the area is variable, grid blocks lying above the elevation of the ground surface are defined as inactive (non-computational). Uniform 25-m grid spacing was used in the horizontal direction and uniform 2-m grid spacing was used in the vertical direction.

For the non-reactive transport simulations, potassium bromide (KBr) was used and density effects were accounted for in eSTOMP transport. The addition of a conductive tracer can create sharp concentration boundaries with the native groundwater. To account for these sharp boundaries, a total variation diminishing transport scheme was used to ensure mass conservation with minimal numerical dispersion. The eSTOMP output parameters used for the ERT simulations were saturation, porosity, and tracer concentration.

Lateral boundaries for groundwater flow were defined using seepage face boundary conditions in which base pressures and gradients along segments of the lateral boundaries were defined by interpolating data from a database of water table elevations for a Hanford Site-wide well monitoring network. Historical water level data from 1944-2018 were used. Boundary conditions for times later than 2018 were held constant at the last values used for 2018. The upper recharge boundary conditions were defined based on a recharge map for the site (Fayer and Walters 1995). Lateral boundaries for transport were defined as outflow type boundary conditions. The upper boundary condition for transport was defined as a zero-flux condition.

Hydrologic parameters for the hydrostratigraphic units defined in the flow and transport model are shown in Table 5.1 (Rockhold et al. 2018; Budge 2017). Beginning in 2020, a tracer injection of 757 m³ (200,000 gallons) was simulated at two borehole locations: 699-49-69 and MW-10A, over a period of 7 days just below the water table. The tracer concentration used in the modeling was 60 g/L KBr.

Table 5.1. Input parameters for Phase 1 flow and transport model simulations.

HSU	Subunit	K_{sxx}/K_{syy} [m/d]	K_{szz} [m/d]	Porosity [-]	S_r [-]	α [1/cm]	n [-]	ρ_s [g/cm ³]
Hanford fm	Hf	6.14E+01	3.80E+00	0.250	0.077	0.061	2.03	2.62E+00
Cold Creek	CCu	2.00E+03	1.00E+02	0.250	0.6512	0.0092	5.942	2.71E+00
	Rtf	2.00E+00	2.00E-01	0.391	0.0725	0.021	1.374	2.72E+00
Ringold Fm	Rwie	4.36E+00	4.30E-01	0.221	0.0725	0.021	1.374	2.86E+00
	Rlm	8.00E-03	8.00E-04	0.400	0.0565	0.0197	1.419	2.71E+00
	Rwia	1.00E+00	1.00E-01	0.221	0.0562	0.0197	1.419	2.86E+00
Basalt	Ba	1.40E-05	1.40E-05	0.100	0.0725	0.021	1.374	2.71E+00

The sensitivity of ERT predictions to uncertainties in hydrologic parameters was also explored. Parameter fields used by MODFLOW and MT3DMS in the calibrated Plateau-to-River (P2R) model described by Budge (2019) were mapped to eSTOMP model grid blocks for elevations less than 140 m. Overlying grid blocks, representing vadose zone sediments, were assigned physical and hydraulic properties based on three different sets of parameters. Model 1 parameters were based on a STOMP input file developed by Intera to represent the vadose zone in the WA-1 waste management area (as used in Robinson et al, 2020). Models 2 and 3 were based on parameters representing the 216T-X and 216S_U N-x vadose zone templates, respectively, described in the vadose zone hydrogeology data package for Hanford assessments by Last et al. (2006). The parameters used to explore uncertainty are listed in Table 5.2.

Table 5.2. Input parameters for Phase 2 flow and transport model simulations.

HSU	Subunit	eSTOMP Zone No.	Parameter [units]	Model 1	Ref	Model 2	Ref	Model 3	Ref	
Hanford fm	H1 ^(a)	10	K _{sxx} [m/d]	2.26E+00	1	1.24E+01	3	2.03E+00	4	
			K _{syy} [m/d]	2.26E+00	1	1.24E+01	3	2.03E+00	4	
			K _{szz} [m/d]	2.26E-01	1	1.24E+00	3	2.03E-01	4	
			Porosity [-]	2.13E-01	1	1.54E-01	3	2.73E-01	4	
			S _r [-]	1.51E-02	1	1.52E-01	3	1.33E-01	4	
			α [1/cm]	1.41E-02	1	1.40E-02	3	8.00E-03	4	
			n [-]	1.37E+00	1	1.74E+00	3	2.22E+00	4	
			ρ _s [g/cm ³]	2.57E+00	1	2.24E+00	3	2.49E+00	4	
			H2 ^(a)	9	K _{sxx} [m/d]	8.54E-01	1	2.03E+00	3	1.48E-01
	K _{syy} [m/d]	8.54E-01			1	2.03E+00	3	1.48E-01	4	
	K _{szz} [m/d]	8.54E-02			1	2.03E-01	3	1.48E-02	4	
	Porosity [-]	3.82E-01			1	2.73E+02	3	3.47E-01	4	
	S _r [-]	1.16E-01			1	1.33E-01	3	1.22E-01	4	
	α [1/cm]	1.17E-02			1	8.00E-03	3	1.30E-02	4	
	n [-]	1.62E+00			1	2.22E+00	3	2.45E+00	4	
	ρ _s [g/cm ³]	2.90E+00			1	2.49E+00	3	2.63E+00	4	
	H3 ^(a)	8				(b)		(b)		(b)
	Cold Creek	CCu ^(a)	7	K _{sxx} [m/d]	2.07E+00	1	4.81E-01	3	6.28E-02	4
				K _{syy} [m/d]	2.07E+00	1	4.81E-01	3	6.28E-02	4
				K _{szz} [m/d]	2.07E-01	1	4.81E-02	3	6.28E-03	4
				Porosity [-]	4.35E-01	1	4.19E-01	3	3.95E-01	4
S _r [-]				1.53E-01	1	9.70E-02	3	1.17E-01	4	
α [1/cm]				8.50E-03	1	5.00E-03	3	4.00E-03	4	
n [-]				1.85E+00	1	2.25E+00	3	2.29E+00	4	
ρ _s [g/cm ³]				2.94E+00	1	2.89E+00	3	2.83E+00	4	
CCUc ^(a)		6	K _{sxx} [m/d]	2.07E+00	1	7.30E+00	3	7.30E+00	4	
			K _{syy} [m/d]	2.07E+00	1	7.30E+00	3	7.30E+00	4	
			K _{szz} [m/d]	2.07E-01	1	7.30E-01	3	7.30E-01	4	
			Porosity [-]	4.35E-01	1	2.81E-01	3	2.81E-01	4	
			S _r [-]	1.53E-01	1	1.85E-01	3	1.85E-01	4	
			α [1/cm]	8.50E-03	1	1.10E-02	3	1.10E-02	4	
			n [-]	1.85E+00	1	1.74E+00	3	1.74E+00	4	
ρ _s [g/cm ³]	2.94E+00	1	2.39E+00	3	2.39E+00	4				

HSU	Subunit	eSTOMP Zone No.	Parameter [units]	Model 1		Model 2		Model 3	
				Model 1	Ref	Model 2	Ref	Model 3	Ref
Ringold Fm	Rtf ^(a)	5	K _{sxx} [m/d]	8.54E-01	1	4.81E-01	3	4.81E-01	4
			K _{syy} [m/d]	8.54E-01	1	4.81E-01	3	4.81E-01	4
			K _{szz} [m/d]	8.54E-02	1	4.81E-02	3	4.81E-02	4
			Porosity [-]	3.82E-01	1	4.19E-01	3	4.19E-01	4
			S _r [-]	1.16E-01	1	9.70E-02	3	9.70E-02	4
			α [1/cm]	1.17E-02	1	5.00E-03	3	5.00E-03	4
			n [-]	1.62E+00	1	2.25E+00	3	2.25E+00	4
			ρ _s [g/cm ³]	2.90E+00	1	2.89E+00	3	2.89E+00	4
	Rwie ^(a)	4	K _{sxx} [m/d]	4.84E+00	2	9.16E-01	2	6.77E-01	2
			K _{syy} [m/d]	4.84E+00	2	9.16E-01	2	6.77E-01	2
			K _{szz} [m/d]	4.84E-01	2	9.16E-02	2	6.77E-02	2
			Porosity [-]	1.50E-01	2	1.50E-01	2	1.50E-01	2
			S _r [-]	7.25E-02	1	1.20E-01	3	1.38E-01	4
			α [1/cm]	2.10E-02	1	1.40E-02	3	1.40E-02	4
			n [-]	1.37E+00	1	1.67E+00	3	1.68E+00	4
			ρ _s [g/cm ³]	2.24E+00	1	2.24E+00	3	2.24E+00	4
	Rlm ^(a)	3	K _{sxx} [m/d]	8.00E-03	2	8.00E-03	2	8.00E-03	2
			K _{syy} [m/d]	8.00E-03	2	8.00E-03	2	8.00E-03	2
			K _{szz} [m/d]	8.00E-04	2	8.00E-04	2	8.00E-04	2
			Porosity [-]	1.50E-01	2	1.50E-01	2	1.50E-01	2
			S _r [-]	1.53E-01	0	1.53E-01	0	1.53E-01	0
			α [1/cm]	8.50E-03	0	8.50E-03	0	8.50E-03	0
			n [-]	1.85E+00	0	1.85E+00	0	1.85E+00	0
			ρ _s [g/cm ³]	2.24E+00	0	2.24E+00	0	2.24E+00	0
	Rwia ^(a)	2	K _{sxx} [m/d]	1.00E+00	2	1.00E+00	2	1.00E+00	2
			K _{syy} [m/d]	1.00E+00	2	1.00E+00	2	1.00E+00	2
			K _{szz} [m/d]	1.00E-01	2	1.00E-01	2	1.00E-01	2
			Porosity [-]	1.50E-01	2	1.50E-01	2	1.50E-01	2
			S _r [-]	7.25E-02	0	7.25E-02	0	7.25E-02	0
			α [1/cm]	2.10E-02	0	2.10E-02	0	2.10E-02	0
n [-]			1.37E+00	0	1.37E+00	0	1.37E+00	0	
ρ _s [g/cm ³]			2.24E+00	0	2.24E+00	0	2.24E+00	0	
Basalt	Ba	1	K _{sxx} [m/d]	1.40E-05	0	1.40E-05	0	1.40E-05	0
			K _{syy} [m/d]	1.40E-05	0	1.40E-05	0	1.40E-05	0
			K _{szz} [m/d]	1.40E-05	0	1.40E-04	0	1.40E-05	0
			Porosity [-]	1.00E-01	0	1.00E-01	0	1.00E-01	0
			S _r [-]	7.25E-02	0	7.24E-02	0	7.25E-02	0
			α [1/cm]	2.10E-02	0	2.10E-02	0	2.10E-02	0
			n [-]	1.37E+00	0	1.37E+00	0	1.37E+00	0
			ρ _s [g/cm ³]	2.71E+00	0	2.71E+00	0	2.71E+00	0

(a) Hydraulic conductivity and porosity values used in eSTOMP were mapped from calibrated Plateau-to-River (P2R) MODFLOW model (CP-57037, Rev 2) for all model elevations below 140 m. Hydraulic parameters for higher elevations were based on parameters reported in the indicated references.

(b) H3 subunit is absent locally.

Ref. 0: Parameters were not tabulated in reference documents so assumed values were used.

Ref. 1: Parameters based on Intera's vadose zone STOMP model input file for WA-1.

Ref. 2: CP-57037, Rev. 2. (Budge, 2019; P2R Model).

Ref. 3: PNNL-14702, Rev. 1 (Last et al. 2006; Template 216T-X).

Ref. 4: PNNL-14702, Rev. 1 (Last et al. 2006; Template 216S_U_N-x).

5.2.2 Petrophysical Transform

eSTOMP outputs parameters of interconnected porosity ϕ_{int} and aqueous saturation S and tracer concentrations that are transformed into bulk electrical conductivity σ for the ERT simulations. For a partially saturated electrically resistive sediment, Archie's law (Archie 1942) describes the relationship between σ and pore space properties as

$$\sigma = \sigma_w \phi_{int}^m S^n \quad (5.1)$$

Note that surface conduction is neglected in Eq. (5.1), which is valid to a first-order, given that the target zones are permeable buried features with coarser sediments. However, further work needs to be performed on finer sediments, particularly those in the Ringold and Cold Creek units, to validate this assumption. The cementation exponent m is a function of the rate of change in pore complexity with porosity (Yue 2019), dependent on particle shape and orientation (Niu and Zhang 2018) and typically varies between 1.2 and 4.4 (Lesmes and Friedman 2005). The saturation exponent n is associated with the additional tortuosity due to the replacement of pore fluid with air (an insulator). Commonly, $n = 2$ is used and was also assumed in this assessment (e.g., Brunet et al. 2010; Day-Lewis et al. 2005).

Fluid conductivity σ_w is the summation of the background groundwater conductivity and the contribution from the tracer. Groundwater samples between 200 East and West have an average σ_w equal to 0.05 S/m (see Section 5.2.4). The composition of the ionic tracer was potassium bromide (KBr). Isono (1984) identified the relationship between KBr concentration and fluid conductivity as shown in Figure 5.5. A concentration of 60 g/L of KBr was assumed to maximize conductivity contrasts (σ_w of 4.764 S/m) while maintaining a realistic amount of KBr to be injected into the aquifer.

Initially, a value of 1.8 was used for the cementation exponent m , as this is representative for consolidated sandstones (Archie 1942; Lesmes and Friedman 2005). Also, the vadose zone conductivities were scaled by the bounds defined by the inversion of surface data at the B-Complex (Johnson and Wellman 2013) since the flow and transport modeling predicted these conductivities to be an order of magnitude lower than what was found at the B-Complex. This allowed for a more conservative approach to ERT evaluation given that depth penetration of electrical current would likely be shallower with a more resistive vadose zone, and therefore less favorable for ERT imaging.

Numerical simulations also considered a second value of m equal to 1.3 (e.g., Robinson et al. 2019) in addition to m equal to 1.8 to compare the effects on the ERT imaging and evaluate uncertainty in petrophysical parameters. The delineation of Hanford subunits H1 and H2 allowed the translated conductivities to be used as-is, and no scaling was performed on the translated conductivities.

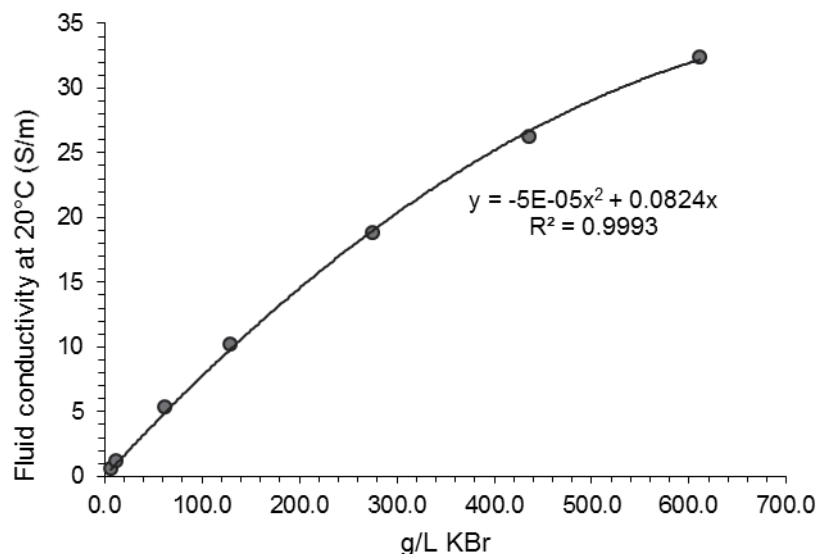


Figure 5.5. The relationship between potassium bromide (KBr) concentration and fluid conductivity (from Isono 1984).

5.2.3 Electrical Resistivity Tomography

The unstructured tetrahedral mesh used in the ERT modeling contained 1.4 million elements. Surface topography was incorporated at 50-m resolution, and from this information, nearest neighbor elevations were used for electrode elevations. The water table represented a sharp electrical conductivity contrast and was explicitly incorporated in the mesh as a variable elevation surface using the same water level measurements as in the flow and transport modeling. Since the region of interest was below the water table, finer tetrahedral elements were used below this boundary to an elevation of 0 m. The ERT modeling solved for conductivity within each tetrahedral element. Therefore, finer elements increased the ability of the model to solve for spatial variability within the region of interest.

A surface grid of 192 electrodes was simulated with dimensions of 24 x 8 electrodes (Figure 5.4 **Error! Reference source not found.**). In the easting direction, there was a 100-m separation; in the northing direction, there was a 200-m separation. The total surface area of the electrode grid was 3.22 km² (2.3 km x 1.4 km).

Before the tracer injection was simulated, a background characterization dataset was inverted to determine if the conductivity structure could delineate lithologic boundaries at the water table elevation. A constraint was added in the background modeling that favored higher conductivities in the saturated zone than in the vadose zone. This provides the inversion with realistic physical information and is enforced only if the data can fit such a constraint. Other constraints used were nearest neighbor smoothing between adjacent elements in the vadose and saturated zones.

Time-lapse ERT simulations began after the tracer injections and used the background conductivity as the starting model. Changes from the background model were inverted within the finely discretized region below the water table. This assumes there were no site activities that would produce changes in conductivity within the vadose zone that would affect the saturated zone, which is justified at this scale assuming annual recharge remains relatively constant (Oostrom et al. 2017). Decreases in conductivity were penalized, subject to data fit, which assumed conductivity remains constant or increases over time within the monitoring zone below the water table and over the simulation period. This focuses the

inversion on changes within the saturated zone due to addition of the tracer. Time-lapse simulations solved for a smooth conductivity distribution, in space and time relative to the background model.

The hypothetical 3D ERT survey consisted of a focused 2828 four-electrode measurements. The configuration only collected data where current and potential electrodes all fall in the same row or column. Noise levels were assumed to be 2% with an absolute error of 0.001 ohms, which is based on previous studies in the 300 Area (Johnson and Wellman 2013). The simulation summary is in Table 5.3.

Table 5.3. Phase 1 conceptualization used in ERT feasibility evaluation.

Tracer Volume	757 m ³
Archie's Petrophysical Parameters	<i>m</i> =1.8 <i>n</i> =2
Tracer (KBr) Concentration	60 g/L
ERT Survey ^(a)	F=Focused

(a) Focused survey contains 2,828 measurements.

An additional comprehensive hypothetical ERT survey was evaluated that contained 21,822 measurements consisting of Wenner, Schlumberger, and dipole-dipole measurements. Additional measurements have the potential to provide more information on the subsurface, particularly for background/characterization imaging. However, a larger number of measurements translates to increased computational time and the intent of providing additional information may not hold true. In time-lapse imaging, a larger number of measurements will increase temporal smearing (i.e. it takes a longer amount of time over which data is collected), which might not represent a 'snapshot' of subsurface processes. These tradeoffs are evaluated below. The simulation summary exploring uncertainty is in Table 5.4 and Table 5.5.

Table 5.4. Phase 2, Models 1 and 3 Conceptualizations used in ERT feasibility evaluation

Tracer Volume	757 m ³											
Archie's Petrophysical Parameters	<i>m</i> =1.3 <i>n</i> =2						<i>m</i> =1.8 <i>n</i> =2					
Tracer (KBr) Concentration	40 g/L		60 g/L		80 g/L		40 g/L		60 g/L		80 g/L	
ERT Survey	F	C	F	C	F	C	F	C	F	C	F	C

F=Focused survey contains 2,828 measurements.
C=Comprehensive survey contains 21,822 measurements.

Table 5.5. Phase 2, Model 2 conceptualizations used in ERT feasibility evaluation

Tracer Volume	378 m ³				757 m ³				1135 m ³									
Archie's Petrophysical Parameters	<i>m</i> =1.3 <i>n</i> =2				<i>m</i> =1.3 <i>n</i> =2				<i>m</i> =1.8 <i>n</i> =2				<i>m</i> =1.3 <i>n</i> =2					
Tracer (KBr) Concentration	60 g/L		40 g/L		60 g/L		80 g/L		40 g/L		60 g/L		80 g/L		60 g/L			
ERT Survey	F		F	C	F	C	F	C	F	C	F	C	F	C	F	C	F	C

F=Focused survey contains 2,828 measurements.
C=Comprehensive survey contains 21,822 measurements.

5.2.4 Other Modeling Considerations

Nitrate is an inorganic dissolved solid that carries a negative ionic charge and therefore increases fluid conductivity. Nitrate is present throughout the Hanford Central Plateau. Since ERT cannot distinguish between ionic sources, nitrate in large concentrations could mimic the response from an injected tracer.

While this would not necessarily be detrimental to paleochannel identification (i.e., presumably nitrate would also preferentially flow within the paleochannel), the impact of nitrate within the groundwater needs to be quantified. Between 200 East and West, there are no known persistent source locations leaching nitrate; therefore, historical records were used to determine existing concentrations.

Nitrate concentrations have been measured for decades and are available through the Hanford Environmental Information System (HEIS), which can be accessed via PHOENIX (<https://phoenix.pnnl.gov>). Fluid specific conductance is also routinely determined from collected groundwater samples. It was assumed that nitrate is correlated with fluid specific conductance, more than any other constituent in the groundwater, and therefore could act as a marker of nitrate concentrations (Oostrom et al. 2017). For co-located sample ID and dates, nitrate and fluid specific conductance were retrieved for all wells between 200 East and West Areas. Thirty-four unique well locations were identified in this area, and a total of 667 total records were retrieved over the date range 12/12/1983-11/2/2018. The coefficient of determination (R^2) of fluid specific conductance versus nitrate concentration was equal to 0.611 (Figure 5.6). Therefore, a first-order linear fluid specific conductance relation (Figure 5.6) could be used as a proxy for nitrate concentrations. For the tracer, the regression equation shown in Figure 5.5 was used to convert simulated tracer concentrations to σ_w in Eq. (5.1).

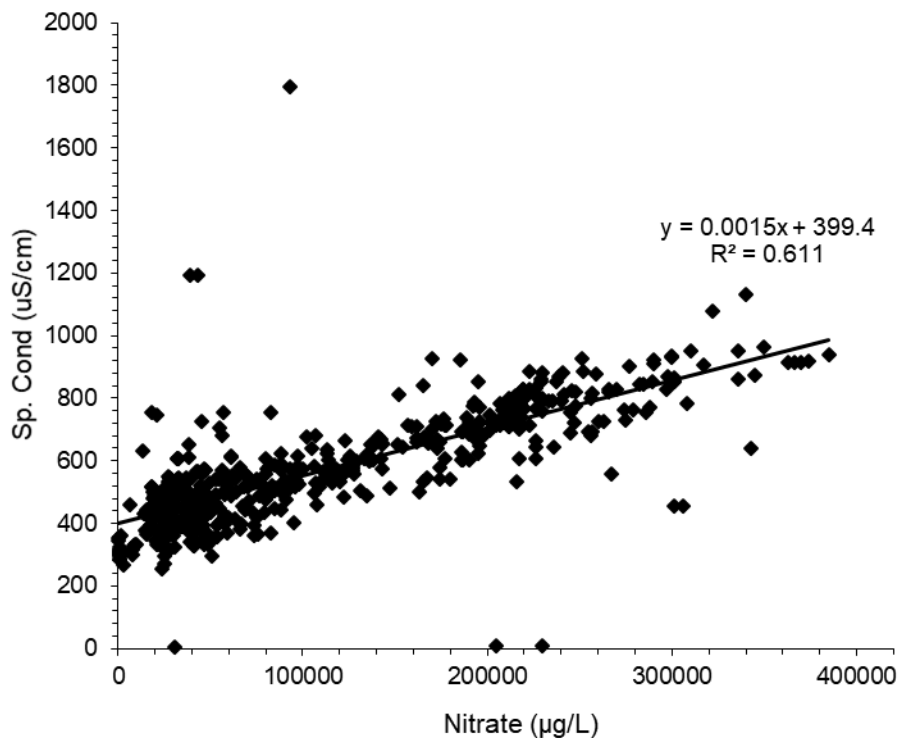


Figure 5.6. A comparison of HEIS nitrate concentrations and fluid specific conductance from boreholes within and surrounding the area between 200 East and West Areas between 12/12/1983 and 11/2/2018.

Average and median specific conductance from the collection of wells between 200 East and West are 0.0552 S/m (std dev=0.0176 S/m) and 0.0516 S/m, respectively. Using a value of 60 g/L in the regression equation in Figure 5.5, the theoretical fluid conductivity of the tracer is 4.7 S/m; at 90% dilution (or 6 g/L), the theoretical fluid conductivity is 0.49 S/m. A tracer fluid conductivity of 0.49 S/m (at 20 deg C) is one order of magnitude higher than 0.0052 S/m, the average specific conductance (at 25 deg C), noting

that this large difference cannot be attributed to a 5 deg C temperature variability in the reported conductivities. Therefore, given the low fluid specific conductance due to the presence of nitrate and the lack of persistent nitrate sources in this area, nitrate was not considered or accounted for as a source in the flow and transport modeling.

5.3 Simulation Results

5.3.1 Flow and Transport

The flow and transport results for the tracer injection are shown in Figure 5.7. For both candidate injection wells, minimum lateral spreading occurs during the first few years of simulation (Figure 5.7a-c). By 2025 (Figure 5.7d), more significant lateral spreading occurs near well 699-49-69 in the direction of groundwater flow because the tracer has entered the high-permeability paleochannel. By contrast, the tracer injection from MW-10A shows less horizontal spreading and quicker southeasterly flow direction due to its location within the paleochannel. For both wells, the trajectories of the simulated plumes follow the boundary of paleochannel as depicted in the GFM.

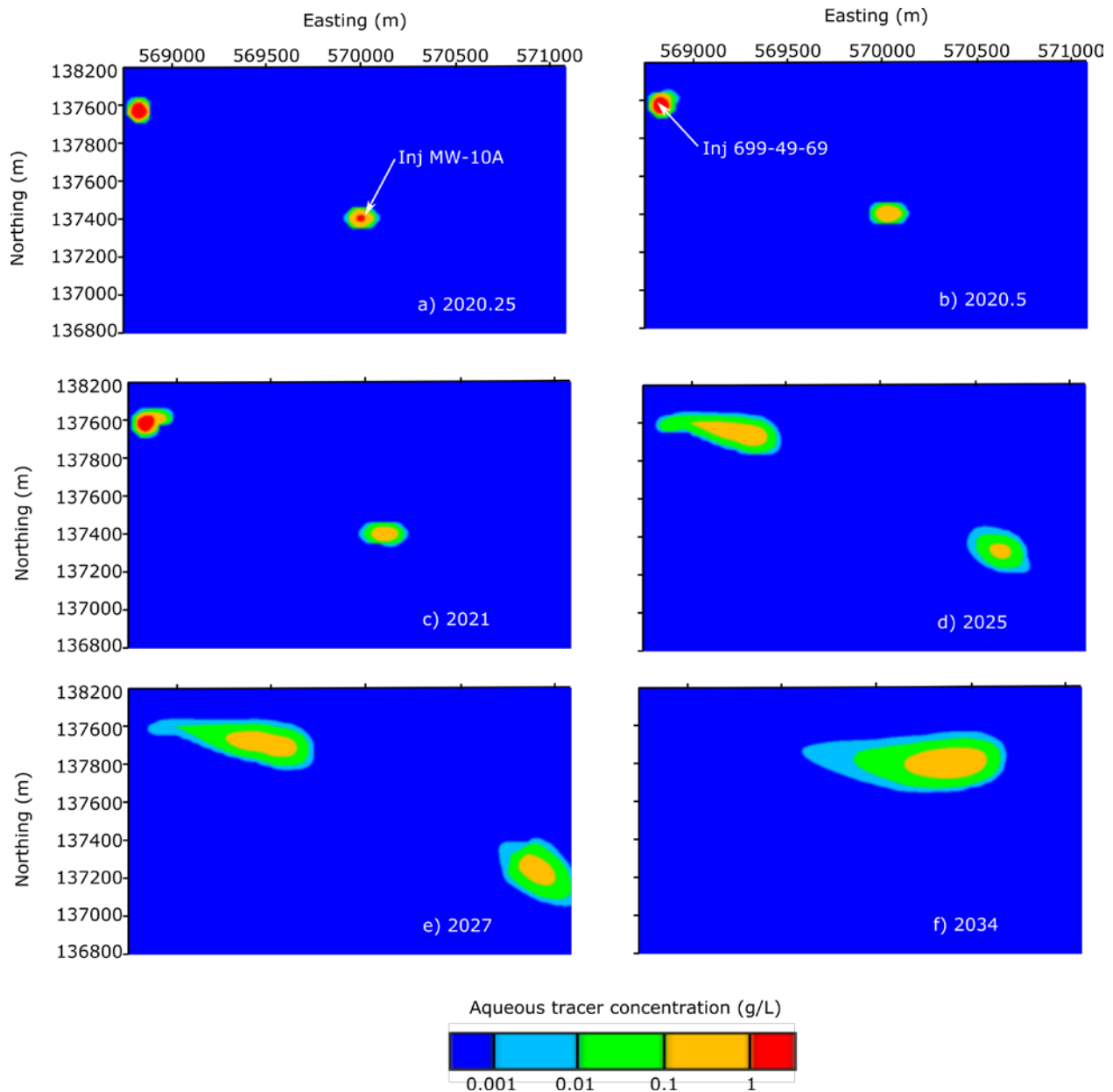


Figure 5.7. Results of flow and transport simulations of a tracer injection into wells 699-49-69 and MW-10A at elevation 120 m. Shown are plan views of the model domain aqueous concentrations after the tracer injection ceased in 2020 a) 2020.25; b) 2020.5; c) 2021; d) 2025; e) 2027; f) 2034.

5.3.2 Electrical Resistivity Tomography

The background ERT image is shown alongside the σ field computed from the flow and transport modeling results in Figure 5.7. The images on the left (Figure 5.8a-b) are the plan and elevation views of the flow and transport σ and electrodes are shown for reference. The images on the right (Figure 5.8c-d) are the inverted ERT images. The color scale for the ERT images has a maximum value that is one order of magnitude lower than for the flow and transport σ so that the conductivity structure can be observed. In general, the plan views (Figure 5.8a and Figure 5.8c) show a similar structure, although the ERT σ

(Figure 5.8c) structure is less resolved. This is especially noticeable near the edges of the electrode grid, where measurement density is lower. Resolution with depth, from the surface to the basalt, is shown in Figure 5.8b and Figure 5.8d for the groundwater model and ERT image, respectively. Using nearest-neighbor smoothness constraints within the water table (~70-m depth), the ERT inversion fit the data to a model with the least amount of structure that can satisfy the data. The ERT image shows limitations in its ability to resolve stratigraphy with depth relative to the stratigraphy represented in the groundwater model (Figure 5.8a and Figure 5.8b). For this electrode configuration, stratigraphy is better resolved in the lateral directions than with depth.

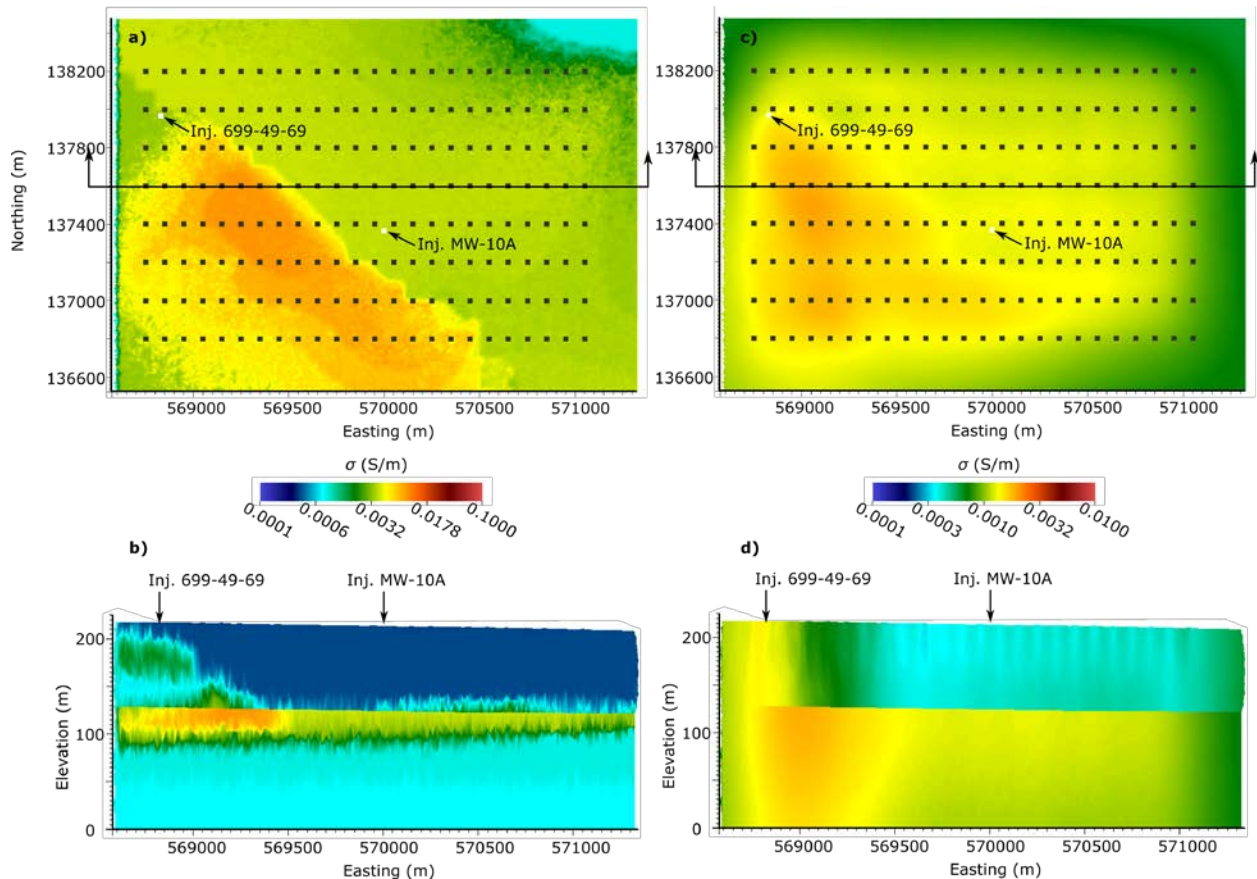


Figure 5.8. Flow and transport σ in plan view a) and elevation view b). Background ERT σ images are shown in plan view c) and elevation view with a 5:1 vertical exaggeration d). Color scales are one order of magnitude lower for the ERT σ relative to the flow and transport model σ to highlight the variability in conductivity structure of the ERT σ , which would otherwise not be visible.

Time-lapse ERT imaging results are compared to the flow and transport σ in Figure 5.9 as logarithmic changes in conductivity relative to background. ERT images are shown as orange-shaded isosurfaces and the flow and transport model σ is shown as blue-shaded isosurfaces. The color scales differ between the two images because ERT the image is less resolved than the flow and transport model-based σ .

Images are shown for select years to represent early and late times in the injection migration. The first result shown is at 2020.25, 3 months after the tracer injections ceased at wells 699-49-69 and MW-10A (Figure 5.9a). While images before this date detected changes in bulk conductivity, 2020.25 is the first image of changes occurring near the injection wells. ERT imaging artifacts are also noted in these images,

where ERT identifies changes that do not correspond to the flow and transport model σ . These are more evident in early times but dissipate at later times (Figure 5.9b). The ERT estimated σ overlaps the spatial extent of the flow and transport model-based σ , and appears as more spatially extensive due to the resolution limitations in the inversion modeling.

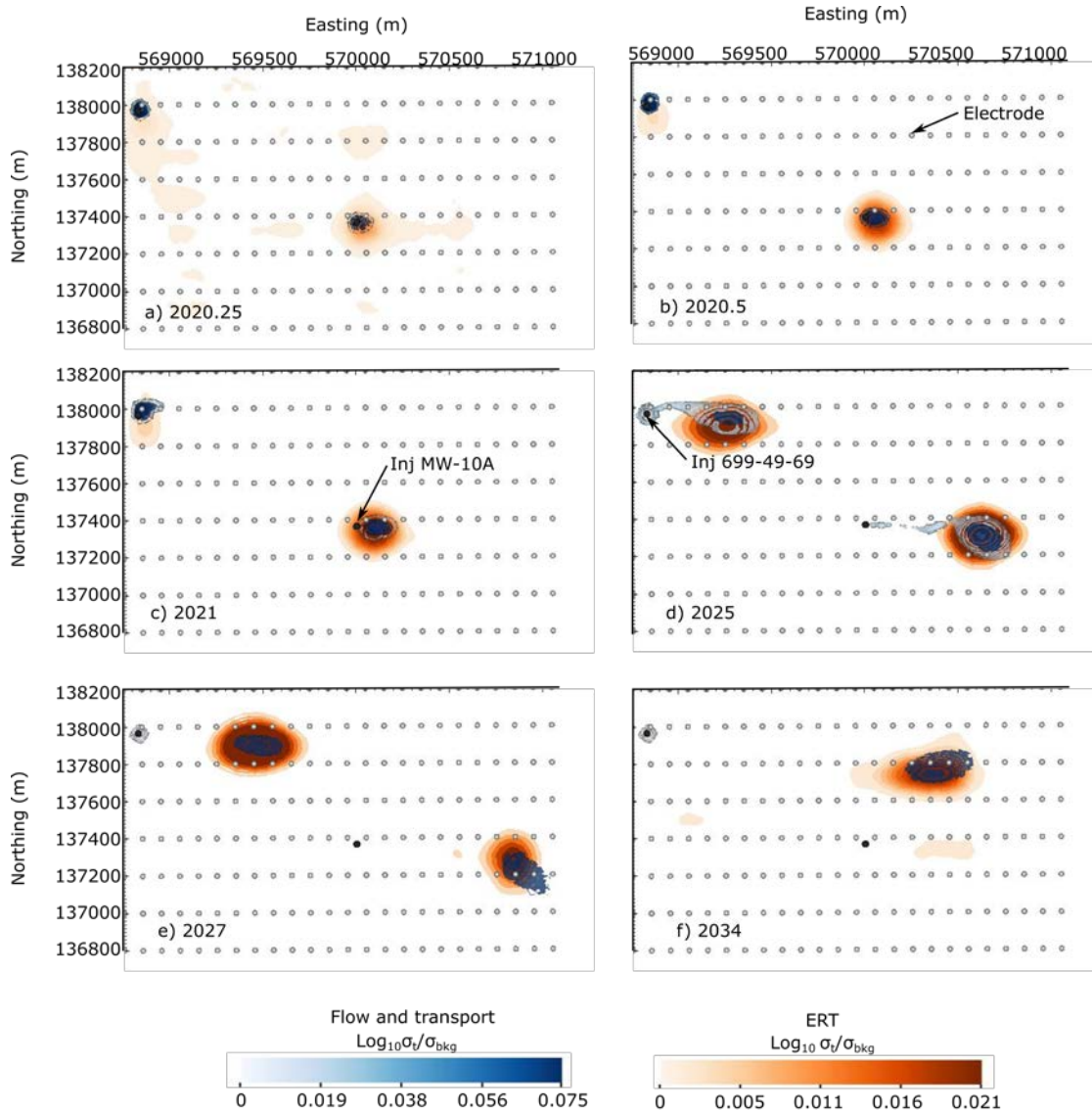


Figure 5.9. Time-lapse ERT σ results alongside flow and transport σ conceptual site models. Both models are represented as isosurfaces of logarithmic change from background (year 2020) values. Simulations results are shown after the tracer injection has ceased at a) 2020.25; b) 2020.5; c) 2021; d) 2025; e) 2027; and f) 2034.

5.4 Simulation Results Exploring Uncertainty

5.4.1 Flow and Transport

The flow and transport results for the tracer injection are shown in Figure 5.10 for Models 1, 2 and 3 at an elevation of 120 m, the average depth of the water table. For all models, there is minimum lateral spreading during the first 6 months (top two rows in Figure 5.10) after the injection. Lateral spreading increases near well MW-10A by year 2022 and by year 2028 and through year 2040, concentrations reduce. For injection well 699-49-69, lateral spreading occurs between years 2022 through year 2040. Given the slow tracer movement, differences between the Models 1,2 and 3 tracer trajectories are marginal in Figure 5.10 and are not visible until year 2028. Flow and transport simulations were run out to year 2120, 100 years after the tracer injection; there was no tracer concentration remaining within the boundaries shown.

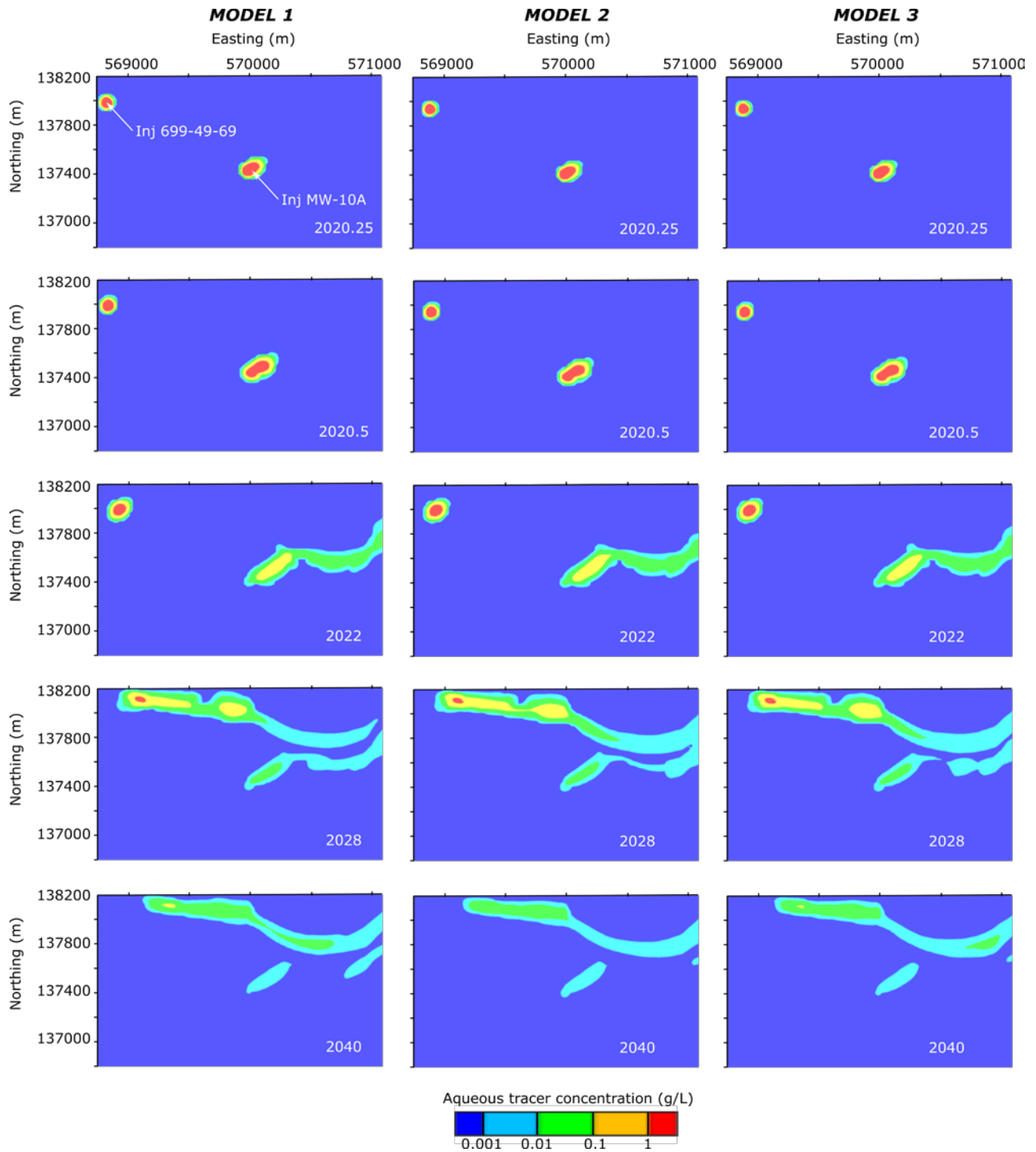


Figure 5.10. Tracer injection models at elevation 120 m from flow and transport simulations for Models 1, 2, and 3 with a tracer volume of 757 m³ and a tracer concentration of 60 g/L.

5.4.2 Background/Characterization Electrical Resistivity Tomography

The steady-state flow and transport σ are presented with background ERT images below. These are presented as cross-sections sliced at 137500 N. This orientation reveals the electrical conductivity structure in the general direction of fluid transport across the 200 Area. These flow and transport σ demonstrate the range of bulk electrical conductivity predicted when varying 1) hydrologic parameters (e.g. porosity and saturation) and 2) Archie's cementation exponent m . Modeled ERT images are shown below each flow and transport σ . The color scale used for the ERT images was selected to show the maximum range of electrical conductivities.

The flow and transport σ for Models 1 and 3 (Figure 5.11A and B) have larger electrical conductivity values in the vadose zone (>120 m elevation), which is mostly represented by the Hanford formation H2 subunit. Model 1 has a layer with noticeably larger electrical conductivity than Model 3. In the ERT images (Figure 5.11C and D), the ability of ERT to image variability within the vadose zone is limited in Model 1 by the shallow high electrical conductivity layers. For Model 3, a contrast is detected; however, highly conductive features near the water table resulted in vertical contrasts appearing in the section, whereas these features are horizontal in the flow and transport σ (Figure 5.11B).

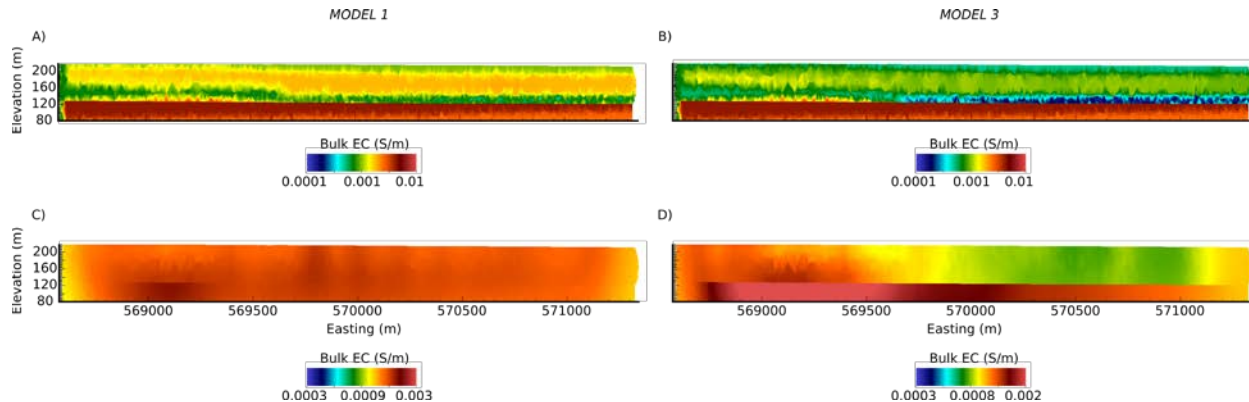


Figure 5.11. Bulk EC Models 1 and 3 shown for the comprehensive survey where $m=1.3$. Flow and transport σ are shown for A) Model 1 and B) Model 3. Corresponding ERT modeling results are shown in C) and D).

A summary of characterization simulations for Model 2 is shown in Figure 5.12 using the comprehensive ERT survey and $m=1.3$ and $m=1.8$. The impact of varying m on the flow and transport σ is evident and clearly affects the ability of ERT to resolve subsurface structure. Horizontal contacts are better delineated where there are higher electrical conductivities (Figure 5.12C).

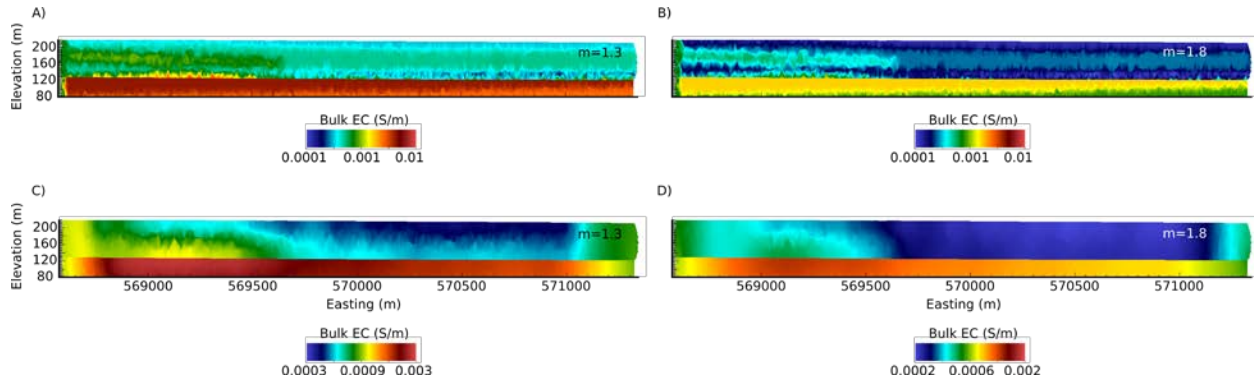


Figure 5.12. Bulk EC Model 2 shown for the comprehensive survey. Flow and transport σ are shown for A) $m=1.3$ and B) $m=1.8$. Corresponding ERT modeling results are shown in C) and D).

Figure 5.13 compares results obtained using the comprehensive (21,822 measurements) versus a focused (2,828 measurements) ERT survey. While the comprehensive survey has finer resolution and details, the impact to the overall electrical conductivity structure interpretation in this case is marginal, even though the number of measurements in the focused survey is about 13% of comprehensive survey. ERT survey optimization is an active area of research, and this study demonstrates the ability to reduce field data acquisition times (and processing); however, sites should be evaluated on a case-by-case basis.

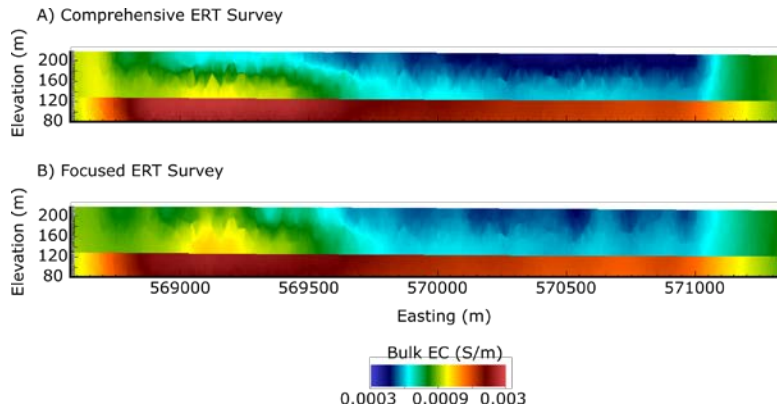


Figure 5.13. ERT Bulk EC for Model 2 comparing imaging results when using A) comprehensive survey and B) focused survey.

For characterization imaging, the figures show that the electrical conductivity contrast between stratigraphic units is less than one order of magnitude. As in the first set of simulations, horizontal layering is less well resolved than vertical contacts. Vertical contacts in the uncertainty simulations are delineated relatively well in all the ERT characterization models, except Model 1, where the layer with larger electrical conductivity in the vadose zone impacts the ability of ERT to provide realistic imaging with depth.

In Model 2, the larger value of m resulted in less-well-resolved features in the ERT imaging based on more resistive σ generated by the flow and transport model. Electrical current flow will preferentially move through more conductive units, and the impact of this in the ERT imaging can have opposing effects. First, if uppermost units are too conductive, then current flow will not penetrate to deeper units and resolution will be limited (as shown for Model 1 above). However, when comparing 5.12C to 5.12 D, the resistive units are not well-delineated because less current density is transmitted. This tradeoff is apparent in Figure 5.12 and can either improve or worsen imaging results.

5.4.3 Time-lapse Electrical Resistivity Tomography

To evaluate uncertainty in the flow and transport σ conceptualizations described in Table 5.4 and Table 5.5, relative changes in σ were assessed through time-lapse imaging. ERT time-lapse modeling uses constraints (refer to Section 5.2.3) in producing an electrical conductivity model, subject to data fit. Therefore, changes in the data cannot strictly be used to indicate if the tracer will be spatially well delineated. However, temporal changes in the data must exist for the ERT inverse-modeling simulation to identify a temporal change in electrical conductivity. Comparing the magnitude of changes across different flow and transport σ conceptualizations can inform ERT simulations; however, it cannot be used as a replacement for full inverse modeling.

Changes in the synthetic ERT data are expressed as logarithmic change in apparent conductivity σ_{app} from the background year of 2020:

$$\Delta \log \sigma_{app} = \log \sigma_{app}(t) - \log \sigma_{app}(2020) \quad (5.2)$$

where t is the first year simulated and $\Delta \log \sigma_{app}$ represents an average within the domain. Since the tracer volume is small relative to the simulation domain, the use of averages may amplify outliers and highlight large or small localized changes in the data. Figure 5.14 compares the impact of the hydrologic parameter variations in Models 1, 2, and 3 on the ERT synthetic datasets using the focused ERT survey. The changes in the data rise and hit a peak at year 2022, and then decrease until year 2040. Model 2 has the largest changes. Figure 5.15 evaluates the impact of Archie's m exponent on the data. A higher value of this parameter results in smaller changes in the data. As expected, an increase in tracer volume (Figure 5.16) and tracer concentration (Figure 5.17) results in larger changes to apparent conductivity. Note that decreasing Archie's m exponent value has as much impact as increasing the tracer volume and/or concentration.

Finally, Figure 5.18 compares data changes using the comprehensive and focused ERT surveys. The comprehensive survey depicts smaller changes in the data, a likely consequence when many measurements have little or no change over time within the ERT electrode grid. For both configurations, changes in the bulk conductivity are too small to detect tracer movement past the year 2036.

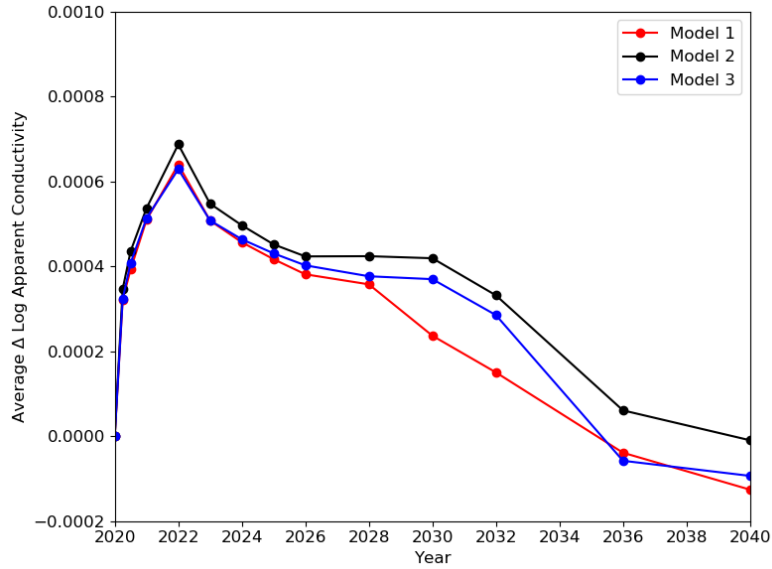


Figure 5.14. Average changes in $\Delta \log \sigma_{app}$ for Models 1, 2, and 3 with the focused ERT survey. A tracer concentration of 60 g/L and a tracer volume of 757 m³ (200,000 gallons) at two injection locations were used.

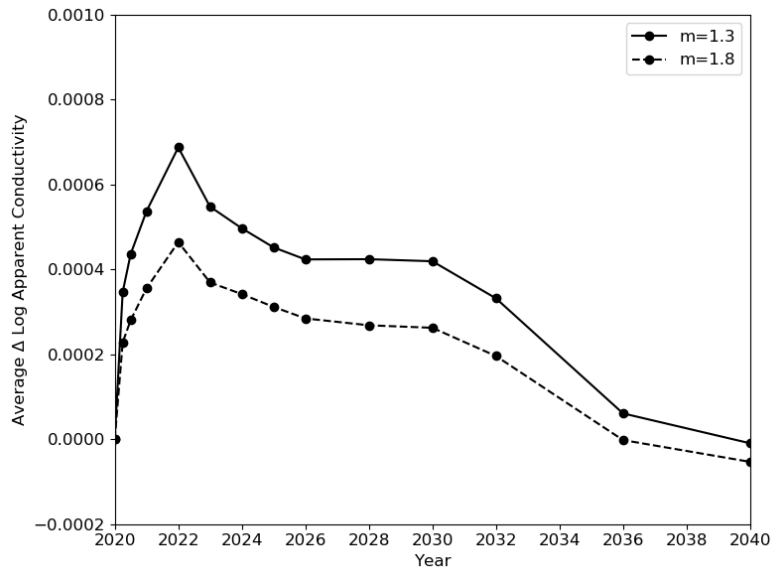


Figure 5.15. Average changes in $\Delta \log \sigma_{app}$ from 2020 using Model 2 and the focused ERT survey. tracer concentration of 60 g/L and a tracer volume of 757 m³ (200,000 gallons) at two injection locations were used.

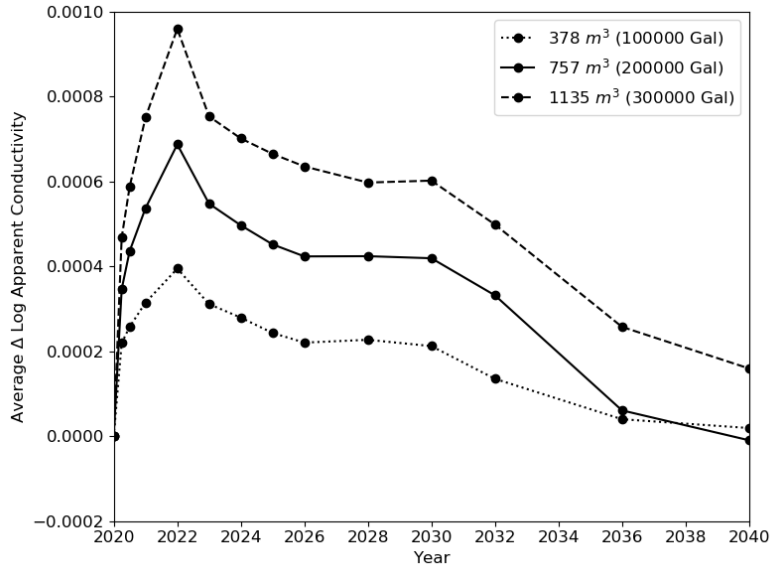


Figure 5.16. Average changes in $\Delta \log \sigma_{app}$ from 2020 using Model 2 and the focused ERT survey for different volumes of injected tracer. A tracer concentration of 60 g/L at two injection locations was used.

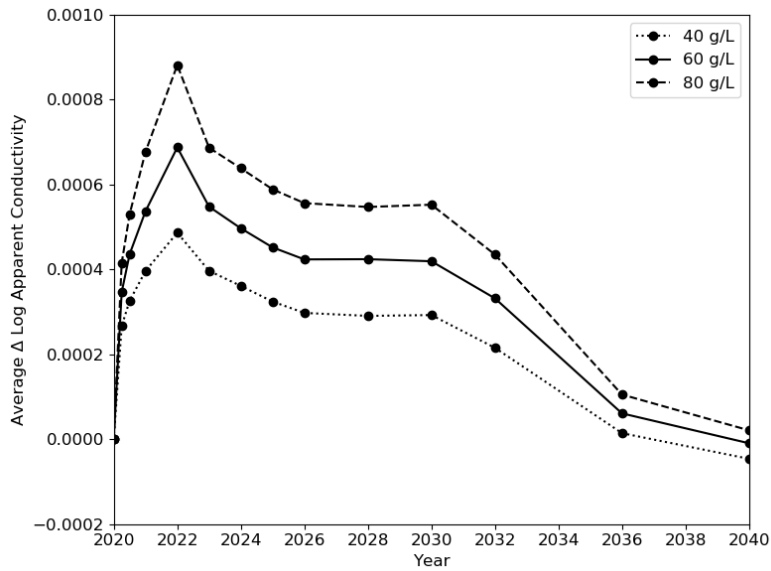


Figure 5.17. Average changes in $\Delta \log \sigma_{app}$ from 2020 using Model 2 and the focused ERT survey for different concentrations of injected tracer. A tracer volume of 757 m³ (200,000 gallons) at two injection locations was used.

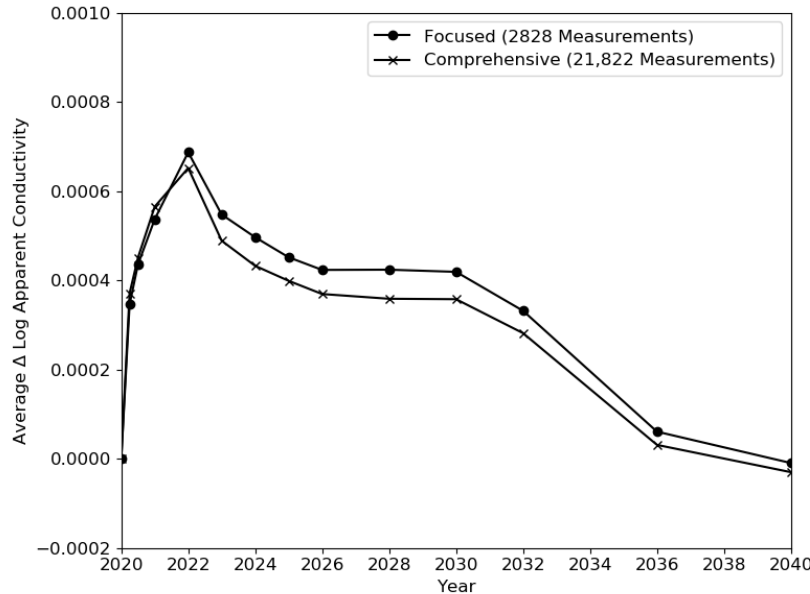


Figure 5.18. Average changes in $\Delta \log \sigma_{app}$ from 2020 using Model 2 resulting from different measurement configurations. A tracer concentration of 60 g/L and a tracer volume of 757 m³ (200,000 gallons) at two injection locations were used.

Time-lapse images are shown in Figure 5.19 through Figure 5.21 for 3 years: 2020.5, 2022, and 2028 for Models 1, 2, and 3 beyond year 2028. Year 2020.5 (6 months after the tracer is injected) is the first time-step where there is a clear detection of the tracer across multiple simulations. Time-lapse images show the flow and transport σ in a blue color scale alongside the bulk EC in an orange color scale.

Many of the low tracer concentration regions (< 0.01 g/L) depicted in Figure 5.10 are not visible as changes bulk EC in the flow and transport model (blue color scale). These low concentrations had little effect on the saturation and/or concentration, resulting in less of a contrast in the bulk EC see Archie's Law [Eq. (5.1)], and therefore do not serve as target areas for field-scale ERT.

A comparison of the focused ERT survey results for Models 1, 2, and 3 is shown in Figure 5.19 using a tracer volume of 757 m³ and a tracer concentration of 60 g/L. Only Model 2 reliably predicts the location of the tracer injection at year 2020.5. In Year 2022 (Figure 5.19b, e, h), Models 1 and 2 predict the location of the tracer near the injection wells; however, the lower concentration tail shown in the flow and transport model-based σ is not resolved. By the year 2028, tracer concentrations are detected to have moved west; however, changes are localized near the injection wells. Relative to Models 1 and 2, Model 3 poorly resolves the tracer transport.

Intuitively, a larger tracer injection volume should increase the ability of ERT to detect the tracer due to a larger spatial impact. Figure 5.20 shows the ERT modeling results for Model 2 with a tracer concentration of 60 g/L for three injection volumes: 378 m³, 757 m³, and 1135 m³. For an injection volume of 378 m³, ERT detection is minimal. The ERT detection increases for 757 m³ and 1135 m³; however, for both volumes, the low-conductivity tracer tail in the flow and transport σ is not well resolved.

Similarly, increasing the tracer concentration should increase the ability of ERT to detect the tracer due to a larger electrical conductivity contrast with a background state. Figure 5.21 shows the ERT modeling results for Model 2 with an injection volume of 757 m³ and injection concentrations of 40, 60, and 80 g/L. Using 40 g/L (Figure 5.21 a-c), the tracer injection is detected by ERT; however, it has a small footprint.

This ERT detection area increases using 60 g/L and 80 g/L, but changes are local to the injection wells. Relative to increasing the tracer injection concentration, increasing the tracer volume has a larger impact on ERT detection. For example, a tracer concentration and volume of 60 g/L and 378 m³, respectively (Figure 5.20a-c) is less detectable in the ERT images than using a tracer concentration and volume of 40 g/L and 757 m³, respectively (Figure 5.21a-c).

Other ERT temporal images evaluating the comprehensive versus focused ERT survey and Archie’s m parameter ($m=1.3$ and $m=1.8$) were compared. It was found that relative to the focused ERT survey, the comprehensive ERT survey was more prone to artifacts in the time-lapse images but had a similar delineation of the tracer injection. Similar results were found where $m=1.3$ and $m=1.8$.

For the ERT time-lapse analysis, changes in bulk EC were detected using the tracer to varying degrees. However, given that lower concentration areas predicted by the flow and transport model simulations did not result in large bulk EC changes, the spatial footprint to evaluate ERT feasibility was limited.

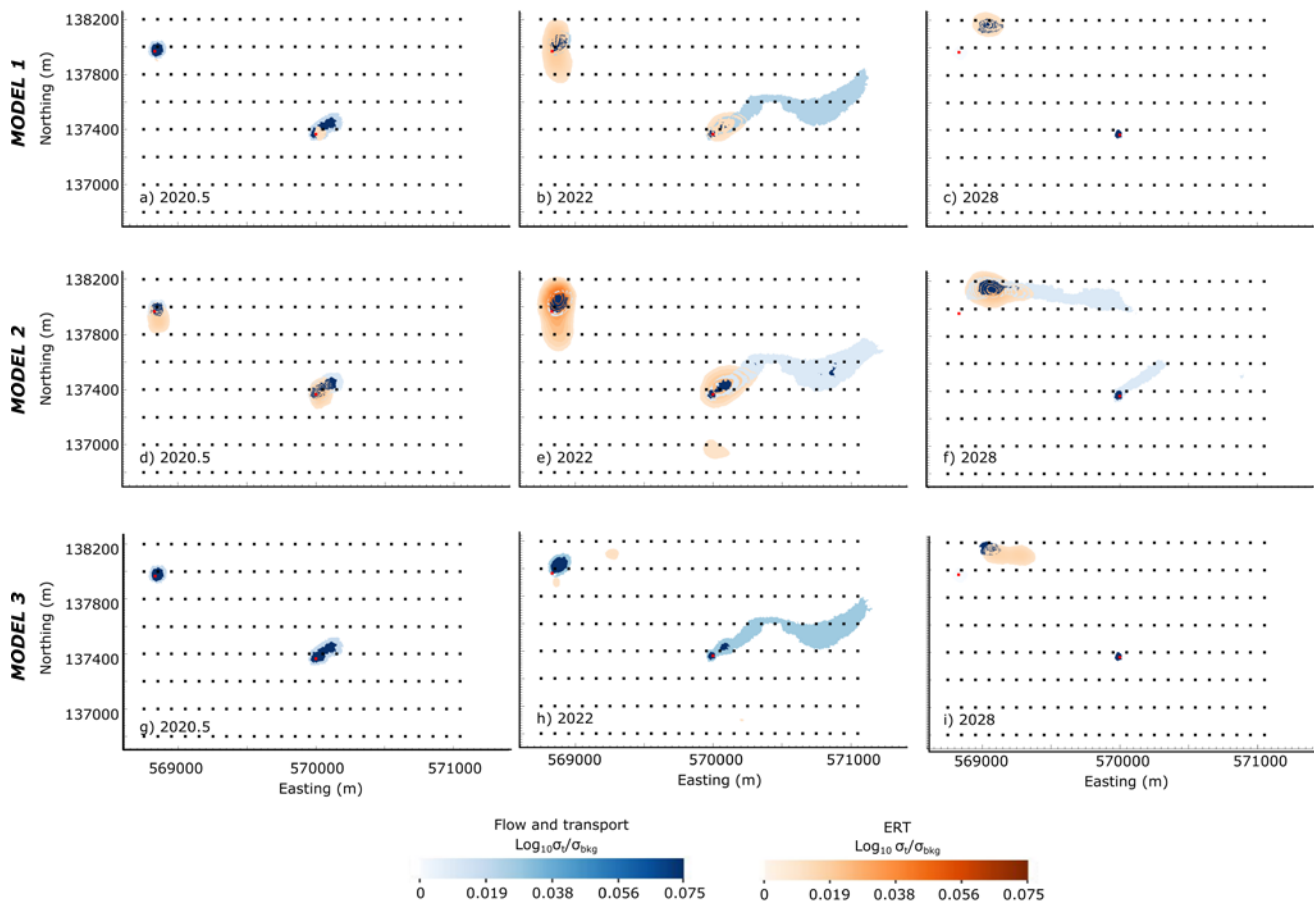


Figure 5.19. Synthetic Models 1, 2, and 3 at elevation 120 m for a 60 g/L tracer injection for years 2020.5, 2022, and 2028. Archie parameters used in the synthetic modeling were $m=1.3$ and $n=2$.

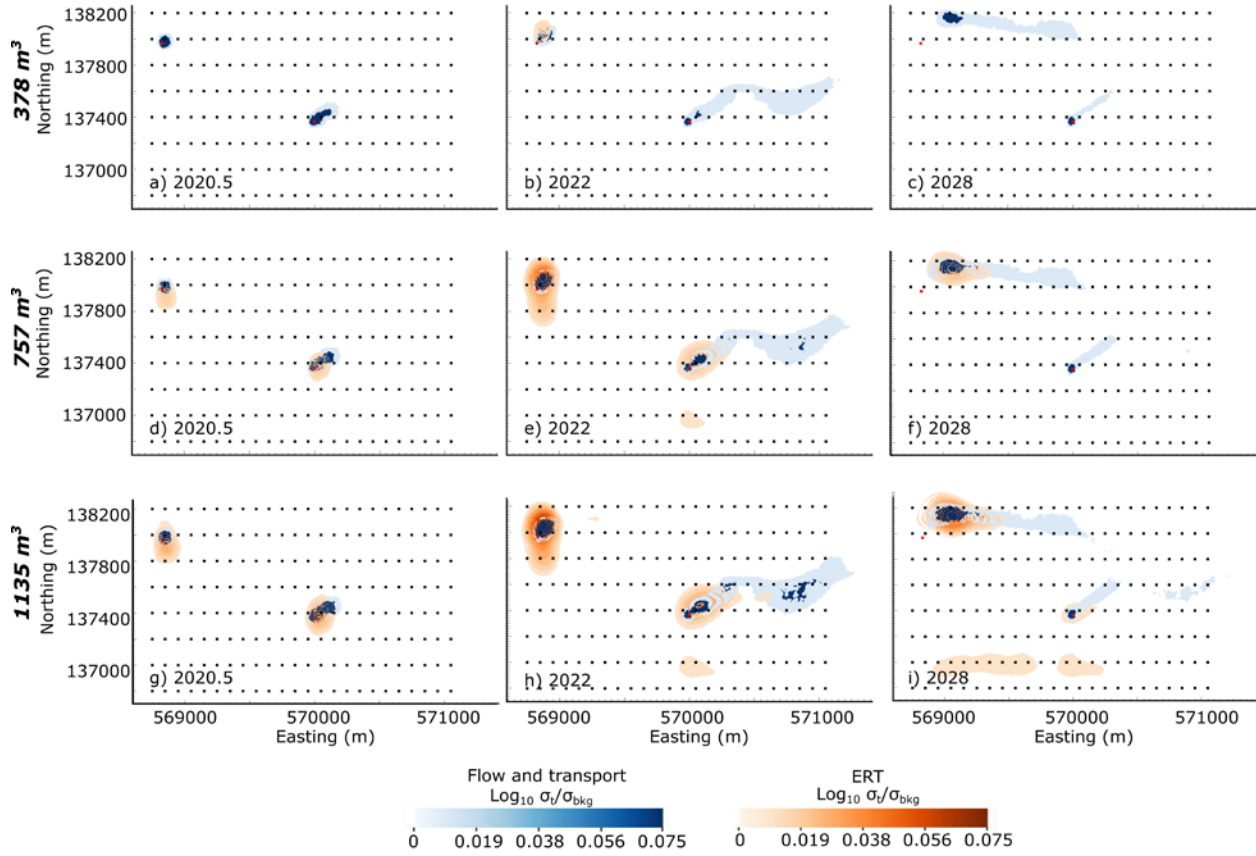


Figure 5.20. Synthetic Model 2 at elevation 120 m using a 60 g/L tracer injection for years 2020.5, 2022, and 2028 for injection volumes 378 m³, 757 m³, and 1135 m³. Archie parameters used in the synthetic modeling were $m=1.3$ and $n=2$.

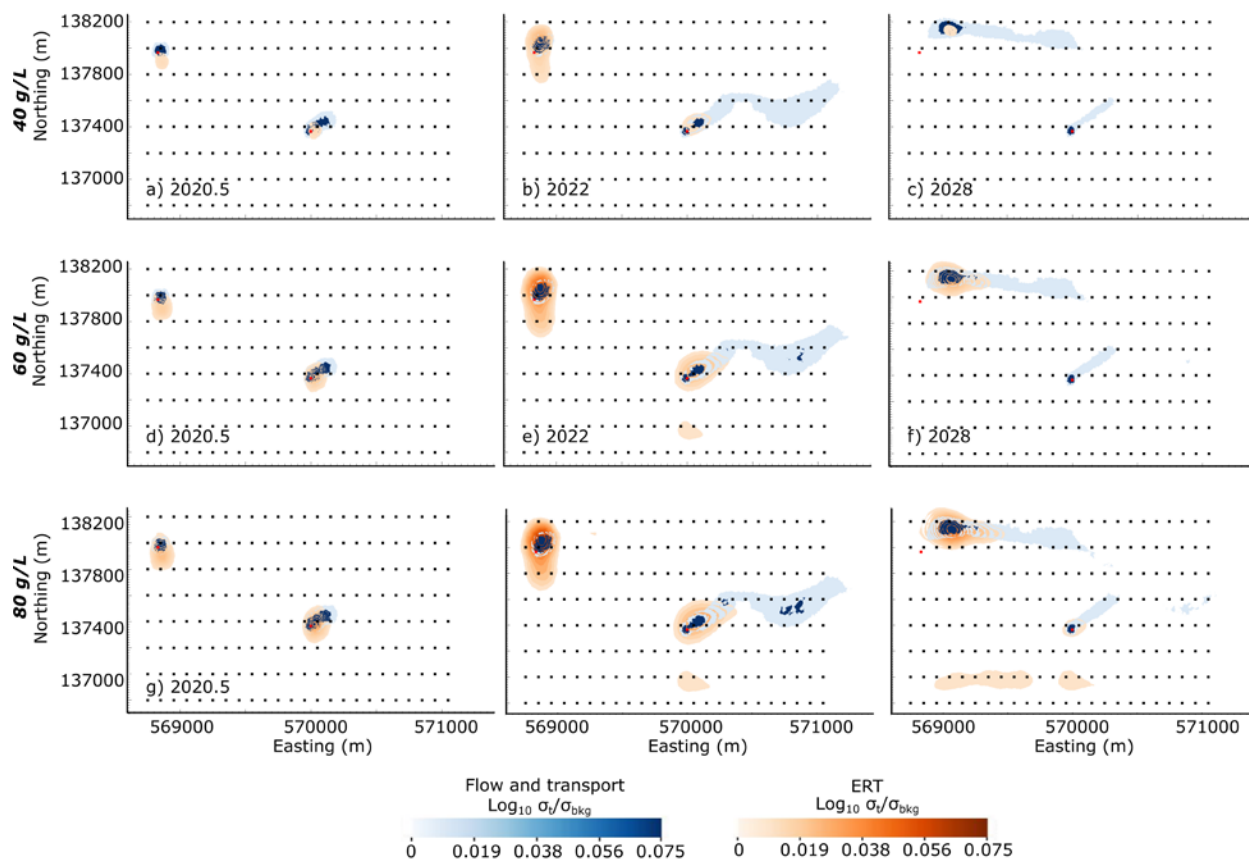


Figure 5.21. Synthetic Model 2 at elevation 120 m with an injection volume of 757 m³, with 40, 60, and 80 g/L tracer concentration for years 2020.5, 2022, and 2028. Archie parameters used in the synthetic modeling were $m=1.3$ and $n=2$.

5.5 ERT Feasibility Evaluation Conclusions

Based on a conceptual geologic framework and transient flow and transport model simulations, 3D surface ERT simulations were used to determine if ERT static and transient imaging can be used to detect tracer movement. A single conceptualization showed static conductivity (stratigraphic) structures from a background image (Figure 5.8) and tracer migration from injections in two separate wells using time-lapse imaging (Figure 5.9). This analysis revealed that 3D surface static imaging can provide limited information on electrical conductivity contrasts related to lithologic boundaries at the depth of interest (~70 m below ground surface) and is better at delineating vertical contacts relative to horizontal layering. In the time-lapse ERT simulation, the tracer was delineated only when the tracer concentration (60 g/L) and volume (757 m³) were high. However, detection limits could potentially be within field site noise levels.

Multiple conceptualizations were considered in evaluating ERT uncertainty. Static ERT imaging was more promising where vadose zone layering was less conductive in the GFM, which was determined by the hydrologic properties used in Models 1, 2, and 3 and the Archie's m value. Differentiation of vadose zone units (e.g., Hanford formation units) was limited; however, larger contrasts were detected. Time-lapse ERT imaging showed mostly localized changes near the injection wells, in part due to flow and transport simulations predicting concentrations (< 0.01 g/L) that provided a low bulk electrical conductivity contrast to evaluate ERT feasibility.

Field-deployment must consider the assumptions made in the flow and transport and ERT modeling. While some of these assumptions were considered by varying parameter estimates, variability within the geologic framework was not considered. Although aquifer parameters were modeled to be spatially variable in all directions, continuous hydrostratigraphy, and the physical properties within the vadose zone, were assumed to be constant. The cementation m and saturation n exponents defined in the Archie transformation [Eq. (5.1)] were assumed to be constant for all units, since formation-specific parameters were not available. If any of these assumptions are violated, then ERT may not be able to detect major stratigraphic units in the field.

6.0 ERT Field Evaluation

The pre-field feasibility simulations in Section 5.0 highlight variability and uncertainty in the ERT evaluation. Several of the factors contributing to uncertainty, including ambient bulk electrical conductivity, data noise and depth of resolution, were evaluated through a surface ERT field data campaign between the 200 East and West areas. The field site is shown in Figure 6.1. This site was chosen based on the GFM shown in Figure 5.2, such that the ERT line would cross the presumed boundary of one or more Hanford-Ringold stratigraphic contacts. E4D (<https://e4d-userguide.pnnl.gov/>, Johnson 2014) was used to interpret field data.

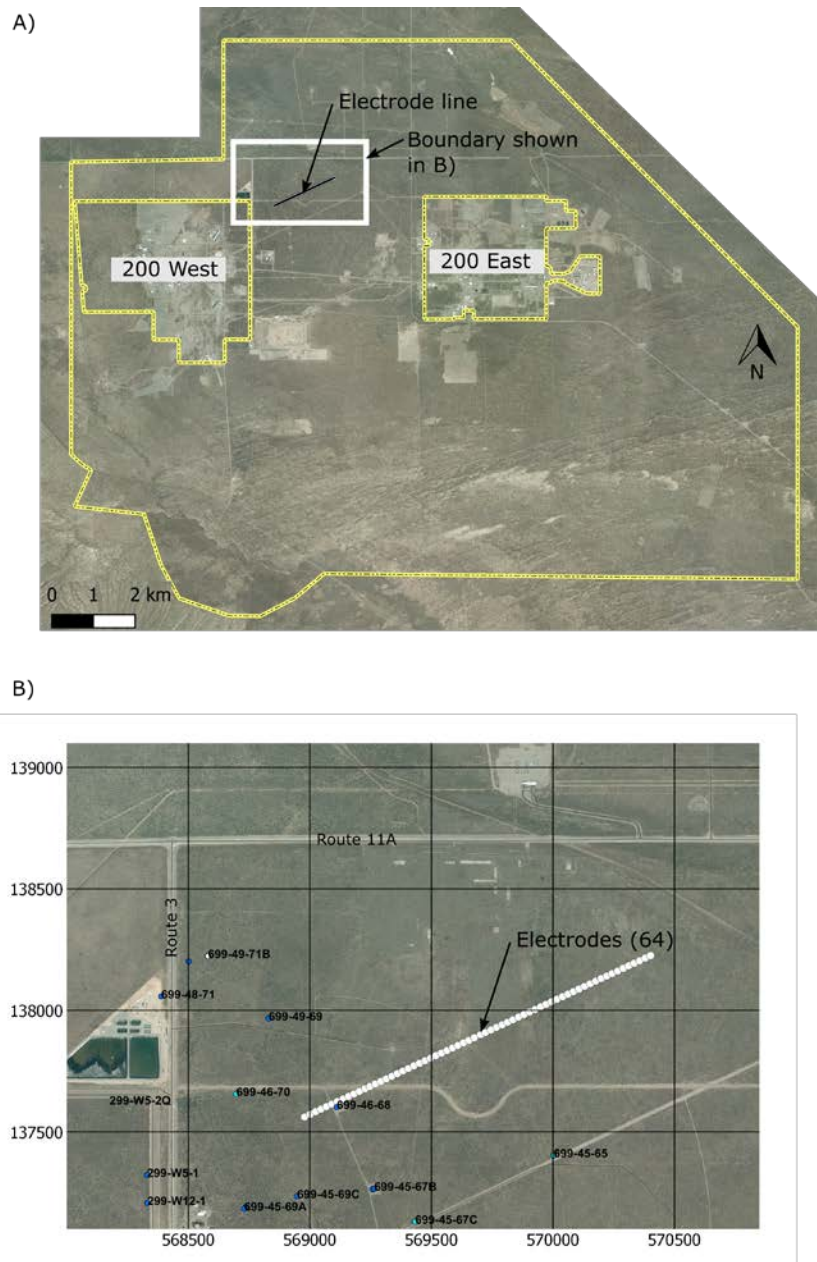


Figure 6.1. Field location of the ~1.6-km ERT line between the 200 East and West areas: A) the location in relation to 200 East and West on the Central Plateau; B) aerial image showing 64 electrodes (~25 m spacing).

6.1 ERT Array Design

6.1.1 Field Setup

The 2D ERT surface electrode array was designed to image the subsurface down to roughly 120 m elevation. A total of 64 electrodes, spaced approximately 25 m apart, were installed for a total line length of approximately 1575 m (Figure 6.1b). The electrodes are 10-inch-long galvanized carbon steel spikes with a 3/8-inch-diameter shaft and a 5/8-inch-diameter head. Four electrodes act collectively as one current injection location. The electrodes were installed manually using hand tools (hammer) through four

1/2-inch-diameter holes in an electrical isolation box (Figure 6.2a and b). The electrodes acted as stakes to hold down these boxes. Polycase[®] (model WQ-64) boxes made of fiberglass-reinforced polycarbonate with a polycarbonate lid were used to isolate the electrodes from exposure during operation.

A Multi-Phase Technologies (model MPT-DAS1) ERT system was used. Four connection cables (16 electrodes each) were composed of 24-AWG stranded tin copper (jacketed with polyurethane insulation rated up to 1100 VDC) to safely transmit up to 3.6 amp with a resistance of 36 ohm per 1000 ft. Connection cables were encased within 5/8-in. and 1/2-in. split-loom as protection from environmental and biological hazards.

The MPT-DAS1 system and the internal high-voltage transmitter were powered using four 12V batteries – two batteries for the transmitter and two batteries for the MPT-DAS1 control module and a power inverter for the controlling PC (Figure 6.2C).



Figure 6.2. Field site data collection images: A) representative field site image showing installation of electrodes; B) polycase[®] box containing connector cable and ERT hookups with four electrodes penetrating to the surface; C) MPT-DAS1 system for field data collection.

6.1.2 Data Collection

Data collection was conducted using an approved operating procedure. A single ERT measurement involves injecting current (I) between one electrode pair and measuring the resultant electrical potential (i.e., the voltage, ΔV) across a second (or more) electrode pair(s). Raw ERT data are provided to the inversion algorithm as the observed voltages normalized by the injected currents ($\Delta V / I$) and have units of resistance (ohms). Different electrode configurations are used to optimize imaging resolution.

ERT measurements included a comprehensive series of Wenner-Alpha, Schlumberger, multiple-gradient, and dipole-dipole four-electrode configurations (Figure 6.3). Small-offset dipoles (electrodes pairs in close proximity to each other), where a and na are small in Figure 6.3, provide high resolution near the electrodes and constrain near-surface structures in the ERT inversion. Large offset dipoles (large n and na) probe deeper into the subsurface. The comprehensive combination of small, intermediate, and large offset dipoles used in the survey was implemented to provide optimal resolution for both shallow and deep structures to the extent possible. The survey was also optimized to leverage the eight channels

available in the MPT-DAS 1 system; eight different potential electrode pairs were recorded for each current electrode pair. In total, 6,500 measurements were collected.

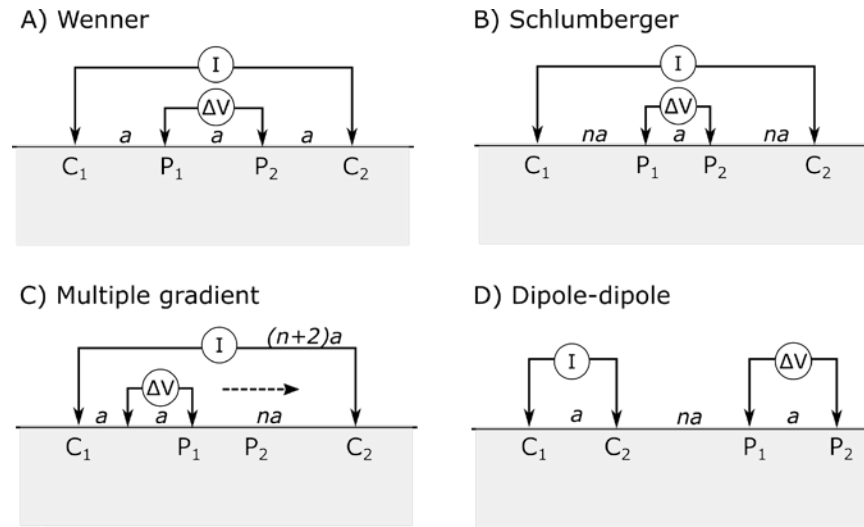


Figure 6.3. Electrode measurement configurations used in the ERT survey, including A) Wenner-Alpha, B) Schlumberger, C) Multiple gradient, and D) dipole-dipole. C1 and C2 are current source and sink, respectively. P1 and P2 are the potential source and sink, respectively.

Data quality was assessed by reviewing contact resistances, current injections, and stacking deviations for each measurement. Using conservative boundaries for these values, outlier measurements were removed. The total number of outliers was 8% of the data collected, confirming that the dataset is of very high quality.

Data quality was also assessed through collection of full set of reciprocal measurements. If the normal (N) measurement is defined as the current and potential electrode pairs as defined in the measurement sequence, the reciprocal (R) measurement is where the current and potential electrode pairs are swapped. In theory, these measurements should be equal and differences can be attributed to data noise (Parasnis 1988). Reciprocal error R_e in units of ohm is defined as:

$$R_e = |R_N - R_R|,$$

where R_N is the measured normal resistance and R_R is the measured reciprocal resistance. The signal-to-noise ratio (SNR) reciprocal error is defined here as:

$$\frac{|R_{avg}|}{R_e}, \text{ where}$$

$$R_{avg} = (R_N + R_R)/2$$

Table 6.1 summarizes the reciprocity analysis for each electrode configuration type, where Wenner and Schlumberger measurements are summarized as a single electrode configuration. Note that when the potential electrodes are located between the current electrodes, the SNR increases and the number of filtered measurements decreases. Overall, these SNR values show the data is of very high quality.

Table 6.1. Reciprocity analysis.

Electrode Configuration	Total #		Inverted #
	Measurements	SNR	Measurements
Wenner-Schlumberger	1828	1333	1764
Multiple gradient	2072	714	1629
Dipole-dipole	2600	364	1610
<i>Total</i>	<i>6500</i>		<i>5003</i>

6.2 ERT Modeling Considerations

Surface topography affects current flow pathways in the subsurface and should be considered in the ERT modeling. Aside from topography, several large depressions were observed adjacent to the ERT line. To incorporate surface elevation variability in the ERT modeling, electrode elevations were globally positioned with a field survey. Also, Hanford LIDAR data (<https://phoenix.pnnl.gov>) at 15 m resolution was incorporated in the surface representation of the site.

Buried metallic infrastructure such as well casings, pipelines, and railroad tracks redistributes subsurface current flow during ERT measurements and can significantly affect ERT images. If metallic subsurface features are not modeled correctly, the processing algorithm compensates by placing anomalously high conductivity features near the infrastructure to match the ERT measurements. These deleterious artifacts mask subsurface bulk conductivity and reduce the utility of ERT. Johnson and Wellman (2015) demonstrated a method of removing the effects of buried infrastructure by explicitly modeling the infrastructure in the forward modeling phase of the ERT imaging algorithm. This method was used here to model the metallic well casing for well 699-46-68 (see Figure 6.1B).

6.3 ERT Survey Results

The ERT data were processed in parallel using 66 processing cores on the Constance supercomputer located at Pacific Northwest National Laboratory. The imaging mesh with infrastructure consisted of approximately 450,000 tetrahedral elements. The raw ERT data were matched with high fidelity (Figure 6.4) to the bulk conductivity model, which requires high-quality data, accurate electrode locations, and accurate forward modeling simulations in the imaging algorithm.

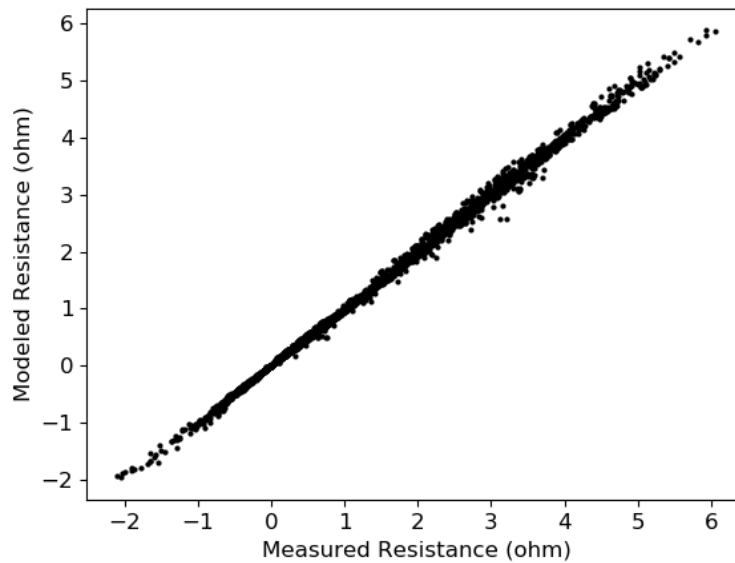


Figure 6.4. Modeled resistance versus measured resistance for each of the 5,003 ERT measurements.

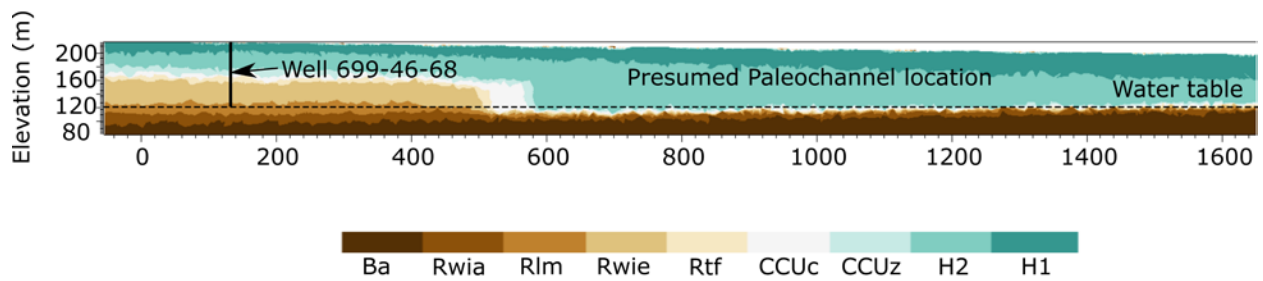
Figure 6.5 shows the Central Plateau GFM (CHPRC 2019, 2018a,b) compared to the ERT model inversion results to potentially correlate these two disparate informational images. Well 699-46-68, which is offset from the ERT line, is also shown for reference. The x-axis denotes the length along the ERT line, starting from the southwestern-most electrode (568978E, 137561N) and ending at the northeastern-most electrode (570402E, 138226N). The paleochannel location in Figure 6.5A is presumed to be within the Hanford units (denoted H1 and H2). A vertical boundary is shown within the H2 unit between 550 and 600 m, which represents where a paleochannel feature is predicted.

Within the ERT image (Figure 6.5B), coarser units are presumed to be zones of low electrical conductivity above the water table, representing low-saturation units within the stratigraphic sequence. The shaded regions at depth represent poorly resolved zones through a sensitivity analysis following the approach of Kemna (2000). The image delineates two low electrically conductive features, with a higher electrically conductive feature in between. A near-surface high conductivity feature corresponds with the road crossing, potentially caused by backfill or road runoff events.

The geologic interpretation between 550 and 600 m in Figure 6.5A, an area with sparse borehole coverage, does not correlate with the image in Figure 6.5B. In addition, the ERT image predicts a low electrical conductivity feature in the region between 200 East and West, and this feature does not correspond in all locations with the Hanford units from the GFM.

Below the water table, coarser units are expected to have a higher electrical conductivity than surrounding units; however, this is not revealed in the Figure 6.5B. The ERT data alone cannot resolve the sharp conductivity contrast expected at the water table. Imposing a sharp conductivity contrast at the water table boundary was implemented but it didn't change the locations of the low conductivity features and added additional structure to the model, so it was chosen to only display the smoothness inversion in Figure 6.5B. The low electrically conductive regions in the vadose zone can be interpreted as zones where coarser sediments incise into lower units.

A) Geologic framework model



B) ERT model

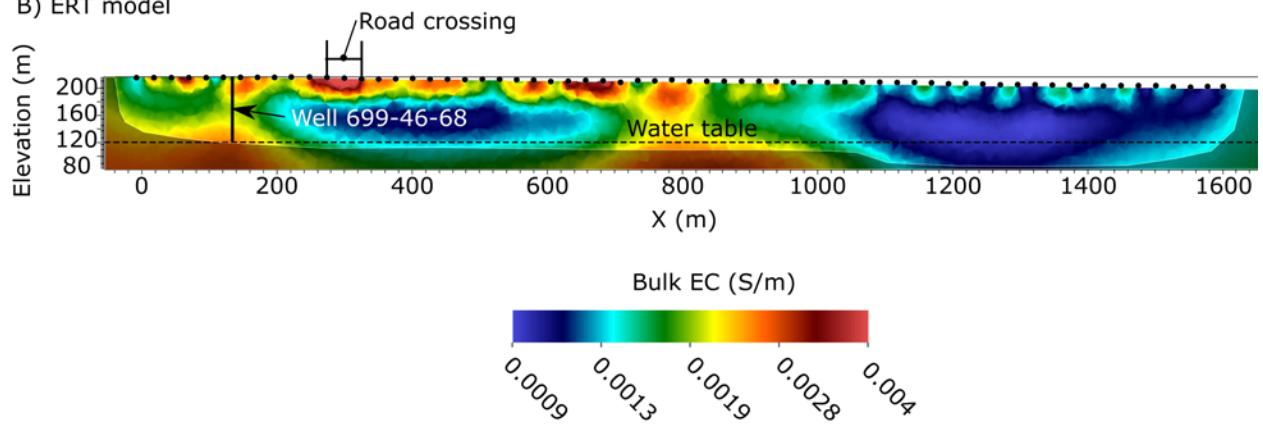


Figure 6.5. A comparison of A) the geologic framework model (CHPRC 2019, 2018a,b) compared to B) the ERT inversion results. The shaded gray region in B) represents poorly resolved ERT zones. Refer to Table 5.2 for stratigraphic unit abbreviations shown in the legend for A).

7.0 Summary and Recommendations

The evaluation in this report was performed by (1) reviewing historical field investigations where the objective of the field campaign was specifically related to identifying transmissive features; (2) conducting hydrogeophysical simulations to assess the feasibility of using ERT to characterize transmissive, paleochannel features; and (3) conducting a 2D field ERT survey between the 200 West and East Areas.

7.1 Geophysical Surveys at Hanford

Previous geophysical field surveys at Hanford employed EM, seismic, and ERT methods to delineate subsurface structure and stratigraphy. EM surveys in the 600 Area were conducted to identify transmissive features in the top 100 m of the subsurface. Seismic surveys near Gable Gap and LERF were executed to map the depth to the basement basalt and identify lithologic contacts within suprabasalt sediments. ERT has been used to map lithologic boundaries and structure in support of other investigations, and time-lapse ERT has been used to better understand surface water-groundwater interactions at the 300 Area. Each of these geophysical methods samples a volume of earth and measures a bulk quantity. Therefore, the success of a method for stratigraphic identification depends on a contrast in biological, chemical, and physical properties that impact the measured quantity and the resolution of the geophysical survey.

Depths for EM and seismic geophysical models were estimated during previous investigations by calibrating to known information, such as EM receiver height and seismic borehole check shots to known units, respectively. However, this localized information for stratigraphic interpretation may not be sufficient for a spatially extensive 3D model. True depth estimates for a 3D model can only be obtained through numerical inverse modeling, which can also use all available information for ground truthing. Existing datasets that have not been previously inverted can be re-evaluated without the expense of conducting an additional field survey.

ERT has a distinct advantage over other geophysical methods in imaging transient processes because sensors (i.e., electrodes) can be left in place. This allows for continuous, autonomous data collection and analysis over time.

7.2 Paleochannel Evaluation

The hydrogeophysical simulations represent an evaluation of a large-scale ERT field survey with a tracer injection for paleochannel identification. The simulations allowed for realistic expectations for static and time-lapse ERT imaging; the 2D ERT field survey provided an assessment of data quality/site noise, signal strength, and bulk electrical conductivity structure. The bulk EC structure from the field survey was aligned with the findings for static ERT imaging in terms of bulk EC contrast and site noise levels.

Static 2D ERT imaging in the field delineated vertical contacts within the vadose zone. The depth of investigation was estimated to be below the water table. The assumption is that contrasting low electrically conductive features are representative of high hydraulic conductivity units incised into the deeper units and represent areas where there are highly transmissive units below the water table.

Given the findings of hydrogeophysical simulations and the 2D ERT field imaging the following is recommended:

1. Additional 2D ERT static imaging between 200 East and West to map areas where transmissive features extend below the water table. The electrode spacing used in the 2D field imaging provided both shallow and deeper information; extension of the ERT line could potentially probe deeper into the subsurface.
2. Combine 2D static ERT surveys for a pseudo-3D evaluation and interpretation between 200 West and East. While 2D imaging will not provide 3D coverage of an area, individual evaluation of each 2D dataset could potentially be used to determine subsequent locations. This overall could be an advantage for the kilometer-scale area between the 200 East and West Areas.
3. Data collection and analyses could be followed by (a) selection of borehole locations within the paleochannel to monitor groundwater concentrations and/or b) refinement of the location of an ERT field campaign/feasibility using a tracer injection to monitor transport over time. Further hydrogeophysical feasibility testing would benefit from site-specific hydrostratigraphic unit petrophysical parameters. The permitting logistics for a tracer injection and concentration of 757 m³ and 60 g/L, respectively, are reviewed in Appendix A.

8.0 Quality Assurance

This work was performed in accordance with the Pacific Northwest National Laboratory (PNNL) Nuclear Quality Assurance Program (NQAP). The NQAP complies with DOE Order 414.1D, *Quality Assurance*, and 10 CFR 830 Subpart A, *Quality Assurance Requirements*. The NQAP uses NQA-1-2012, *Quality Assurance Requirements for Nuclear Facility Application*, as its consensus standard and NQA-1-2012, Subpart 4.2.1, as the basis for its graded approach to quality.

This work emphasized acquiring new theoretical or experimental knowledge and the initial stages of proving scientific theory. The information associated with this report should not be used as design input or operating parameters without additional qualification.

9.0 References

- Annan AP. 2009. *Electromagnetic Principles of Ground Penetrating Radar*. Vol. 1(1), 1–37.
- Archie GE. 1942. “The Electrical Resistivity Log as an Aid in Determining Some Reservoir Characteristics.” *Petroleum Transactions of AIME* 146:54–62.
- ASME NQA-1-2000, *Quality Assurance Requirements for Nuclear Facility Applications*. American Society of Mechanical Engineers, New York, NY.
- ASTM International. 1999. ASTM D6429-99, *Standard Guide for Selecting Surface Geophysical Methods*. West Conshohocken, PA. www.astm.org.
- Banks WSL and CD Johnson. 2011. *Collection, Processing, and Interpretation of Ground-Penetrating Radar Data to Determine Sediment Thickness at Selected Locations in Deep Creek Lake, Garrett County, Maryland, 2007*. Scientific Investigations Report 2011–5223, U.S. Department of the Interior, U.S. Geological Survey, Reston, VA.
- Barclay F, KB Rasmussen, A Cooke, D Cooke, D Salter, D Lowden, S Pickering, A Rasmussen, and R Roberts. 2008. “Seismic Inversion: Reading Between the Lines.” *Oilfield Review*, 42–63.
- Beamish D. 2004. “Airborne EM Skin Depths.” *Geophysical Prospecting* 52:439–49.
- Behroozmand A, K Keating, and E Auken. 2014. “A Review of the Principles and Applications of the NMR Technique for Near-Surface Characterization.” *Surveys in Geophysics* 36(1):27–85. <https://doi.org/10.1007/s10712-014-9304-0>
- Bergstrom KA, TH Mitchell, and JR Kunk. 1993. *Interpretation of Ground Penetrating Radar Data at the Hanford Site, Richland, Washington*. WHC-SA-2018-FP, Westinghouse Hanford Co., Richland, WA.
- Bevan BW and TN Smekalova. 2013. “Magnetic Exploration of Archaeological Sites.” *Good Practice in Archaeological Diagnostics*, 133–52. Springer, Cham. https://doi.org/10.1007/978-3-319-01784-6_7
- Blakely RJ. 1996. *Potential Theory in Gravity and Magnetic Applications*. Cambridge University Press.
- Binley A. 2015. “Tools and Techniques: Electrical Methods.” *Treatise on Geophysics*, 233–259. <https://doi.org/10.1016/B978-0-444-53802-4.00192-5>
- Bjornstad BN and DC Lanigan. 2007. *Geologic Descriptions for the Solid-Waste Low Level Burial Grounds*. PNNL-16887, Pacific Northwest National Laboratory, Richland, WA.
- Bjornstad BN, PD Thorne, BA Williams, GV Last, GS Thomas, MD Thompson, JL Ludwig, and DC Lanigan. 2010. *Hydrogeologic Model for the Gable Gap Area, Hanford Site*. PNNL-19702, Pacific Northwest National Laboratory, Richland, WA.
- Brunet P, R Clément, and C Bouvier. 2010. “Monitoring Soil Water Content and Deficit Using Electrical Resistivity Tomography (ERT) – A Case Study in the Cevennes Area, France.” *Journal of Hydrology* 380(1–2):146–53. <https://doi.org/10.1016/j.jhydrol.2009.10.032>

Budge TJ. 2017. *Model Package Report: Central Plateau Groundwater Model, Version 8.4.5*. CP-47631, Rev. 4, U.S. Department of Energy, Office of Environmental Management, Washington, D.C.

Budge TJ. 2019. *Model Package Report: Central Plateau Groundwater Model, Version 8.2*. CP-57037, Rev. 1, U.S. Department of Energy, Office of Environmental Management, Washington, D.C.

Carling PA, CS Bristow, and AS Litvinov. 2016. “Ground-Penetrating Radar Stratigraphy and Dynamics of Megaflood Gravel Dunes.” *Journal of the Geological Society* 173(3):550–59.
<https://doi.org/10.1144/jgs2015-119>

CHPRC. 2019. *Central Plateau Vadose Zone Geoframework*. ECF-HANFORD-18-0035, Rev. 1, CH2M Hill Plateau Remediation Company, Richland, WA.

CHPRC. 2018a. *Development of the Hanford South Geologic Framework Model, Hanford Site, Washington*. ECF-HANFORD-13-0029, Rev. 5, CH2M Hill Plateau Remediation Company, Richland, WA.

CHPRC. 2018b. *Model Package Report: Central Plateau Vadose Zone Geoframework*. CP-60925, Rev. 0, CH2M Hill Plateau Remediation Company, Richland, WA.

CHPRC. 2016. *Development of the Hanford South Geologic Framework Model, Hanford Site, Washington Fiscal Year 2016 Update*. ECF-HANFORD-13-0029, Rev. 4, CH2M Hill Plateau Remediation Company, Richland, WA.

CHPRC. 2012. *Integrated Surface Geophysical Investigation Results at Liquid Effluent Retention Facility, 200 East Area, Hanford, Washington*. SGW-52467, CH2M Hill Plateau Remediation Company, Richland, WA.

CHPRC. 2011. *Interpretation and Integration of Seismic Data in the Gable Gap*. SGW-48478, CH2M Hill Plateau Remediation Company, Richland, WA.

CHPRC. 2010a. *Testing Ground Based Geophysical Techniques to Refine Electromagnetic Surveys North of the 300 Area, Hanford, Washington*. SGW-47996, Rev 0, CH2M Hill Plateau Remediation Company, Richland, WA.

CHPRC. 2010b. *Interpretation of Airborne Electromagnetic and Magnetic Data in the 600 Area*. SGW-47839, CH2M Hill Plateau Remediation Company, Richland, WA.

CHPRC. 2009. *Landstreamer / Gimbaled GeoPhone Acquisition of High Resolution Seismic Reflection Data North of the 200 Areas - Hanford Site Landstreamer / Gimbaled GeoPhone Acquisition of High Resolution Seismic Reflection Data North of the 200 Areas - Hanford Site*. SGW-43746, CH2M Hill Plateau Remediation Company, Richland, WA.

Dahlin T and V Leroux. 2012. “Improvement in Time-Domain Induced Polarization Data Quality with Multi-Electrode Systems by Separating Current and Potential Cables.” *Near Surface Geophysics* 10(6):545–65. <https://doi.org/10.3997/1873-0604.2012028>

Day-Lewis FD, K Singha, and AM Binley. 2005. “Applying Petrophysical Models to Radar Travel Time and Electrical Resistivity Tomograms: Resolution-Dependent Limitations.” *Journal of Geophysical Research B: Solid Earth* 110(8):1–17. <https://doi.org/10.1029/2004JB003569>

- DOE Order 414.1D, *Quality Assurance*. U.S. Department of Energy, Washington, D.C.
- DOE. 2002. *Standardized Stratigraphic Nomenclature for Post-Sediments Within the Central Pasco Basin*. Vol. 39, U.S. Department of Energy, Washington, D.C.
- DOE. 2017. *Hanford Site Groundwater Monitoring Report for 2017*. DOE/RL-2017-66, U.S. Department of Energy, Richland Operations Office, Richland, WA.
- DOE. 2012. *Hanford Site Groundwater Monitoring for 2011*. DOE/RL-2011-118, U.S. Department of Energy, Richland Operations Office, Richland, WA.
- Dyck AV and GF West. 1984. "The Role of Simple Computer Models in Interpretations Wide-Band , Drill-Hole Electromagnetic Surveys in Mineral Exploration." *Geophysics* 49(7):957–80.
- Falzone S, J Robinson, and L Slater. 2018. "Characterization and Monitoring of Porous Media with Electrical Imaging : A Review." *Transport in Porous Media* 26. <https://doi.org/10.1007/s11242-018-1203-2>
- Fang YD, D Appriou, DH Bacon, V Freedman, ML Rockhold, C Ruprecht, GD Tartakovsky, MD White, SK White, and F Zhang. 2015. *ESTOMP Online User Guide*. Pacific Northwest National Laboratory, Richland, WA. http://stomp.pnnl.gov/estomp_guide/eSTOMP_guide.stm
- Fayer MJ and TB Walters. 1995. *Estimated Recharge Rates at the Hanford Site*. PNL-10285, Pacific Northwest Laboratory, Richland, WA.
- Fecht KR, SP Reidel, and AM Tallman. 1985. *Paleodrainage of the Columbia River System on the Columbia Plateau of Washington State - A Summary*. RHO-BW-SA-318-P, Rockwell International Corp., Richland, WA.
- Fink JB, MT Levitt, DF Rucker, and MB Skorska. 2010. "Detection of Historical Pipeline Leak Plumes Using Non-Intrusive, Geophysical Techniques at the Hanford Nuclear Site, Washington, USA." *WM2011 Conference*, March 7-11, 2011. Phoenix, AZ.
- Fluor Hanford Inc. 2008a. *Logistics and Processing Report Airborne Magnetic and HeliGEOTEM® II Survey*. Airborne Magnetic and HeliGEOTEM II Survey. Job No. 08027, Richland, WA.
- Fluor Hanford Inc. 2008b. *Resolve Survey*. Report #08027R, Richland, WA.
- Fraser DC. 1978. "Resistivity Mapping with an Airborne Multicoil Electromagnetic System." *Geophysics* 43(I):144–72.
- Fugro Airborne Surveys. 2010. *EM Interpretation Report Airborne RESOLVE® and HeliGEOTEM® II Survey*. Job No. 10554, Ottawa, Ontario.
- Gander MJ, KD Leary, MT Levitt, CW Miller, and DF Rucker. 2011. "Geophysics and Site Characterization at the Hanford Site : The Successful Use of Electrical Resistivity to Position Boreholes to Define Deep Vadose Zone Contamination-11509." *WM2011 Conference*, March 7-11, 2011, 15.
- Geomatrix Consultants Inc. 2005. *Evaluation of Geophysical Technologies for Subsurface Characterization*. Project No. 10960, Denver, CO.

- Haldar SK. 2018. “Exploration Geophysics, Magnetic Survey.” In *Mineral Exploration: Principles and Applications*, 111–13. Elsevier. <https://doi.org/10.1016/B978-0-12-814022-2.00006-X>
- Hammond TB and D Lupton. 2015. *Development of the Hanford South Geologic Framework Model, Hanford Site, Washington*. ECF-HANFORD-13-0029, Rev. 2, CH2M Hill Plateau Remediation Company, Richland, WA.
- Harari Z. 1996. “Ground-Penetrating Radar (GPR) for Imaging Stratigraphic Features and Groundwater in Sand Dunes.” *Journal of Applied Geophysics* 36(1):43–52. [https://doi.org/10.1016/S0926-9851\(96\)00031-6](https://doi.org/10.1016/S0926-9851(96)00031-6)
- Huang H and DC Fraser. 1996. “The Differential Parameter Method for Multifrequency Airborne Resistivity Mapping.” *Geophysics* 61(1):100–109.
- Huisman JA and SS Hubbard. 2003. “Measuring Soil Water Content with Ground Penetrating Radar A Review.” *Vadose Zone* 2(4):476–91. <https://doi.org/10.2113/2.4.476>
- Hyde ER, MA Speece, CA Link, TR Repasky, MD Thompson, and SF Miller. 2011. “A Seismic Landstreamer Survey at the Hanford Site, Washington, U.S.A.” *Environmental and Engineering Geoscience* 17(3):227–39. <https://doi.org/10.2113/gseegeosci.17.3.227>
- Isono T. 1984. “Density, Viscosity, and Electrolytic Conductivity of Concentrated Aqueous Electrolyte Solutions at Several Temperatures. Alkaline-Earth Chlorides, LaCl_3 , Na_2SC_4 , NaN_3 , NaBr , KNC_3 , KBr , and $\text{Cd}(\text{NO}_3)_2$.” *Journal of Chemical and Engineering Data* 29(1):45–52. <https://doi.org/10.1021/jc00035a016>
- Johnson TC, LD Slater, D Ntarlagiannis, FD Day-Lewis, and M Elwaseif. 2012. “Monitoring Groundwater-Surface Water Interaction Using Time-Series and Time-Frequency Analysis of Transient Three-Dimensional Electrical Resistivity Changes.” *Water Resources Research* 48(7).
- Johnson TC and D Wellman. 2015. “Accurate Modelling and Inversion of Electrical Resistivity Data in the Presence of Metallic Infrastructure with Known Location and Dimension.” *Geophysical Journal International* 202(2):1096–1108. <https://doi.org/10.1093/gji/ggv206>
- Johnson TC. 2014. *E4D: A Distributed Memory Parallel Electrical Geophysical Modeling and Inversion Code User Guide - Version 1.0*. PNNL-SA-23783, Pacific Northwest National Laboratory, Richland, WA.
- Johnson TC, GE Hammond, and X Chen. 2017. “PFLOTRAN-E4D: A Parallel Open Source PFLOTRAN Module for Simulating Time-Lapse Electrical Resistivity Data.” *Computers and Geosciences* 99(September 2016):72–80. <https://doi.org/10.1016/j.cageo.2016.09.006>
- Johnson TC and DM Wellman. 2013. *Re-Inversion of Surface Electrical Resistivity Tomography Data from the Hanford Site B-Complex*. PNNL-22520, Pacific Northwest National Laboratory, Richland, WA.
- Johnson TC, RJ Versteeg, A Ward, FD Day-Lewis, and A Revil. 2010. “Improved Hydrogeophysical Characterization and Monitoring through Parallel Modeling and Inversion of Time-Domain Resistivity and Induced-Polarization Data.” *Geophysics* 75(4).
- Johnson TC, R Versteeg, J Thomle, G Hammond, X Chen, and J Zachara. 2015. “Four-Dimensional Electrical Conductivity Monitoring of Stage-Driven River Water Intrusion: Accounting for Water Table

Effects Using a Transient Mesh Boundary and Conditional Inversion Constraints.” *Water Resources Research* 51:1–20. [https://doi.org/10.1016/0022-1694\(68\)90080-2](https://doi.org/10.1016/0022-1694(68)90080-2)

Jol HM and DG Smith. 1991. “Ground Penetrating Radar of Northern Lacustrine Deltas.” *Canadian Journal of Earth Sciences* 28(12):1939–47. <https://doi.org/10.1139/e91-175>

Kemna A. 2000. “Tomographic Inversion of Complex Resistivity – Theory and applications”. PhD Thesis, Bochum Ruhr-Univ., Germany (published by: Der Andere Verlag, Osnabruck, Germany).

Kemna A, J Huisman, E Zimmerman, R Martin, Y Zhao, A Treichel, A Orozco, and T Fechner. 2014. “Broadband Electrical Impedance Tomography for Subsurface Characterization Using Improved Corrections of Electromagnetic Coupling and Spectral Regularization.” In *Tomography of the Earth’s Crust: From Geophysical Sounding to Real-Time Monitoring*. Springer, Cham. https://doi.org/10.1007/978-3-319-04205-3_1

Knight R, J Irving, E Freeman, and P Tercier. 2003. “The Use of GPR as a Means of Locating Clastic Dikes.” In *Symposium on the Application of Geophysics to Engineering and Environmental Problems*, 221–27. Society of Exploration Geophysicists.

Knight RJ, JD Irving, P Tercier, and GJ Freeman. 2007. “A Comparison of the Use of Radar Images and Neutron Probe Data to Determine the Horizontal Correlation Length of Water Content.” *Subsurface Hydrology: Data Integration for Properties and Processes* 171(January):31–44. <https://doi.org/10.1029/171GM05>

Lanigan DC, GV Last, BN Bjornstad, PD Thorne, and WD Webber. 2010. *Hanford Site Guidelines for Preparation and Presentation of Geologic Information*. PNNL-18819, Pacific Northwest National Laboratory, Richland, WA.

Last GV, EJ Freeman, KJ Cantrell, MJ Fayer, GW Gee, WE Nichols, BN Bjornstad, and DG Horton. 2006. *Vadose Zone Hydrogeology Data Package for Hanford Assessments*. PNNL-14702, Rev. 1, Pacific Northwest National Laboratory, Richland, WA.

Last GV and DG Horton. 2000. *Review of Geophysical Characterization Methods Used at the Hanford Site*. PNNL-13149, Pacific Northwest National Laboratory, Richland, WA.

Legault JM. 2015. “Airborne Electromagnetic Systems--State of the Art and Future Directions.” *CSEG Recorder* 40(6):38–49.

Lesmes DP and SP Friedman. 2005. “Relationships between the Electrical and Hydrogeological Properties of Rocks and Soils.” In *Hydrogeophysics*, 87–128. Springer Netherlands. https://doi.org/10.1007/1-4020-3102-5_4

Lin C, C Lin, and C Chien. 2017. “Dispersion Analysis of Surface Wave Testing – SASW vs. MASW.” *Journal of Applied Geophysics* 143:223–30. <https://doi.org/10.1016/j.jappgeo.2017.05.008>

Lin Y. 2007. “Characterizing vs Profiles by the SASW Method and Comparison with Other Seismic Methods.” Doctoral Dissertation. The University of Texas at Austin.

MacQueen JD and E Mann. 2007. *Borehole Gravity Meter Surveys at the Waste Treatment Plant, Hanford, Washington*. PNNL-16490, Pacific Northwest National Laboratory, Richland, WA.

- Mankinen EA, EE Larson, CS Gromme, M Prevot and RS Coe. 1987. “The Steens Mountain (Oregon) Geomagnetic Polarity Transition (USA). 3. Its Regional Significance.” *Journal of Geophysical Research* 92(B8):8057–76. <https://doi.org/10.1029/JB092iB08p08057>
- Martin CJ. 2010. *Overview of Hanford Hydrogeology. Hanford Site Groundwater Monitoring and Performance Report: 2009*. DOE/RL-2010-11, Rev. 1, U.S. Department of Energy, Richland Operations Office, Richland, WA.
- Myers DA, Rucker D, M Levitt, B Cubbage, and C Henderson. 2009. *Surface Geophysical Exploration of SX Tank Farm at the Hanford Site: Results of Background Characterization with Magnetics and Electromagnetics*. RPP-RPT-42, Hanford Site, Richland, WA.
- Murray CJ and GV Last. 2005. *Review of Geophysical Techniques to Define the Spatial Distribution of Subsurface Properties or Contaminants*. PNNL-15305, Pacific Northwest National Laboratory, Richland, WA.
- Nabighian MN, VJS Grauch, RO Hansen, TR LaFehr, Y Li, JW Peirce, JD Phillips and ME Ruder. 2005. “The Historical Development of the Magnetic Method in Exploration.” *Geophysics* 70(6):33ND-61ND. <https://doi.org/10.1190/1.2133784>
- Neal A. 2004. “Ground-Penetrating Radar and Its Use in Sedimentology: Principles, Problems and Progress.” *Earth-Science Reviews* 66(3–4):261–330. <https://doi.org/10.1016/j.earscirev.2004.01.004>
- Niu Q and C Zhang. 2018. “Physical Explanation of Archie’s Porosity Exponent in Granular Materials: A Process-Based, Pore-Scale Numerical Study.” *Geophysical Research Letters* 45(4):1870–77. <https://doi.org/10.1002/2017GL076751>
- NQAP-2012, *Nuclear Quality Assurance Program (NQAP) Manual*. Pacific Northwest National Laboratory, Richland, WA.
- Oostrom M, MJ Truex, ML Rockhold, and TC Johnson. 2017. “Deep Vadose Zone Contaminant Flux Evaluation at the Hanford BY-Cribs Site Using Forward and Imposed Concentration Modeling Approaches.” *Environmental Processes* 4(4):771–97. <https://doi.org/10.1007/s40710-017-0272-5>
- Parasnis, D. 1988. “Reciprocity theorems in geoelectric and geoelectromagnetic work.” *Geoexploration* 25(3): 177-198.
- Park CB, RD Miller, J Xia, and J Ivanov. 2007. “Multichannel Analysis of Surface Waves (MASW) Active and Passive Methods.” *The Leading Edge*, 26.1, 60–64.
- Pelton JR. 2012. “Near-Surface Seismology: Surface-Based Methods.” In *Near-Surface Geophysics*, 219–64. <https://doi.org/10.1190/1.9781560801719.ch8>
- Pluhar CJ, BN Bjornstad, SP Reidel, RS Coe, and PB Nelson. 2006. “Magnetostratigraphic Evidence from the Cold Creek Bar for Onset of Ice-Age Cataclysmic Floods in Eastern Washington during the Early Pleistocene.” *Quaternary Research* 65(1):123–35. <https://doi.org/10.1016/j.yqres.2005.06.011>
- Rabbel W. 2010. “Seismic Methods.” In *Groundwater Geophysics: A Tool for Hydrogeology*, 23–84. Berlin: Springer. <https://doi.org/10.1007/978-3-540-88405-7>

- Reidel SP and TL Tolan. 2013. “The late Cenozoic evolution of the Columbia River system in the Columbia River flood basalt province.” *Geological Society of America Special Papers* 497:201-230.
- Reynolds JH. 2002. “Magnetostratigraphy Adds a Temporal Dimension to Basin Analysis.” Search and Discovery Article #40050.
<http://www.searchanddiscovery.com/pdfz/documents/geophysical/reynolds/images/reynolds.pdf.html>
- Richard BH, JT Lillie, and RA Deju. 1977. *Gravity Studies of the Hanford Reservation, Richland, Washington*. RHO-BWI-C-4, Atomics International Division, Richland, WA.
- Robinson J, TC Johnson, J Thomle and I Demirkanli. 2020. *Electrical Resistivity Tomography of the 216-U-1&2 and 216-U-16 WA-1 Waste Sites*. PNNL-30000, Pacific Northwest National Laboratory, Richland, WA.
- Robinson J, L Slater, T Johnson, A Shapiro, C Tiedeman, D Ntarlagiannis, C Johnson, et al. 2015. “Imaging Pathways in Fractured Rock Using Three-Dimensional Electrical Resistivity Tomography.” *Groundwater* 54(2):1–16. <https://doi.org/10.1111/gwat.12356>
- Robinson J, T Johnson, and M Rockhold. 2019. “Feasibility Assessment of Long-term Electrical Resistivity Monitoring of a Nitrate Plume.” *Groundwater*, April, gwat.12899.
<https://doi.org/10.1111/gwat.12899>
- Rockhold ML, FA Spane, TW Wietsma, DR Newcomer, RE Clayton, I Demirkanli, DL Saunders, MJ Truex, MM Valenta-Snyder, and CJ Thompson. 2018. *Physical and Hydraulic Properties of Sediments from the 200-DV-1 Operable Unit*. PNNL-27846, RPT-DVZ-CHPRC 0005, Rev. 0, Pacific Northwest National Laboratory, Richland, WA.
- Routh PS and DW Oldenburg. 2001. “Electromagnetic Coupling in Frequency-Domain Induced Polarization Data: A Method for Removal.” *Geophysical Journal International* 145(1):59–76.
<https://doi.org/10.1111/j.1365-246X.2001.00384.x>
- Rucker D, M Levitt, and B Cubbage. 2007. *Surface Geophysical Exploration of B, BX, and BY Tank Farms at the Hanford Site: Results of Background Characterization with Magnetics and Electromagnetics*. Vol. RPP-RPT-34, hydroGEOPHYSICS, Inc., Richland, WA.
- Schuck A and G Lange. 2007. “Seismic Methods.” *Environmental Geology*, Springer, Berlin, Heidelberg, 337–402.
- Singha K, F Day-Lewis, T Johnson, and L Slater. 2014. “Advances in Interpretation of Subsurface Processes with Time-Lapse Electrical Imaging.” *Hydrological Processes*.
<https://doi.org/10.1002/hyp.10280>
- Slater LD, D Ntarlagiannis, FD Day-Lewis, K Mwakanyamale, RJ Versteeg, A Ward, C Strickland, CD Johnson, and JW Lane. 2010. “Use of Electrical Imaging and Distributed Temperature Sensing Methods to Characterize Surface Water–Groundwater Exchange Regulating Uranium Transport at the Hanford 300 Area, Washington.” *Water Resources Research* 46(10):1–13. <https://doi.org/10.1029/2010WR009110>
- Smith DG and HM Jol. 1995. “Ground Penetrating Radar: Antenna Frequencies and Maximum Probable Depths of Penetration in Quaternary Sediments.” *Journal of Applied Geophysics* 33(1–3):93–100.
<https://doi.org/10.1358/dof.2006.031.12.1045051>

Spain E and A Venkatanarayanan. 2014. “Review of Physical Principles of Sensing and Types of Sensing Materials.” *Comprehensive Materials Processing*, Vol. 13. Elsevier. <https://doi.org/10.1016/B978-0-08-096532-1.01302-9>

Spies BR. 1989. “Depth of Investigation in Electromagnetic Sounding Methods” *Geophysics* 54(7):872–88.

Steeple DW. 2005. “Shallow Seismic Methods.” In *Hydrogeophysics*, 215–251. Dordrecht: Springer Netherlands. https://doi.org/10.1007/1-4020-3102-5_8

Stokoe K, Y Lin, S Hwang, and J Roberts. 2014. *Hanford Site-Wide Probabilistic Seismic Hazard Analysis (PSHA): Seismic Shear Wave Velocity Profiling at Hanford, WA*. PNNL-23361, Pacific Northwest National Laboratory, Richland, WA.

Strickland CE, MJ Truex, RD Mackley, and TC Johnson. 2018. *Deep Vadose Zone Monitoring Strategy for the Hanford Central Plateau*. PNNL-28031, Pacific Northwest National Laboratory, Richland, WA.

Topp C. 1980. “Electromagnetic Determination of Soil Water Content:” *Water Resources Research* 16(3):574–82.

Vanderborght J, A Kemna, H Hardelauf, and H Vereecken. 2005. “Potential of Electrical Resistivity Tomography to Infer Aquifer Transport Characteristics from Tracer Studies: A Synthetic Case Study.” *Water Resources Research* 41(6):1–23. <https://doi.org/10.1029/2004WR003774>

Veeken PCH and M Da Silva. 2004. “Seismic Inversion Methods and Some of Their Constraints.” *First Break* 22(6):47–70.

Vereecken H, J Huisman, H Bogaen, J Vanderborght, J Vrugt, and JW Hopmans. 2008. “On the Value of Soil Moisture Measurements in Vadose Zone Hydrology: A Review.” *Water Resources Research* 44(4). <https://doi.org/10.1029/2008WR006829>

Wallin EL, TC Johnson, WJ Greenwood, and JM Zachara. 2013. “Imaging High Stage River-Water Intrusion into a Contaminated Aquifer along a Major River Corridor Using 2-D Time-Lapse Surface Electrical Resistivity Tomography.” *Water Resources Research* 49(3):1693–1708. <https://doi.org/10.1002/wrcr.20119>

Ward SH. 1988. “The Resistivity and Induced Polarization Methods.” *Symposium on the Application of Geophysics to Engineering and Environmental Problems*, 147–89. <http://www.earthdoc.org/publication/publicationdetails/?publication=47435>

White MD and M Oostrom. 2006. *STOMP Subsurface Transport Over Multiple Phases, Version 4: User’s Guide*. PNNL-15782 (UC-2010), Pacific Northwest National Laboratory, Richland, WA. <https://stomp.pnl.gov>

Williams BA, BN Bjornstad, R Schalla, and MD Webber. 2002. *Revised Hydrogeology for the Suprabasalt Aquifer System, 200-West Area and Vicinity, Hanford Site, Washington*. PNNL-13858, Pacific Northwest National Laboratory, Richland, WA.

Williams BA, BN Bjornstad, R Schalla, and WD Webber. 2000. *Revised Hydrogeology for the Suprabasalt Aquifer System, 200-East Area and Vicinity, Hanford Site, Washington*. PNNL-12261, Pacific Northwest National Laboratory, Richland, WA.

Wynn JC. 1974. “Electromagnetic Coupling in Induced Polarization.” Doctoral Dissertation. The University of Arizona.

Yaede JR, JH McBride, ST Nelson, CB Park, JA Flores, SJ Turnbull, DG Tingey, et al. 2015. “A Geophysical Strategy for Measuring the Thickness of the Critical Zone Developed over Basalt Lavas.” *Geosphere* 11.2, 514–32. <https://doi.org/10.1130/GES01142.1>

Yue WZ. 2019. “Pore-scale Explanation of the Archie’s Cementation Exponent: Microstructure, Electrical Anisotropy and Numerical Experiments.” *Geophysical Research Letters* 46:9. <https://doi.org/10.1029/2019GL082585>

Zhao Y, E Zimmermann, E Zimmermann, and A Kemna. 2015. “Phase Correction of Electromagnetic Coupling Effects in Cross-Borehole EIT Measurements.” *Measurement Science and Technology PAPER* 26. <https://doi.org/10.1088/0957-0233/26/1/015801>

Appendix A – Tracer Injection Considerations

A.1 Permitting Review

The hydrogeophysical simulations show that high tracer volumes (~757 m³) and concentrations (~60 g/L) are required for electrical resistivity tomography (ERT) time-lapse imaging to reveal transmissive groundwater flow pathways. Beyond technical feasibility, other considerations of a tracer injection at this scale need to be considered. For example, the impact of bromide tracers on the 200 West pump-and-treat resins and facility could be significant and are in the process of being evaluated. Any final action would need to consider all impacts. This appendix is focused solely on permitting requirements.

A tracer injection on the Hanford Site requires a Discharge to Ground Approval, whereby the effluent limits and general requirements of permit ST 4511 are met. The primary requirement in this document is to demonstrate that there will be no adverse impact to groundwater from the tracer injection. Concurrence must also be obtained from the U.S. Department of Energy Richland Operations Office as the landowner. The following must be demonstrated:

1. The tracer plume will remain within the Central Plateau for ~100 years.
2. Tracer concentrations after ~100 years will attenuate to an average less than ~250 mg/L.
3. Discharges do not exceed any Groundwater Quality Criteria (WAC 173-200).
4. A review of Hanford Site groundwater data including an assessment of other constituents that already exceed the WAC 173-200 values.

Other general requirements that must be met for discharges include:

5. No discharges within a surface contamination area.
6. No discharges within a 300-ft horizontal radius of an active or inactive crib, ditch, or trench used for waste disposal.
7. Each discharge has a responsible person assigned should questions arise.
8. Any discharge > 14,500 gal/day or > 50,000 gal/year must be reported at the end of the year.
9. The injection well must be registered as an Underground Injection Control (UIC) well.

There are no biological permitting concerns for Central Plateau work consisting of a KBr tracer injection to groundwater. Many of these requirements are administrative controls that can be demonstrated at the time of permitting. Below, requirements for criteria 1-3 are addressed, through a tracer plume and concentration analysis.

Modeled Tracer Plume and Concentrations

Flow and transport modeling using the eSTOMP flow and transport simulator (Section 5.0 of the main report) demonstrated slow tracer transport and high dilution, which would minimize the impact of a tracer injection. To validate the eSTOMP results and provide input for permitting requirements beyond the limits of the ERT electrode grid, another flow and transport simulation approach using MODFLOW (steady-state groundwater flow) (USGS 2000) and MT3DMS (non-reactive tracer transport) (Zheng and

Wang 1999) was used to model tracer transport across the Central Plateau. The P2R model (Budge 2020) was applied for these. The objective was to assess injection of KBr tracer at two well locations (699-49-69 and MW-10A) and evaluate the direction and extent of tracer transport in the subsurface. Tracer injection parameters for the simulations are summarized in Table A.1.

Table A.1. Parameters for KBr simulations

	Injection Well	
	699-49-69	MW-10A
Hydrogeologic units at screen	Mixture of Hanford and Ringold units	Mixture of Hanford and Ringold units
Well Diameter (in.)	8	8
Injectate KBr Concentration (mg/L)	60000	60000
Injection Volume (m ³)	757	757
Injection Mass (kg)	45420	45420
Injection Duration (d)	7	7
Injection Flow Rate (m ³ /d)	108.155	108.155
Key timepoints of interest (y)	100 and 500	100 and 500

The results for the P2R tracer transport are summarized for 100 and 500 years, respectively. The model output layers were reviewed, and the largest spatial extent and concentrations are shown in Figure A.1 and Figure A.2. Tracer injected into well 699-49-69 has dissipated by 100 years, but earlier times show slow spread in a nominally southwest direction. The tracer injected into well MW-10A spreads in a northeasterly direction. Note that after 100 years there are no tracer concentrations above 100 mg/L. These results concur with the eSTOMP flow and transport simulations, in that they also show high dilution and slow tracer transport resulting from an injection from the two specified wells. These results indicate that the criteria necessary to conduct tracer injections on the Central Plateau will be met.

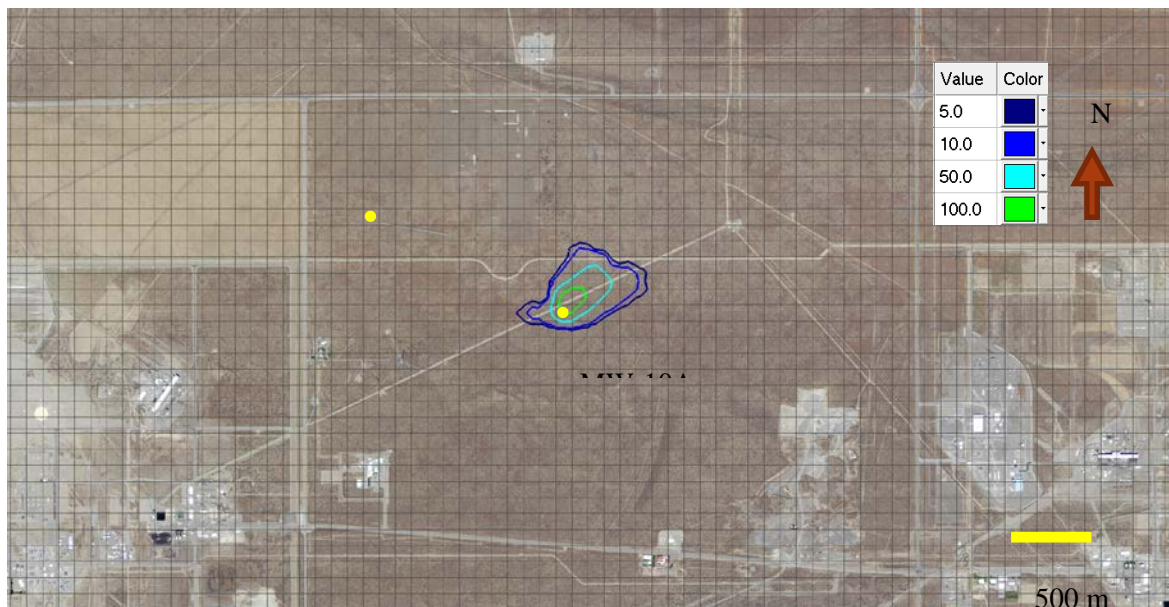


Figure A.1. P2R 100-year tracer transport simulation showing the maximum extent of plume migration in the Central Plateau.

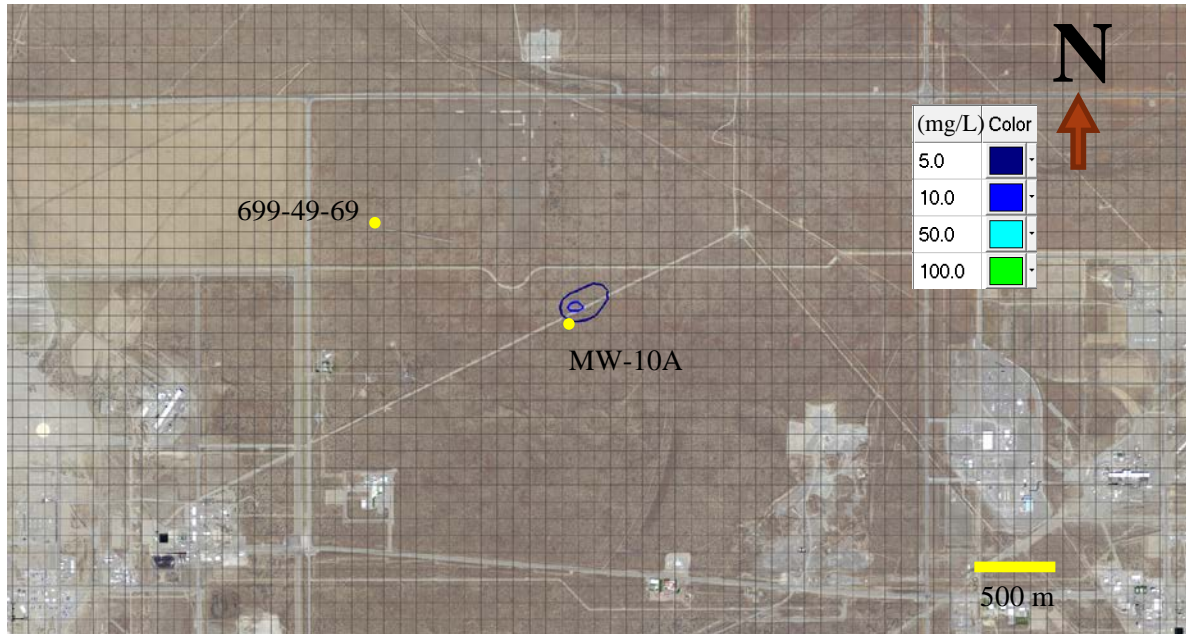


Figure A.2. P2R 500-year tracer transport simulation showing the maximum extent of plume migration in the Central Plateau.

A.2 References

Budge TJ. 2020. *Model Package Report: Plateau to River Groundwater Model, Version 8.3*. CP-57037 Rev. 2, CH2M Hill Plateau Remediation Company, Richland, WA.

USGS. 2000. *MODFLOW-2000, The U.S. Geological Survey Modular Ground-water Model – User Guide to Modularization Concepts and the Ground-Water Flow Process*. Open File Report 00-92, U.S. Geological Survey, Denver, Colorado. <http://water.usgs.gov/nrp/gwsoftware/modflow2000/ofr00-92.pdf>

Zheng C and PP Wang. 1999. *MT3DMS: A Modular Three-Dimensional Multispecies Transport Model for Simulation of Advection, Dispersion, and Chemical Reactions of Contaminants in Groundwater Systems; Documentation and User's Guide*. SERDP-99-1, U.S. Army Engineer Research and Development Center, U.S. Army Corps of Engineers, Vicksburg, Mississippi. Available at: <https://hydro.geo.ua.edu/mt3d/index.htm>

Pacific Northwest National Laboratory

902 Battelle Boulevard
P.O. Box 999
Richland, WA 99354
1-888-375-PNNL (7665)

www.pnnl.gov